Annex I

SEISMIC WAVE INCOHERENCE: A CASE STUDY

I–1. BACKGROUND

Probabilistic seismic hazard assessments (PSHAs) performed recently have yielded uniform hazard response spectra (UHRS) with significant high frequency content, i.e. frequency content greater than 10 Hz. (see Fig. I–1). Similarly, recorded ground motions to varying degrees, and dependent on direction, demonstrate high frequency content (Figs I–2–I–4). These high frequency motions also exist when design spectra are created to envelop a number of different seismic environments for design, e.g., by augmenting broad-banded low frequency design ground response spectra with high frequency motions. The result being design basis ground response spectra with broad low frequency and high frequency content. Figure I.5 shows response spectra for artificial time histories generated to match the USNRC Regulatory Guide 1.60 [I–1] standard response spectra. Figure I–6 shows response spectra for artificial time histories generated to match Ref. [I–1] standard response spectra enhanced in the frequency range of 10–20 Hz.

Taking into account seismic wave incoherence is one tool to address these high frequencies. Seismic motion incoherence is a phenomenon that results in spatial variability of ground motions over large and small distances.

The main sources of incoherence [I–2] are:

- Attenuation effects that are responsible for changes in amplitude and phase of seismic motions as a function of distance from the source to observation points and the distance between observation points. Also, attenuation due to energy dissipation, e.g., damping, that seismic waves experience along the travel paths. This is a significant source of incoherence (lack of correlation) for long structures (bridges); however, for nuclear installations it is not of much significance.
- Wave passage effects contribute to incoherence due to the difference in recorded wave fields at two points as the waves (body and surface) travel from one point to the second point.
- Scattering effects, are responsible for incoherence by creating a scattered wave field. Scattering is due to unknown subsurface geologic features that contribute to modifications of the wave field.
- Extended source effects contribute to incoherence by creating a complex wave source field. As the (extended) fault ruptures, the rupture propagates and generates seismic sources along the rupturing fault. Seismic energy is thus emitted from different points (along the rupturing fault) and has different travel paths and timing as it travels to observation points.

In the context of nuclear installations, wave passage effects and local wave scattering effects are the two most likely sources of ground motion incoherence (GMI).

In general, soil–structure interaction (SSI) is an important phenomenon to take into account as a function of ground motion amplitude and frequency content, site conditions (rock and soil), and structure/foundation conditions. Two aspects of SSI are inertial interaction and kinematic interaction.

- Inertial interaction is the combined dynamic response behaviour of the soil–structure system. For nuclear power plant (NPP) structures and foundations (large, stiff, mat foundations), inertial interaction is especially important for soil sites. The dynamic behaviour of these soil–structure systems is characterized by lower frequencies than for the fixed-base case and increased effective damping of the systems due to radiation damping and the material damping in the soil. These 'equivalent damping' ratios for inertial interaction can range from relatively low values for rocking to very large values (greater than 50%) for horizontal and vertical deformations.
- Kinematic interaction is the effect of spatial variation of ground motion on the "foundation input motion" to the structure.
  There are two aspects of kinematic interaction:

  - The first aspect of kinematic interaction is the spatial variation of ground motion in the soil or rock. The effective excitation of the foundation/structure is dependent on the free field ground motion in the dimensional envelope of the embedded portion of foundation/structure. If the free field control motion is defined at the top of grade, then this spatial variation refers to the variation of motion from the top of grade to the bottom of the foundation. If the free field control motion is defined at a location different than the top of grade, for example, at the top of a hypothetical outcrop at depth, then this spatial variation is determined through wave propagation modelling over the embedded foundation/structure. These phenomena have a significant effect on the foundation input motion generally reducing the translational motion of the foundation and increasing the rotational motion. Generally, the net effect on in-structure responses is a reduction due to embedment. In most cases for soil sites and NPP structures, the reduction in responses is very significant.
  - The second aspect of kinematic interaction is that of incoherency of ground motions, or seismic wave incoherence. For NPP structures, this effect is significant when considering free-field ground motion with significant high frequency content. It is this latter aspect of kinematic interaction that is the focus of this study.

Ground motion incoherence (GMI) occurs due to:

- Random spatial variation (local wave scattering)
  - Scattering of waves due to heterogeneous nature of the soil or rock at the locations of interest and along the propagation paths of the incident wave fields (local wave scattering).
- Wave passage effects
  - Systematic spatial variation due to difference in arrival times of seismic waves across a foundation.

For structures founded on rock or stiff soil, wave passage effects have been shown to have minimal effects on the response of NPP structures mainly based on the range of apparent wave velocities (2 km/s to 4 km/s) derived from the recorded data used to establish the coherency functions [I–2].

Coherency functions that express random spatial variation as a function of frequency and separation distance were developed by Abrahamson [I–3].

The resulting ground motion coherency functions as a function of frequency and distance between observation points were initially generated considering all data regardless of site conditions, earthquake characteristics, and other factors [I–3]. In Ref. [I–4], this initial effort is refined to separate soil and rock sites. Plots of soil and hard rock ground motion coherency functions are shown for horizontal and vertical ground motion components in Figure I–7.

In general, implementing GMI into seismic response analyses has the effect of reducing translational components of excitation at frequencies above about 10 Hz, while simultaneously adding induced rotational input motions (induced rocking from vertical GMI effects and increased torsion from horizontal GMI effects). Significant reductions in in-structure response spectra (ISRS) in progressively higher frequency ranges can be observed.

There is an urgent need to record and process additional data to further verify GMI phenomena and their effects on structures of interest. Until such additional data is accumulated and processed, incorporating the effects of GMI on NPP structures' seismic response for design is as follows:

- Seismic responses (ISRS) for assumptions of coherent and incoherent ground motions need to be calculated to permit comparisons to be made.
- Currently, the following guidelines for ISRS, representing current practice in the USA [I-5] are in place for design:

  (i) For the frequency range 0–10 Hz, no reductions in ISRS are permitted;

  (ii) For the frequencies above 30 Hz, a maximum reduction in ISRS of 30% is permitted;

  (iii) For the frequency range of 10–30 Hz, a maximum reduction based on a linear variation between 0% at 10 Hz and 30% at 30 Hz is permitted.

For BDBE assessments, no such limitations are currently implemented.

I–2. OBJECTIVE

The objective is to investigate the effects of incoherent ground motion on the seismic response of an NPP structure for two site conditions, three recorded earthquake ground motions, two artificial time history ground motions, assuming fixed base conditions, SSI for coherent ground motion and SSI for incoherent ground motion.

I–3. CASE STUDY PARAMETERS

Case study presents the assessment of the effects of GMI on a NPP structure.

The parameters of the study are:

I–3.1. Structure and Foundation

The subject structure is the Kashiwazaki-Kariwa Nuclear Power Plant (KKNPP) Unit 7 Advanced Boiling Water Reactor (ABWR) reactor building, which experienced the Niigataken-chuetsu-oki (NCO) earthquake (16 July 2007) and was studied extensively post-NCOE [I–6]. The structure is shown in Figure I.8.

A detailed finite element dynamic model was developed for the U.S. NRC [I–7] as part of the KARISMA project [I–6] and is used for this case study. The fixed-base model has 480 fixed-base modes with validated horizontal fundamental frequencies: 4.85 Hz (43.7% mass)/6.19Hz (24.2% mass) in the X-direction; and 5.64 Hz (62.1% mass)/7.43Hz (9.25%) in the Y-direction. Vertical frequencies are not clearly distinguishable, i.e., no single mode or two modes dominate the vertical dynamic response.

For simplicity, the foundation is assumed to be surface founded, square in shape (58.0m), and assumed to behave rigidly. The actual foundation/structure configuration is deeply embedded as observed in Figure I–8. The actual plan dimensions of the structure are: 56.6m (NS) x 59.6m (EW). The coordinate system used in the case study is the same as identified in Figure I.8 with the bottom of the base mat located at elevation -13.7m (TMSL), +X (N), +Y (W), +Z(up).

I–3.2. Site Conditions

The site conditions analysed in the case study are: fixed-base and uniform half-spaces with shear wave velocities (Vs) (Vs = 305m/s; Vs = 2,000m/s).

I–3.3. Ground Motions

Five sets of earthquake ground motions (acceleration time histories) are analysed, each comprised of three spatial components (two orthogonal horizontal directions and the vertical direction). Three sets of recorded motions and two sets of artificially generated time histories are used. The sets of recorded motions were selected such that one set is dominated by low frequency motion (El Centro), one dominated by high frequency (Landers), and the third with intermediate frequency content (Val-des-Bois). The sets of artificially generated time histories match the broad-banded response spectra of Ref. [I–1] design response spectra including a spectrum enhanced in the high frequency range.

The recorded ground motion excitations are:

i. Landers earthquake M=7.3; June 28, 1992; recording at San Gabriel, E. Grand Ave. Station (Figure I–2);
ii. Imperial Valley earthquake M=6.9; May 18, 1940; El Centro (Figure I–3);
iii. (iii) Val-des-Bois earthquake, M=5.0, June 23, 2010, Sta OT012 (Figure I–4);

Input motions have three spatial components of recorded motion.

I–3.4. Ground Motion Coherency Functions

Initially, Abrahamson [I–3] developed ground motion coherency functions for the combination of all recorded data regardless of earthquake magnitude, site conditions, etc. Subsequently, Abrahamson partitioned the data into "hard rock" sites and "soil" sites [I–4]. Figure I–7 shows the ground motion coherency functions (horizontal and vertical) for the rock site and soil site. These were used in the current study.

I–3.5. Seismic Response

Seismic responses, in the form of response spectra, are calculated for:

i. The free-field;
ii. Base mat centre, denoted foundation reference point; (free-field and base mat centre are identical for the fixed-base case);
iii. The following in-structure locations (node points), ISRS are calculated:
   NP 1640, 1st Fl, FP1 (-18.50,13.75,12.30); (Figure I–9);
   NP 1694, 1st Fl, CP1 (0.00,-15.50,12.30); (Figure I–9);
   NP 2419, 3rd Fl, FP1 (18.50,13.75,23.50); (Figure.I–10);
   NP 6594, 3rd Fl, FP2 (20.50,17.00,23.50); (Figure I–10);
   NP 2559, 4th Fl, FP1 (-18.50,13.75,31.70); (Figure I–11);
   NP 2621, 4th Fl, FP2 (0.00,-26.50,31.70); (Figure I–11).

Response spectra were calculated for fixed-base, coherent SSI (Vs=305 m/s and Vs=2000 m/s), at six locations/three directions each; incoherent SSI (Vs = 305 m/s and Vs=2000 m/s), at six locations/three directions each. Table I–1 shows the number of analyses performed as a function of the parameters of interest. Response spectra were calculated at 151 frequencies between 0.1 and 100 Hz for 5% damping.

SSI coherent and incoherent analyses were performed with the CLASSI family of programs (Refs [I–8] and [I–9]):

- For coherent analyses, the standard version of CLASSI was used. All three ground motion components were analysed simultaneously.

- For incoherent analyses, the analyses were performed with CLASSIinco-SRSS for each component of the scattering matrix independently, which assumes the relationship between phases of the scattering terms is random. For three components of free-field motion and a 3-D structure, eighteen CLASSIinco-SRSS analyses are performed. In-structure response spectra or other response quantities of interest are generated for each of the eighteen analyses and sum of square root of squares (SRSS) as the end output. In-structure response spectra were the output for this study.

I–4. ANALYSES AND OBSERVATIONS

I–4.1. Node Point (NP) 2559 (-18.5m,13.75m,31.7m)-Rock site

The first set of comparative results is focused on Node point (NP) 2559 with X, Y, Z coordinates of (-18.5m, +13.75m, 31.7m) (denoted F1 in Figure I.11). It is located on the operating floor of the reactor building (Figure I–8). The fixed-base dynamic characteristics show no significant modes in the E-W (Y) direction apparently being located at the top of an E-W shear wall.

The site profile was assumed to be the uniform rock site (uniform half-space Vs=2000m/s). Each of the five sets of earthquake ground motion was analysed for the assumptions of fixed-base, SSI coherent ground motion, and SSI incoherent ground motion.

Case 1: Rock site, Landers earthquake

Figures I–12, I–13, and I–14 show the response spectra of the free-field ground motion with over-plots of the comparison of the response spectra calculated for NP 2559 by analyses of fixed-base, SSI coherent motion, and SSI incoherent motion for the X-, Y-, and Z-directions, respectively.

In Figure I–12, the Landers free-field ground motion response spectrum (X-direction) is dominated by high frequency motion with a peak at 40Hz. The comparative plot shows that the fixed-base response at NP 2559 exhibits peaks at 5 Hz, 6.5 Hz, and 14.5 Hz. The SSI response for the frequency range less than 10Hz exhibits a lower frequency shift and slightly reduced peak values compared to the fixed-base case. In the frequency range of 10–20 Hz, amplification occurs due to the N-S dynamic response of the model for fixed-base, SSI coherent, and SSI incoherent responses. The hierarchy of amplitudes of peak spectral accelerations is fixed-base, coherent SSI, and incoherent SSI as expected; the fixed-base responses are reduced when considering coherent SSI and reduced further when considering incoherent SSI.

In Figure I–13, the Landers free-field ground motion response spectrum (Y-direction) contains high frequency motion with a peak at 30–40Hz. The comparative plot shows that the fixed-base response at NP 2559 exhibits a peak at 5.5 Hz. The SSI response for the frequency range less than 10 Hz exhibits a frequency shift lower compared to the fixed-base and slightly increased peak values compared to the fixed-base case. Since the ground motion coherency functions (Figure I–2) have minimal reductions in amplitude below 10 Hz, reductions in response due to incoherency is not usually observed and expected to be small in this frequency range. In the frequency range greater than 10 Hz, SSI reduces the response to less than the free-field motion, similarly for both coherent and incoherent assumptions.

In Figure I–14, the Landers free-field ground motion response spectrum (Z-direction) is dominated by high frequency motion with a peak in the range 40–50 Hz. The comparative plot shows that dynamic amplification occurs in the 10–20 Hz frequency range due to

dynamic characteristics of the model. The fixed-base, coherent SSI, and incoherent SSI response at NP 2559 exhibit peaks at 10–20 Hz with progressively lower peak values from the fixed-base to the coherent SSI, to the incoherent SSI cases. The SSI responses for the frequency range less than 10 Hz exhibit amplification above the fixed-base case with the coherent and incoherent SSI being approximately the same values.

Recorded high frequency ground motion records show the same behaviour as expected from fixed-base, SSI coherent, and SSI incoherent SSI. Considering SSI for rock for a rock site profile and high frequency ground motion generally follows the trend of SSI reducing motion of in-structure responses (coherent and incoherent). Incoherent SSI further reduces responses for frequency ranges greater than 10 Hz when compared with coherent SSI responses.

Case 2: Rock site, El Centro earthquake

Figures I.15–I.17 show the response spectra of the free-field ground motion with over-plots of the comparison of the response spectra calculated for NP 2559 by analyses of fixed-base, SSI coherent motion, and SSI incoherent motion for the X-, Y-, and Z-directions, respectively.

The two horizontal components of the El Centro ground motion are dominated by low frequency motion (less than 10 Hz). The vertical component has its peak spectral acceleration at 10 Hz.

For this study, the El Centro earthquake is considered to be low frequency ground motion.

In Figures I–15 and I.16, the X-and Y-direction responses for fixed-base, SSI coherent, and SSI incoherent are presented. These NP 2559 responses of interest are in the frequency range less than 10 Hz. No incoherent effects are observed as expected. SSI coherent and incoherent responses are the same or similar for the X- and Y-direction responses.

In the Z-direction, the El Centro ground motion peaks at 10 Hz and is amplified at 10 Hz for the fixed-base, SSI coherent, and SSI incoherent cases. The hierarchy of responses is fixed base to coherent SSI to incoherent SSI.

Low frequency input motion and responses in the horizontal directions are unaffected by incoherence. High frequency input and responses (where high frequency includes the 10 Hz peak for the Z-direction in the free-field) peak at 10 Hz with the hierarchy of highest being the fixed-base, then the coherent SSI, and the lowest is the incoherent SSI.

Case 3: Rock site, Val-des-Bois earthquake

The frequency characteristics of the Val-des-Bois earthquake ground motions are in-between the Landers (high frequency) and the El Centro (low frequency) earthquake motions. For the Val-des-Bois earthquake ground motion, X-direction input has amplified low frequency motion in the range 4–13 Hz; the Y-direction has amplified motion in the

ranges 5–13 Hz and 16–25 Hz; and the Z-direction has amplified motion in the range 6.7–30 Hz.

Figures I–18– I–20 show the response spectra of the free-field ground motion with over-plots of the comparison of the response spectra calculated for NP 2559 by analyses of fixed-base, SSI coherent motion, and SSI incoherent motion for the X-, Y-, and Z-directions, respectively.

For the frequency range less than 15 Hz, responses in the horizontal directions are unaffected by incoherence. In the vertical direction, peaks in the fixed-base response spectra at NP 2559 occur at 7.6Hz, 10.0Hz, and 14.5Hz due to the dynamic characteristics of the structure. Coherent SSI and incoherent SSI reduce these peaks, especially for the peak at 14.5Hz.

Case 4: Rock site, U.S. NRC RG 1.60 artificial time histories

The frequency characteristics of the USNRC RG 1.60 [I–1] artificial time histories (matching the RG 1.60 design basis ground motion response spectra shape) are similar to the El Centro earthquake motions (low frequency). Figures I–21 – I–23 show the response spectra of the free-field ground motion with over-plots of the comparison of the response spectra calculated for NP 2559 by analyses of fixed-base, SSI coherent motion, and SSI incoherent motion for the X-, Y-, and Z-directions, respectively.

This conclusion for Case 2 El Centro applies to the RG 1.60 case:

- Low frequency input motion and responses in the horizontal directions are unaffected by incoherence.
- In the vertical direction, SSI responses exceed the fixed-base case in the frequency range 3–9 Hz. In the frequency range 9–14.5 Hz, the fixed-base responses exceed the SSI responses. Therefore, coherent SSI and incoherent SSI reduce peaks in the NP 2559 response spectra in the frequency range 9–14.5 Hz. The order of amplitudes is fixed-base, SSI coherent, and SSI incoherent.

Case 5: Rock site, U.S. NRC RG 1.60 enhanced in the high frequency range (10–20Hz) artificial time histories

Figures I–24– I–26 show the response spectra of the free-field ground motion with over-plots of the comparison of the response spectra calculated for NP 2559 by analyses of fixed-base, SSI coherent motion, and SSI incoherent motion for the X-, Y-, and Z-directions, respectively.

This conclusion for Case 2 El Centro and Case 4 applies to the RG 1.60 enhanced case:

- Low frequency input motion and responses in the horizontal directions are unaffected by incoherence.
- In the vertical direction, SSI responses exceed the fixed-base case in the frequency range 3–10 Hz. In the frequency range greater than 10 Hz, the fixed-base responses exceed those of the SSI coherent and incoherent. Therefore, the order

of amplitudes is fixed-base, SSI coherent, and SSI incoherent from 10 Hz to 100Hz.

I–4.2. Responses vs. elevation in KKNPP Unit 7 reactor building – Rock site

The second set of comparative results is focused on calculating responses as a function of elevation in the KKNPP Unit 7 reactor building for the following locations:

- Free-field ground motion;
- Foundation reference point (FRP) – with X, Y, Z coordinates[1] of (0.0,0.0,-13.7) (bottom of the foundation);
- Node point (NP) 1640 –with X, Y, Z coordinates of (-18.5,13.75,12.3) (1st floor); (denoted FP 1 in Figure I–9);
- Node point (NP) 2419 – with X, Y, Z coordinates of (-18.5,13.75,12.3) (3rd floor); (denoted FP 1 in Figure I–10);
- Node Point (NP) 2559 - with X, Y, Z coordinates of (--18.5, +13.75, 31.7) (denoted FP 1 in Figure I–11). It is located on the operating floor of the reactor building (Figure I–8).

The site profile is the uniform rock site (uniform half-space Vs = 2000m/s). Two sets of results are plotted: The El Centro earthquake (low frequency ground motion) and the Landers earthquake (high frequency ground motion) for the assumptions of SSI coherent ground motion, and SSI incoherent ground motion.

Case 6: Rock site, El Centro earthquake

Figures I–27–I–29 show the response spectra of the free-field ground motion with over-plots of the comparison of the response spectra at the FRP and NPs 1640, 2419, 2559 as analysed for SSI coherent motion, and SSI incoherent motion for the X-, Y-, and Z-directions, respectively.

In Figures I–27 and I–28, the X-and Y-direction responses for SSI coherent, and SSI incoherent are presented. The responses of interest are in the frequency range less than 10 Hz. No incoherent effects are observed as expected. SSI coherent and incoherent responses are the same or similar for the X- and Y-direction responses at all elevations.

In the Z-direction, the El Centro ground motion peaks at 10 Hz and is amplified at 10 Hz at all elevations. Reductions in the peak spectral accelerations at around 10 Hz due to SSI incoherent assumptions are observed.

At all locations (elevations):

- Low frequency input motion and responses in the horizontal directions are unaffected by incoherence.
- High frequency input and responses peak at 10 Hz and the SSI coherent SSI responses are reduced by assuming incoherent ground motions (SSI incoherent).

[1] All dimensions are in metres (m).

- The observations made for NP 2559 in Cases 2 and 4 hold for other locations in the structure.

Case 7: Rock site, Landers earthquake

Figures I–30, I–31, and I–32a show the response spectra of the free-field ground motion with over-plots of the comparison of the response spectra at the FRP and NPs 1640, 2419, 2559 as analysed for SSI coherent motion, and SSI incoherent motion for the X-, Y-, and Z-directions, respectively. In Fig. I–32a it is difficult to separate the SSI coherent and incoherent responses. Hence, Figures I–32b and I–32c contain only the SSI coherent and incoherent responses, respectively.

Note that the Z-direction responses for NPs 2419 and 2559 are essentially identical reflecting the fact that both are on a shear wall for which vertical dynamic amplification does not occur.

The same observations made for Case 1 apply herein:

- For the frequency range less than 15 Hz, responses in the horizontal directions are unaffected by incoherence;
- For the frequency range greater than 15 Hz, at most locations, the SSI incoherent responses in the horizontal directions are less than those of the SSI coherent;
- In the frequency range greater than 10 Hz, the SSI coherent responses are reduced by assuming incoherent ground motions (SSI incoherent);
- The observations made for NP 2559 in Case 1 hold for other locations in the structure.

I–4.3. Node Point (NP) 2559 (-18.5m, 13.75m, 31.7m) - soil site

As in the Cases 1–5, the third set of comparative results is focused on Node Point (NP) 2559 with X, Y, Z coordinates of (-18.5m, +13.75m, 31.7m) (denoted F1 in Figure I–11). It is located on the operating floor of the reactor building (Figure I–8). The fixed-base dynamic characteristics show no significant modes in the E-W (Y) direction apparently being located at the top of an E-W shear wall.

The site profile was assumed to be the uniform soil site (uniform half-space Vs = 305m/s). Two sets of results are plotted: the El Centro earthquake (low frequency ground motion), and the Landers earthquake (high frequency ground motion) for the assumptions of fixed-base, SSI coherent ground motion, and SSI incoherent ground motion.

Case 8: Soil site, Landers earthquake

Figures I–33– I–35 show the response spectra of the free-field ground motion with over-plots of the comparison of the response spectra calculated for NP 2559 by analyses of fixed-base, SSI coherent motion, and SSI incoherent motion for the X-, Y-, and Z-directions, respectively.

In the horizontal directions (X and Y), the free-field ground motion contains significant high frequency motion as discussed in Case 1 above. The fixed-base response provides insight into the important frequencies in the structure in the X and Y directions (again as discussed in Case 1). The SSI coherent and SSI incoherent responses show the significant effect of frequency shifts to the low frequencies (1.2 Hz (X) and 1.3 Hz (Y)) due to the SSI phenomena and soil-structure system behaviour.

SSI coherent and SSI incoherent responses for the horizontal directions at frequencies less than 12.6 Hz in the X-direction and over the complete frequency range for the Y direction are virtually identical. For frequencies greater than 12.6 Hz in the X-direction, very minor effects of incoherence are observed.

In the vertical direction, Figure I–35 shows a similar pattern for the Z-direction. The exception being in the frequency range 20–50Hz where the SSI incoherent response is less than the SSI coherent response by up to 30%. SSI phenomena have a very significant effect on the frequency characteristics of the response of the KKNPP Unit 7 reactor building when assumed to be founded on soil of Vs = 305m/s. Although, in general, incoherency has a minimal effect on the responses represented by response spectra at NP 2559, some reductions at high frequencies were observed.

Case 9: Soil site, El Centro earthquake

In Figures I–36 and I–37, the X-and Y-direction responses for fixed-base, SSI coherent, and SSI incoherent are presented. As noted in Case 8, the X and Y direction responses are at very low frequencies due to SSI effects. No incoherent effects are observed as expected. SSI coherent and incoherent responses are the same or similar for the X- and Y-direction responses.

In the Z-direction (Figure I–38), the El Centro ground motion peaks at 10 Hz and is deamplified at around 10 Hz due to SSI coherent and SSI incoherent behaviour. SSI incoherent responses are less than those of the SSI coherent analysis over the frequency range 7–40 Hz, but relatively minor reductions. Low frequency input motion and responses in the horizontal directions are unaffected by incoherence. High frequency input and responses (where high frequency includes the 10 Hz peak for the Z-direction in the free-field) are deamplified at 10 Hz due to SSI effects (coherent and incoherent).

I–5. CONCLUSIONS

(1) SSI (inertial and kinematic interaction) have been demonstrated to be important phenomena to take into account for generating the seismic demand for design and evaluation purposes of nuclear installations. Even for hard rock sites (Vs = 2000m/s), inertial interaction contributes to determining rock–structure natural frequencies. Kinematic interaction effects (local wave scattering effects, i.e., GMI) can significantly affect the seismic demand for structures, systems, and components for design and evaluation purposes.

(2) The effect of GMI on seismic response is a function of the ground motion frequency content, the site properties, and the structure.
(3) In general, GMI has minimal effects on seismic responses in frequency ranges less than 10Hz. This is verified in the current study for broad-banded artificial time histories and recorded ground motions of high frequency, low frequency, and a mixture of the two. Coherent and incoherent SSI responses are comparable in the frequency range less than 10Hz.
(4) In many instances, GMI has a more significant effect on vertical than horizontal responses. Nuclear installation structures often have multiple vertical modes with frequencies greater than 10Hz each having similar degrees of importance as measured by vertical modal mass. In contrast, important horizontal modes in nuclear installation structures are low frequency modes, i.e., frequencies less than 10Hz. In two ways, vertical responses are more likely to be affected by GMI than horizontal responses – multiple modes with frequencies greater than 10Hz and multiple modes with relatively close modal mass.
(5) The trend of GMI incoherence being important appears to be consistently the case for nodes at varying elevations.
(6) GMI can be important for soil sites as well as rock. However, for soil sites, the frequencies of interest of the soil-structure system in the horizontal directions are typically less than 10 Hz and often much less than 10Hz. Thereby, GMI being phenomena of frequencies greater than 10Hz lacks relevance. One exception is vertical modes that may be more local than overall modes and may be affected by GMI.

TABLE I–1. SEISMIC ANALYSES PERFORMED AND COMPARISIONS MADE

	Landers	Imperial Valley	Val-des-Bois	RG 1.60	RG 1.60 enhanced	Analyses
Fixed base	x	x	x	x	x	Coherent
Rock Site	x	x	x	x	x	Coherent and incoherent
Soil site	x	x	x	x	x	Coherent and incoherent
Total number of analyses	5	5	5	5	5	

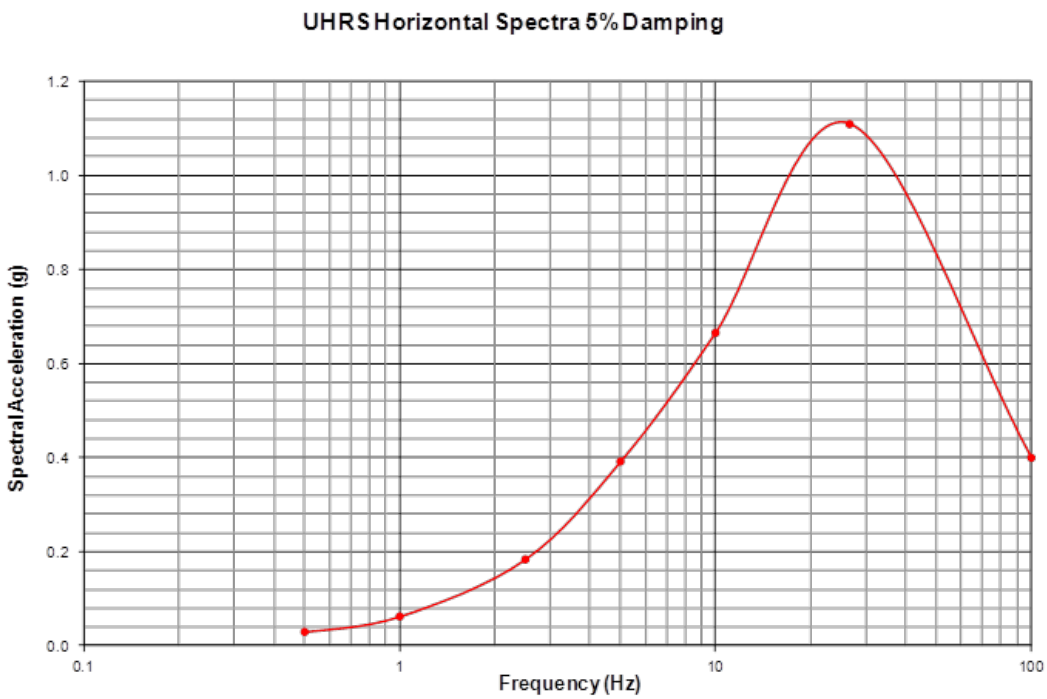

Fig. I–1. Uniform hazard response spectra (UHRS) – annual frequency of exceedance = 10^{-4} for a rock site in the U.S. (Courtesy of James J. Johnson and Associates).

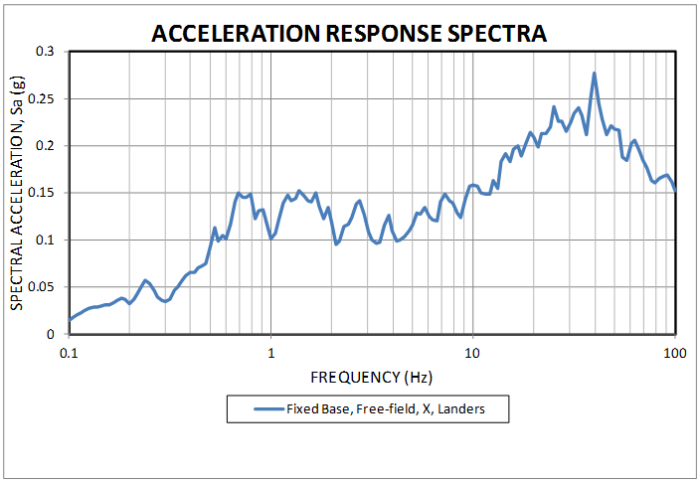

(a) X-direction

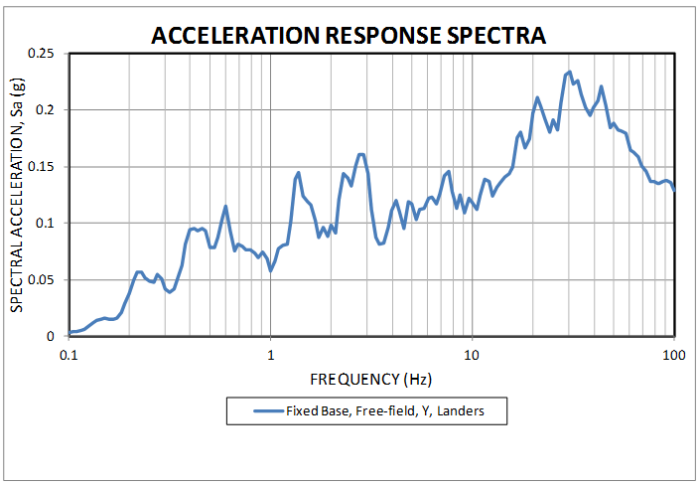

(b) Y-direction

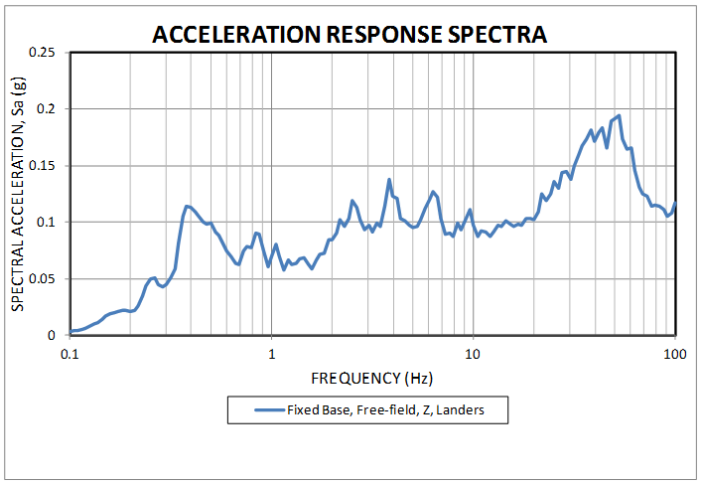

(c) Z-direction

Fig. I–2. Landers Earthquake M=7.3; June 28, 1992.

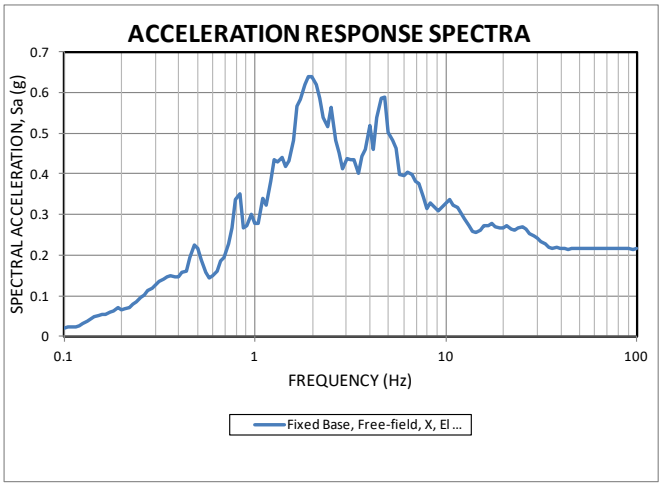

(a) X-direction

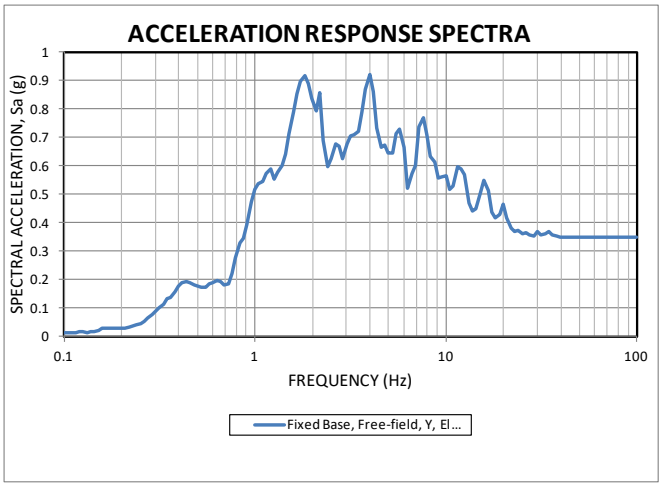

(b) Y-direction

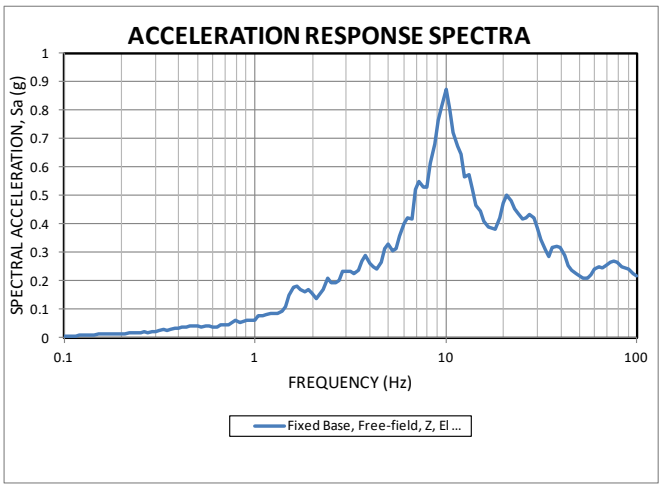

(c) Z-direction

Fig. I–3. Imperial Valley Earthquake M=6.9; May 18, 1940.

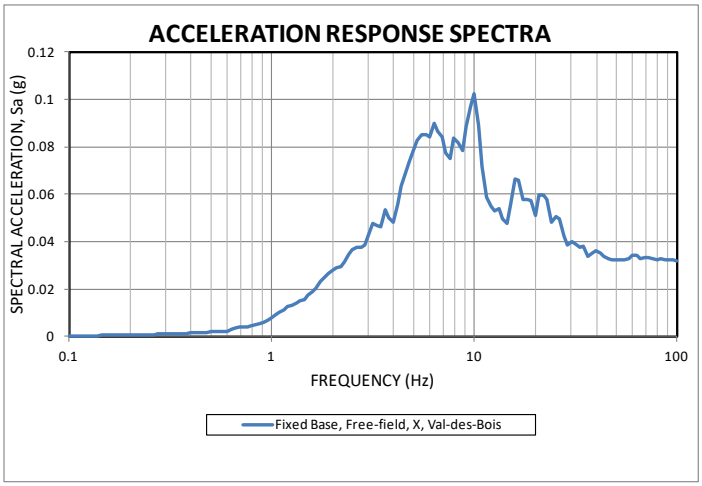

(a) X-direction

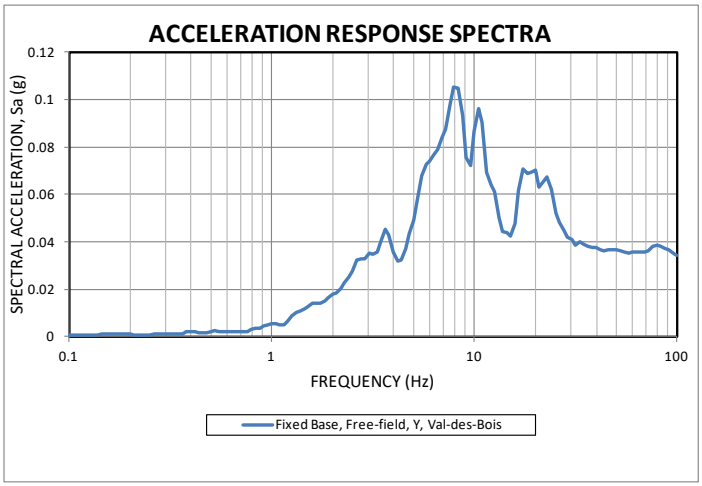

(b) Y-direction

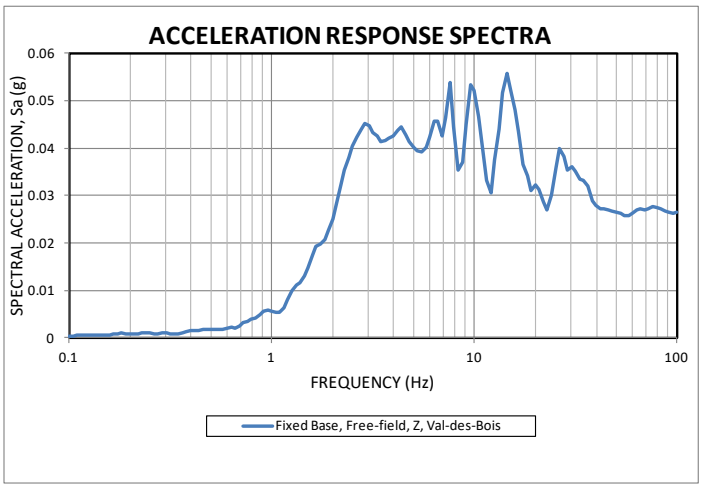

(c) Z-direction

Fig. I–4. Val-des-Bois earthquake, M=5.0, June 23, 2010.

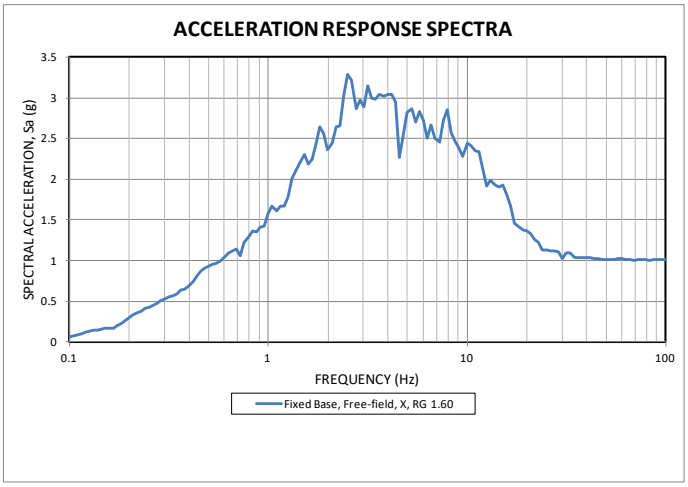

(a) X-direction

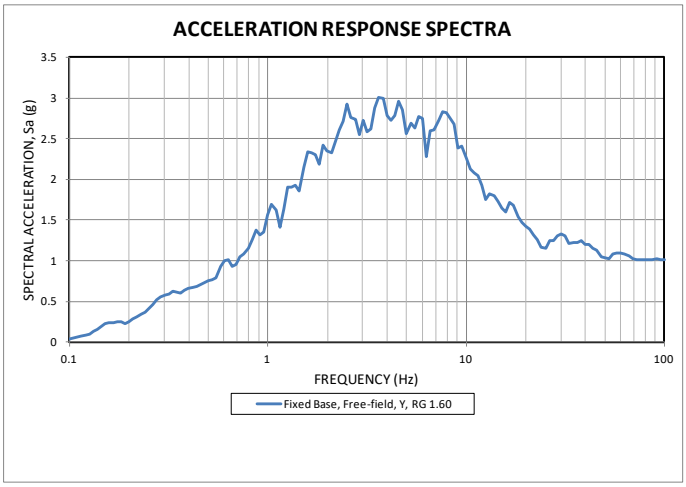

(b) Y-direction

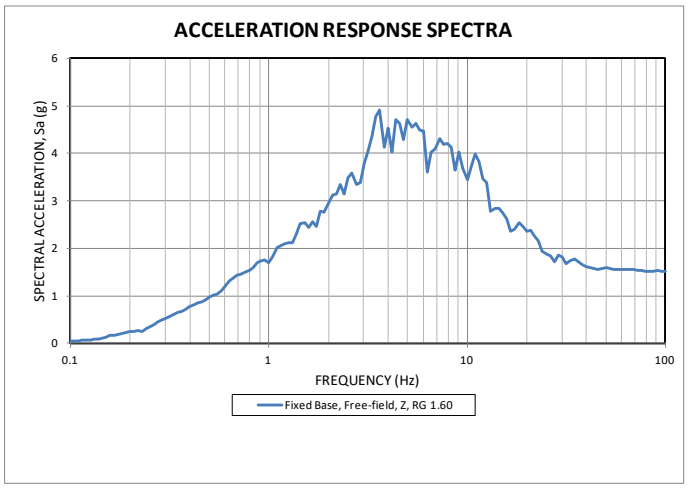

(c) Z-direction

Fig. I–5. U.S. NRC Regulatory Guide 1.60 artificial time histories.

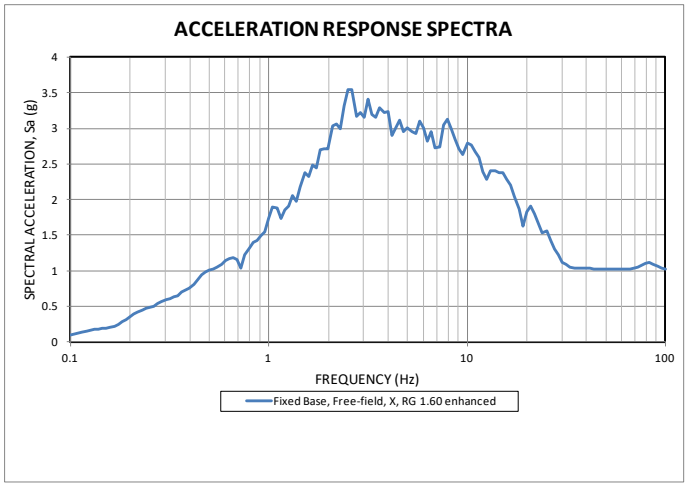

(a) X-direction

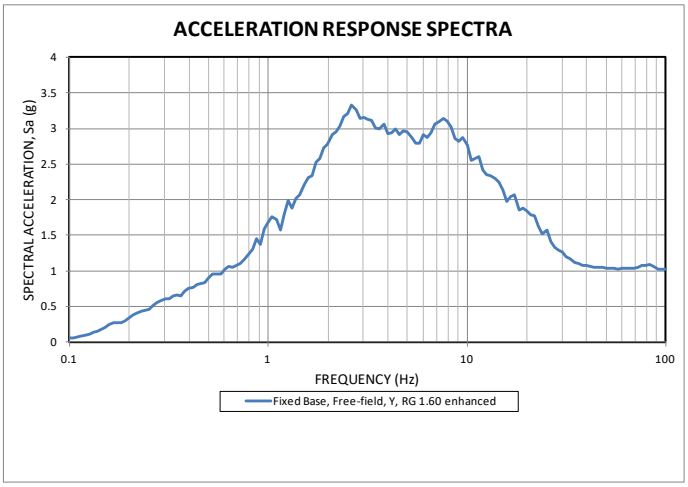

(b) Y-direction

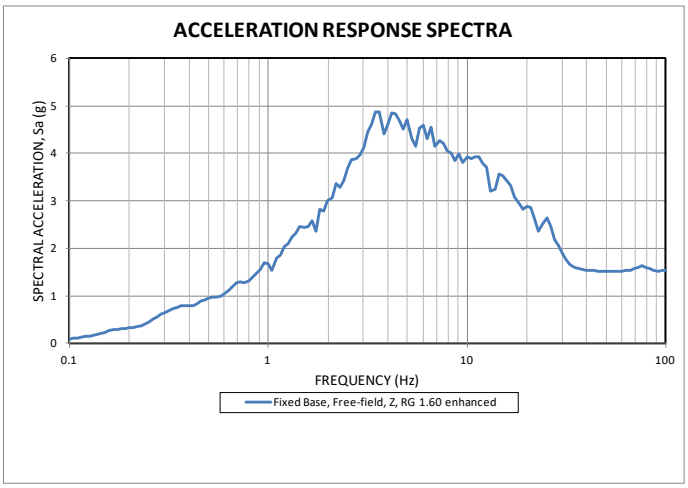

(c) Z-direction

Fig. I–6. U.S. NRC Regulatory Guide 1.60 enhanced artificial time histories.

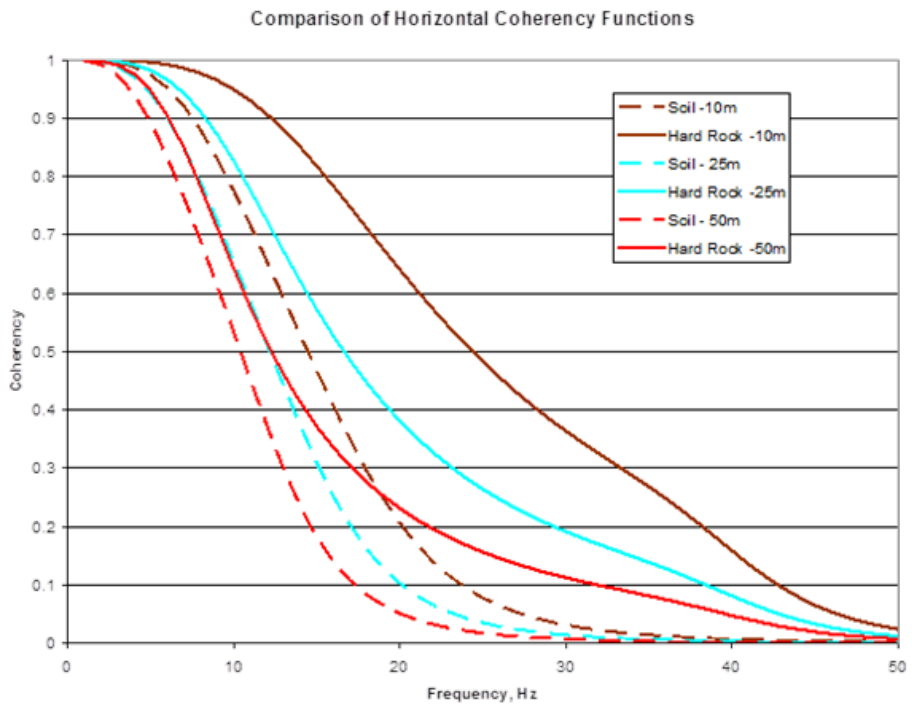

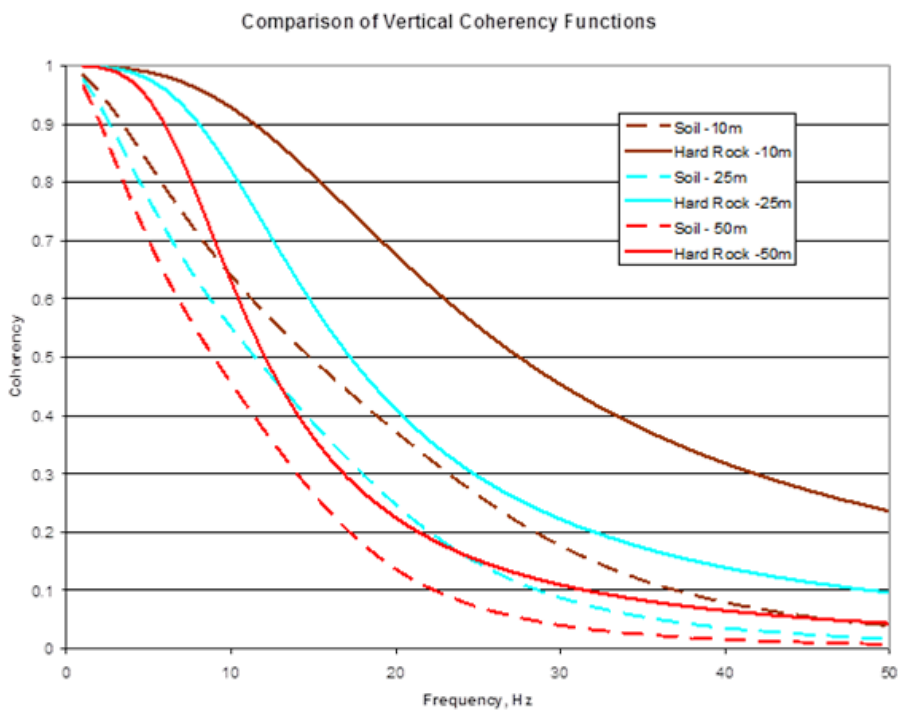

Fig. I–7. Comparison of ground motion coherency functions for soil and hard rock sites.

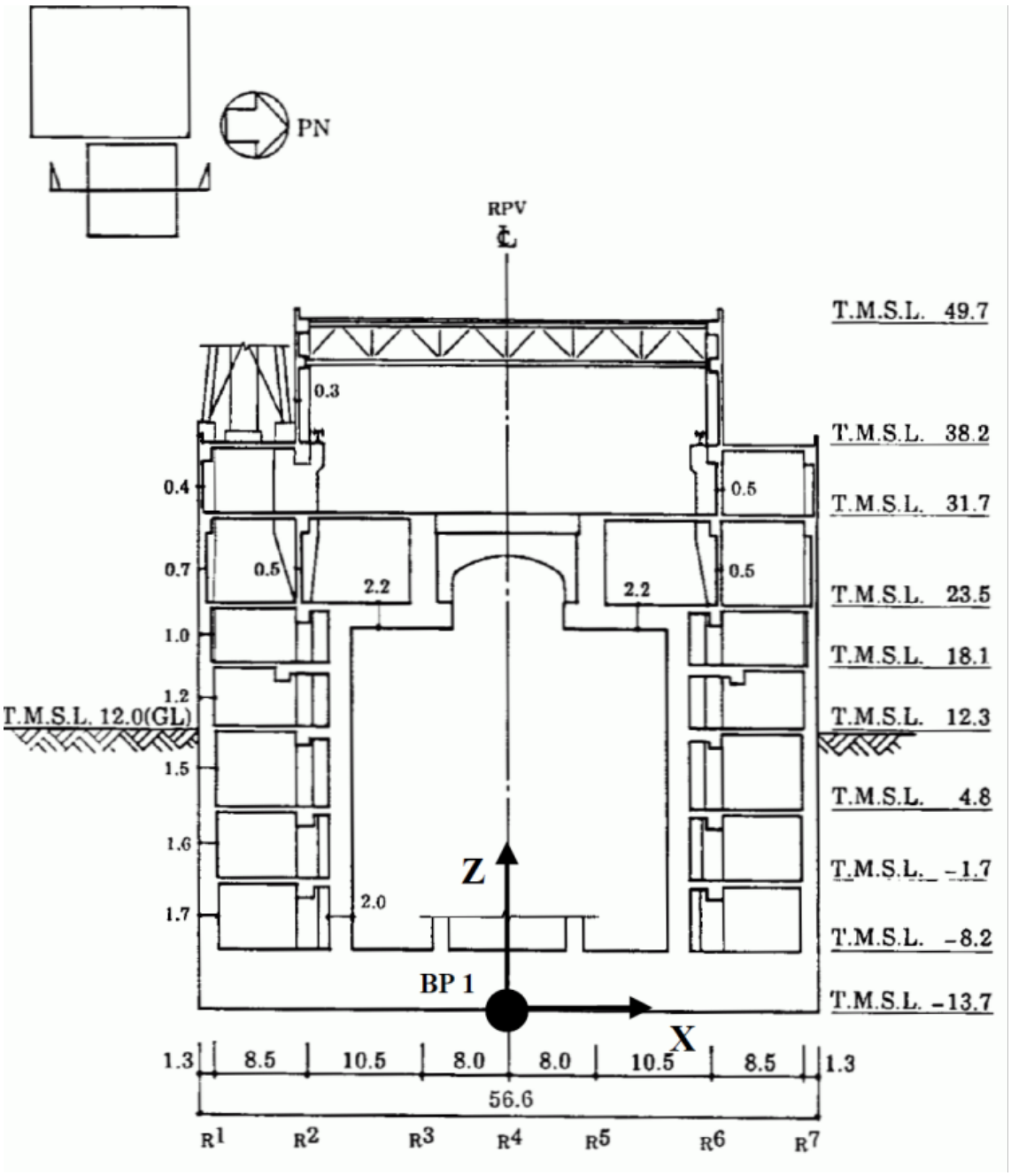

Fig. I–8. KKNPP Unit 7, reactor building cross section in N-S direction [6].

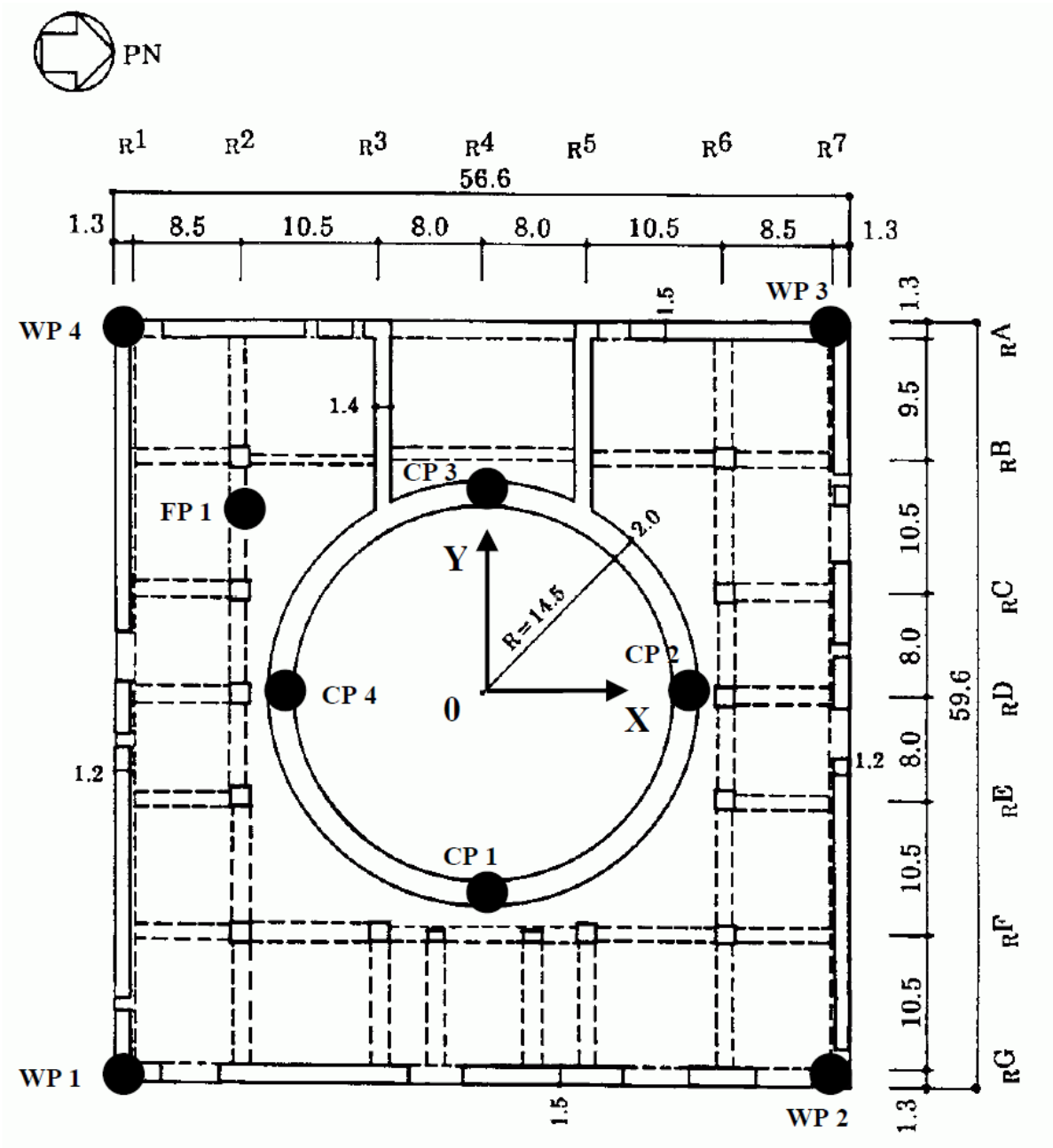

Fig. I–9. KKNPP Unit 7, reactor building plan view Elevation +12.3m [6].

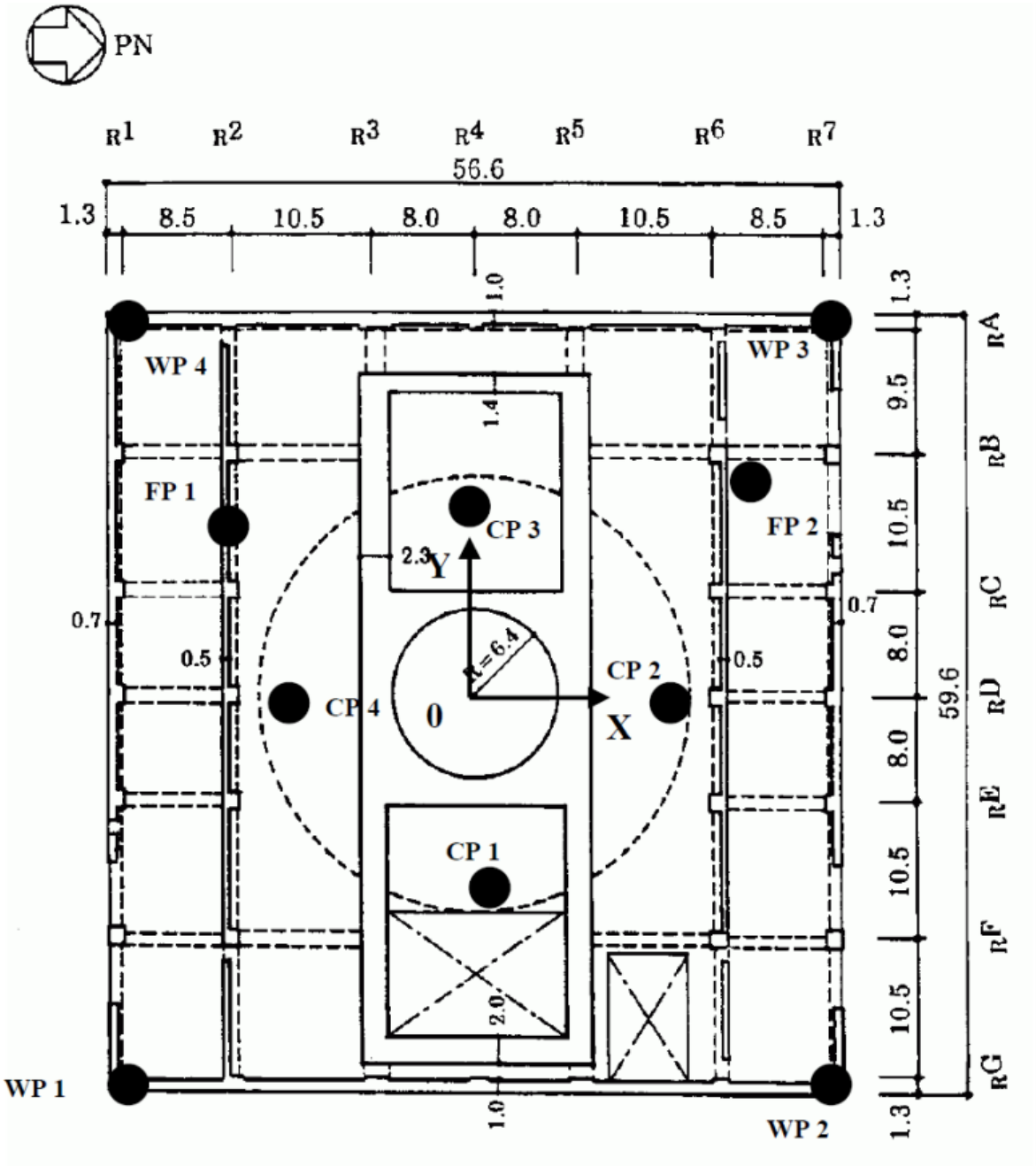

Fig. I–10. KKNPP Unit 7, reactor building plan view Elevation +23.5m [6].

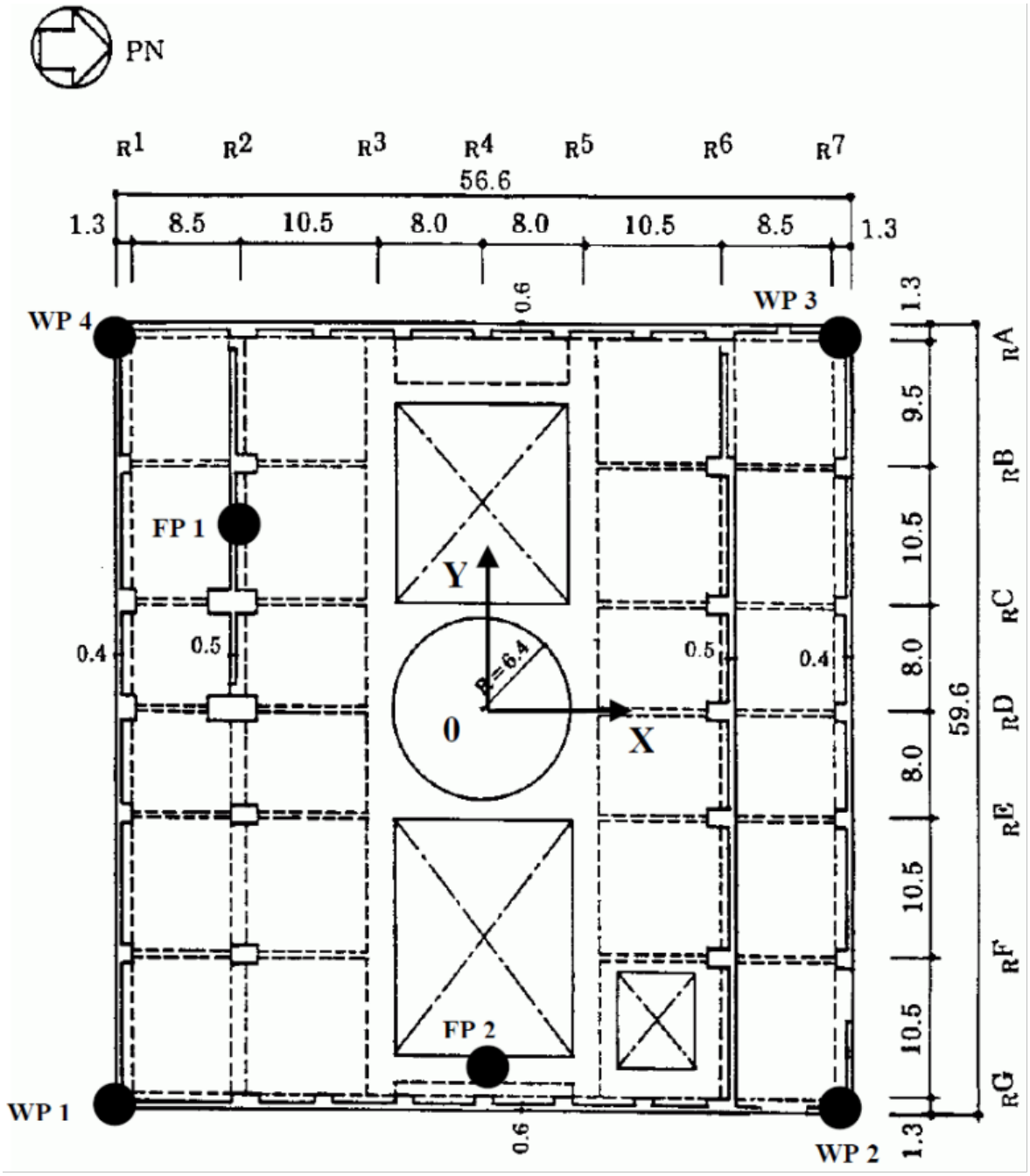

Fig. I–11. KKNPP Unit 7, reactor building plan view Elevation +31.7m [6].

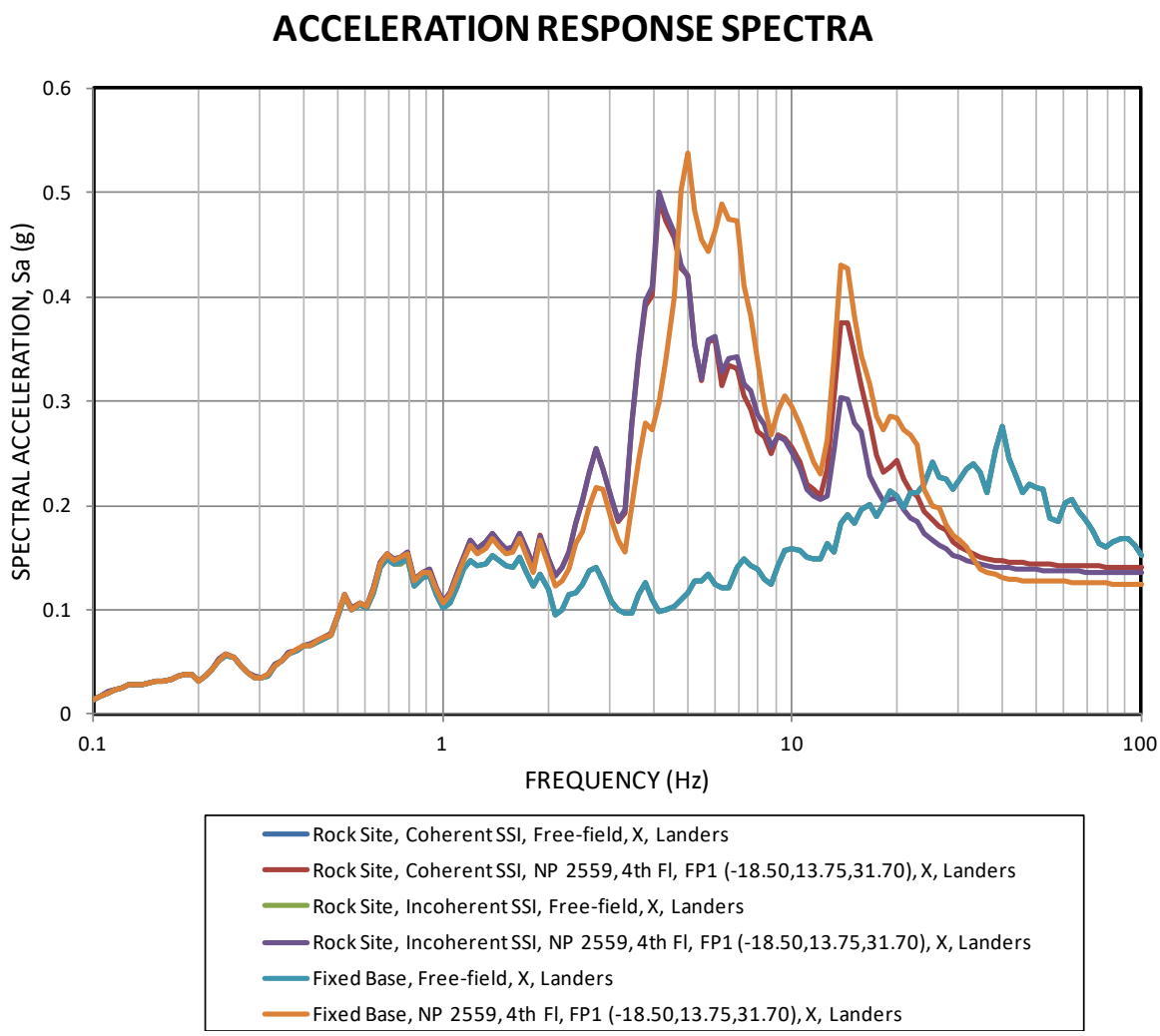

Fig. I–12. KKNPP Unit 7, reactor building, node point 2559, 4th floor; Landers earthquake; X (N-S) direction; fixed-base, coherent SSI, incoherent SSI.

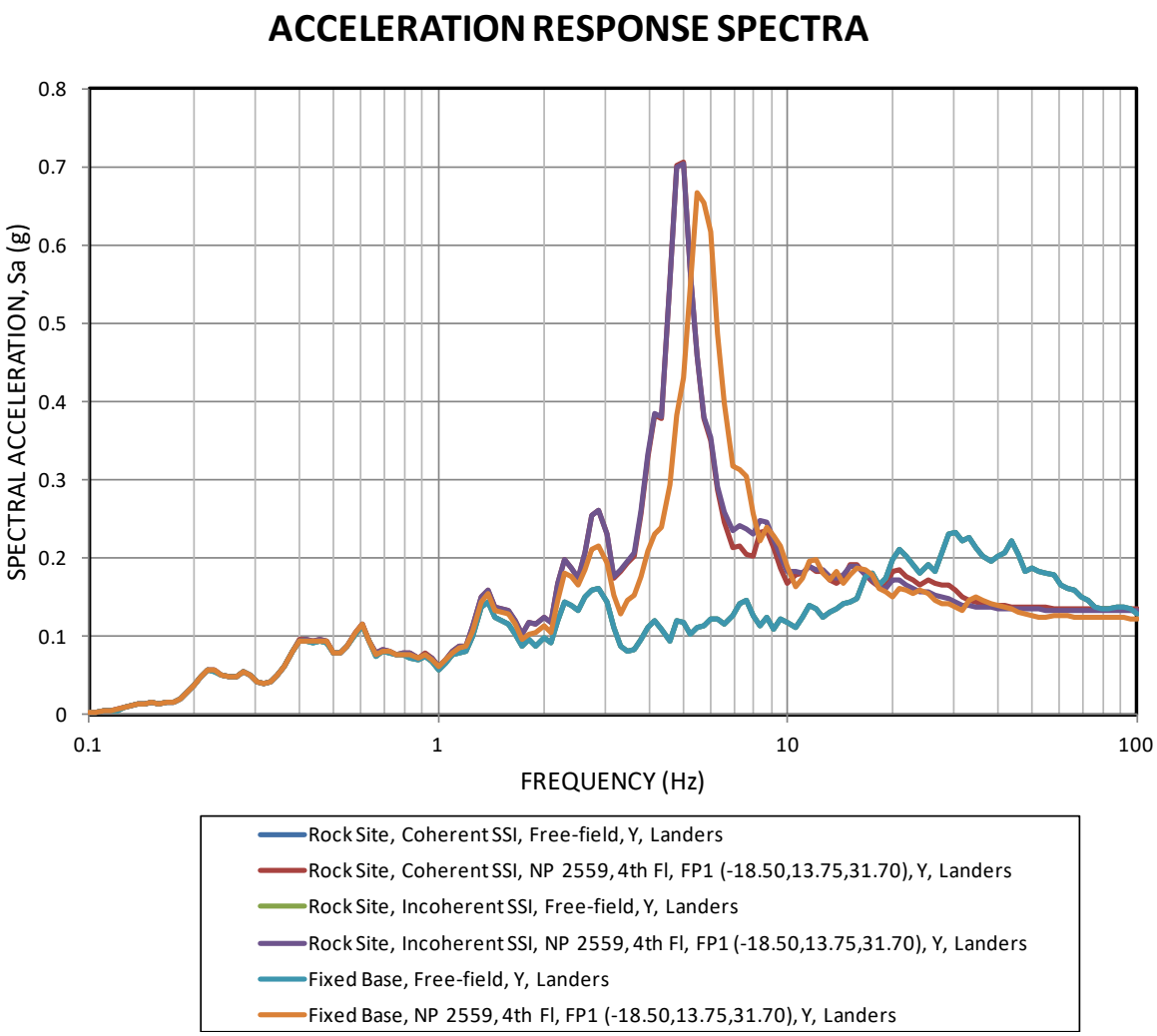

Fig. I–13. KKNPP Unit 7, reactor building, node point 2559, 4th floor; Landers earthquake; Y (E-W) direction; fixed-base, coherent SSI, incoherent SSI.

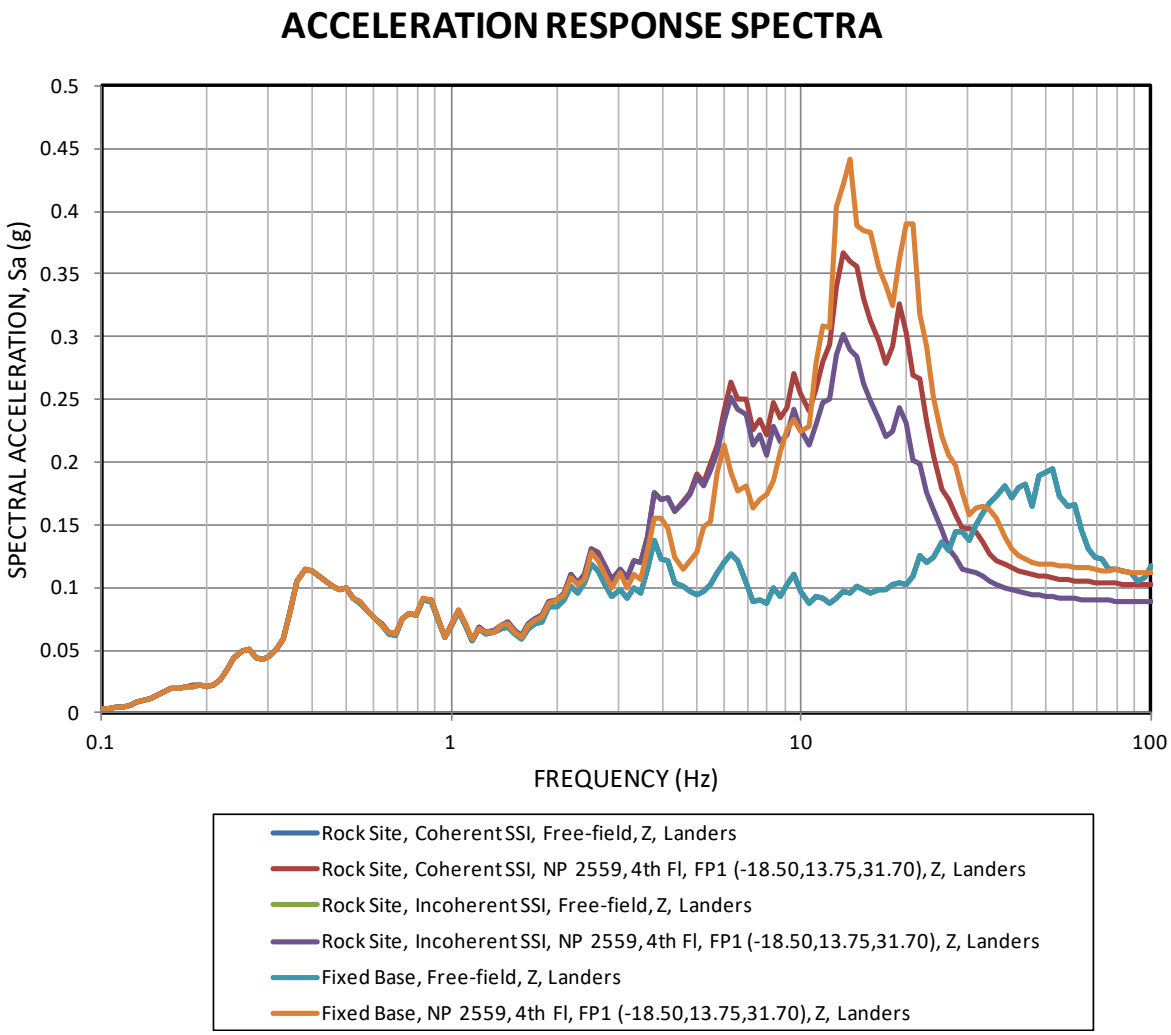

Fig. I–14. KKNPP Unit 7, reactor building, node point 2559, 4th floor; Landers earthquake; Z (Vertical) direction; fixed-base, coherent SSI, incoherent SSI.

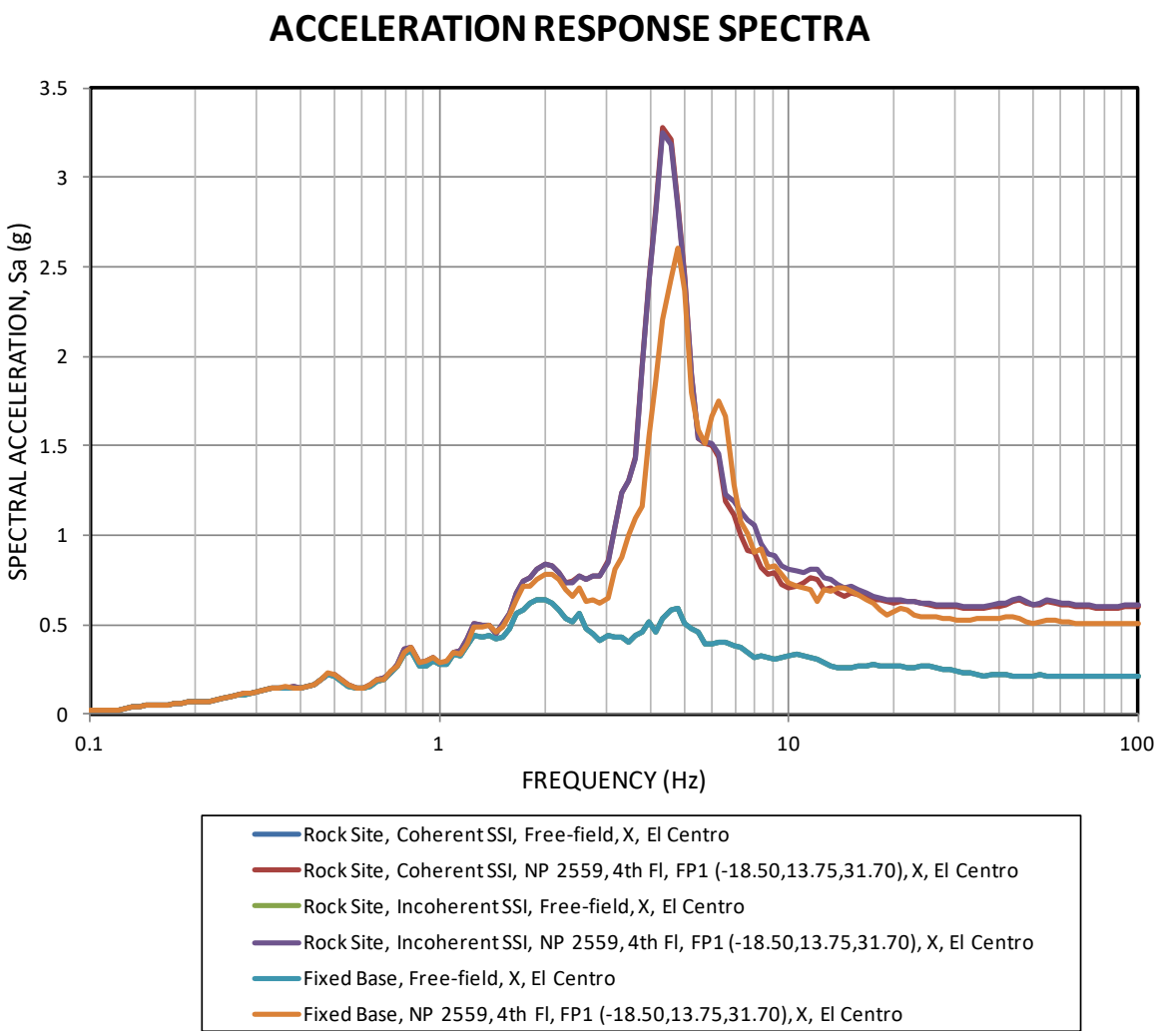

Fig. I–15. KKNPP Unit 7, reactor building, node point 2559, 4th floor; El Centro earthquake; X (N-S) – direction; fixed-base, coherent SSI, incoherent SSI.

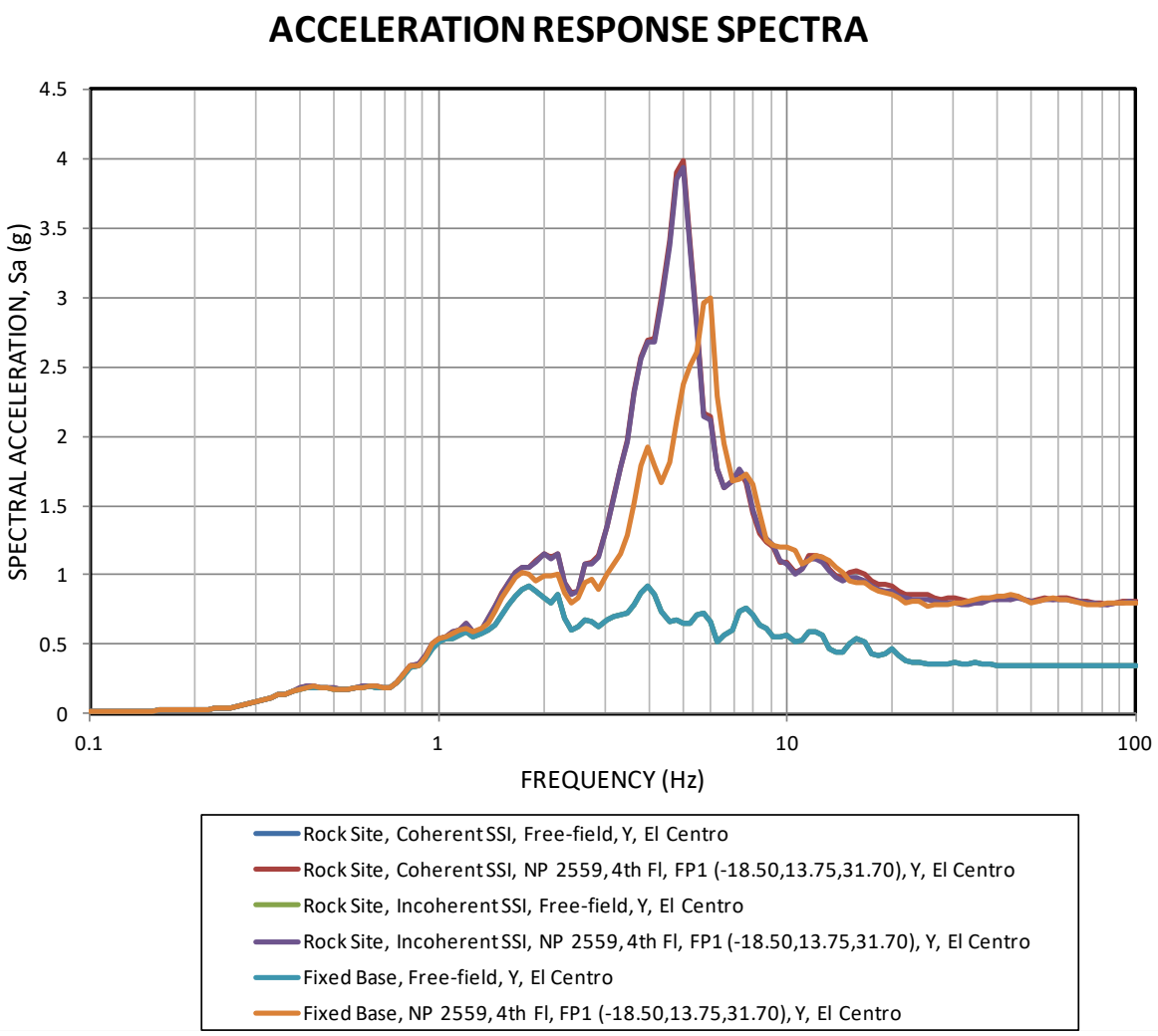

Fig. I–16. KKNPP Unit 7, reactor building, node point 2559, 4th floor; El Centro earthquake; Y(E-W) direction; fixed-base, coherent SSI, incoherent SSI.

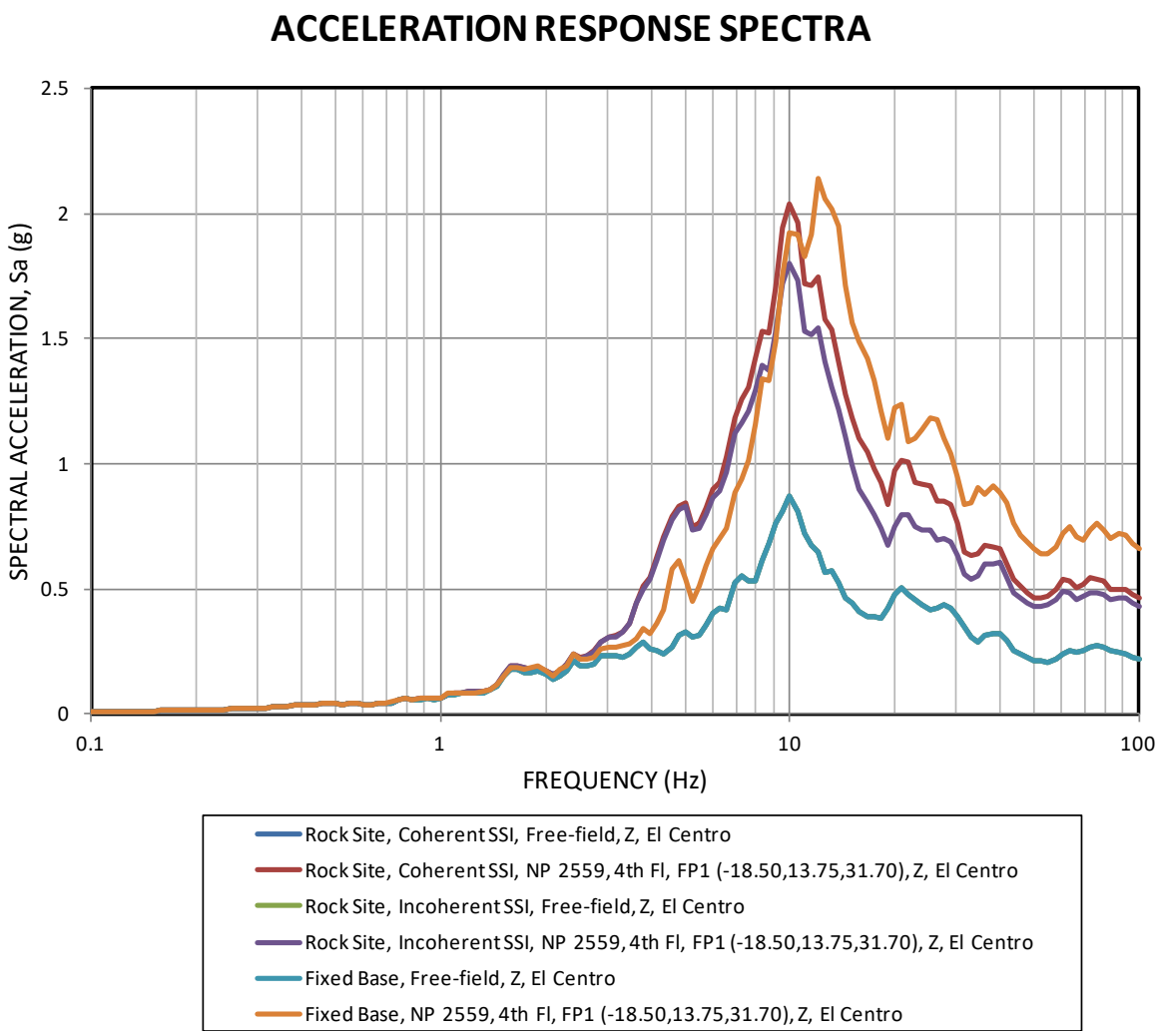

Fig. I–17. KKNPP Unit 7, reactor building, node point 2559, 4th floor; El Centro earthquake; Z (Vertical) - direction; fixed-base, coherent SSI, incoherent SSI.

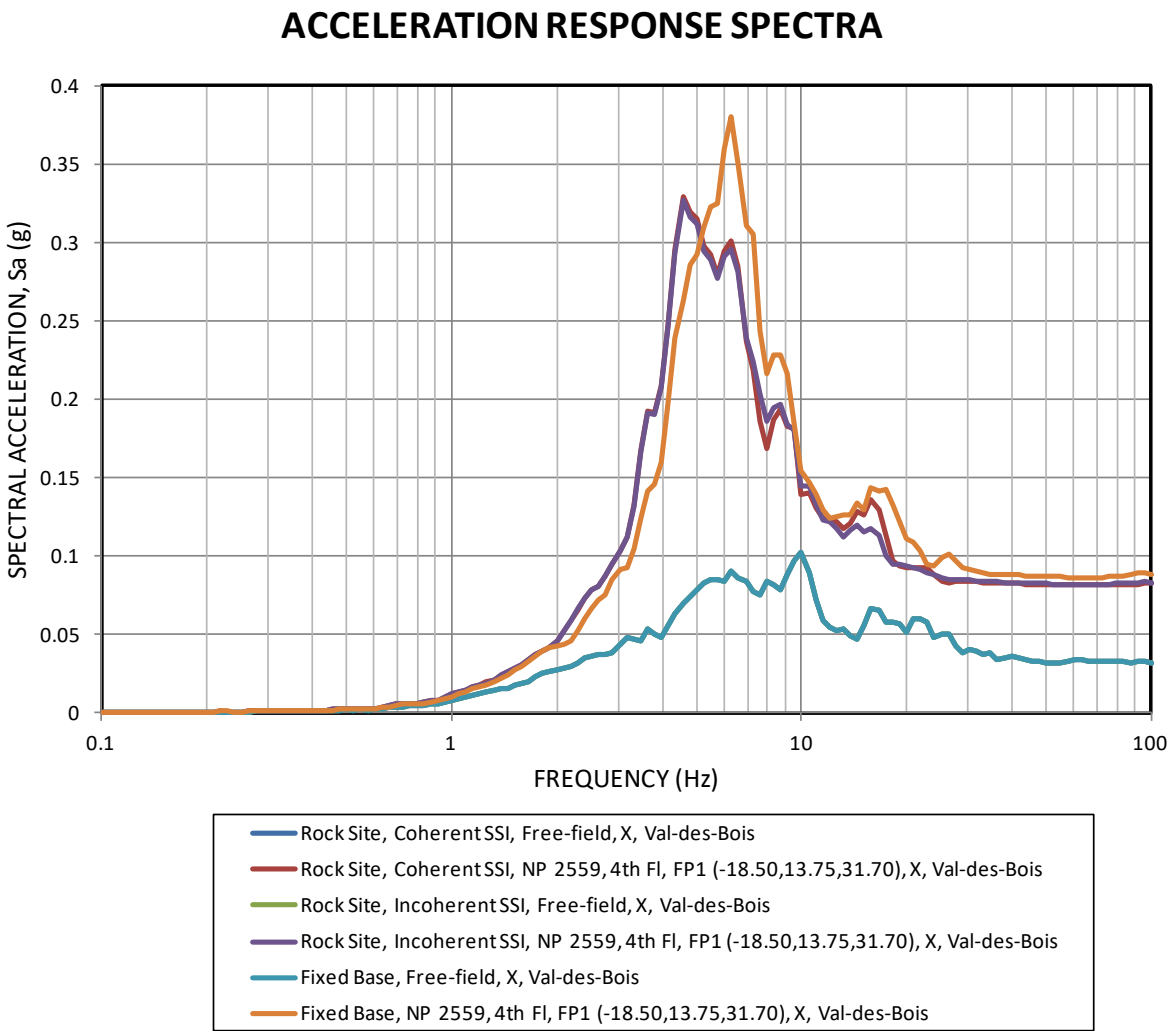

Fig. I–18. KKNPP Unit 7, reactor building, node point 2559, 4th floor; Val-des-Bois earthquake; X (N - S)- direction; fixed-base, coherent SSI, incoherent SSI.

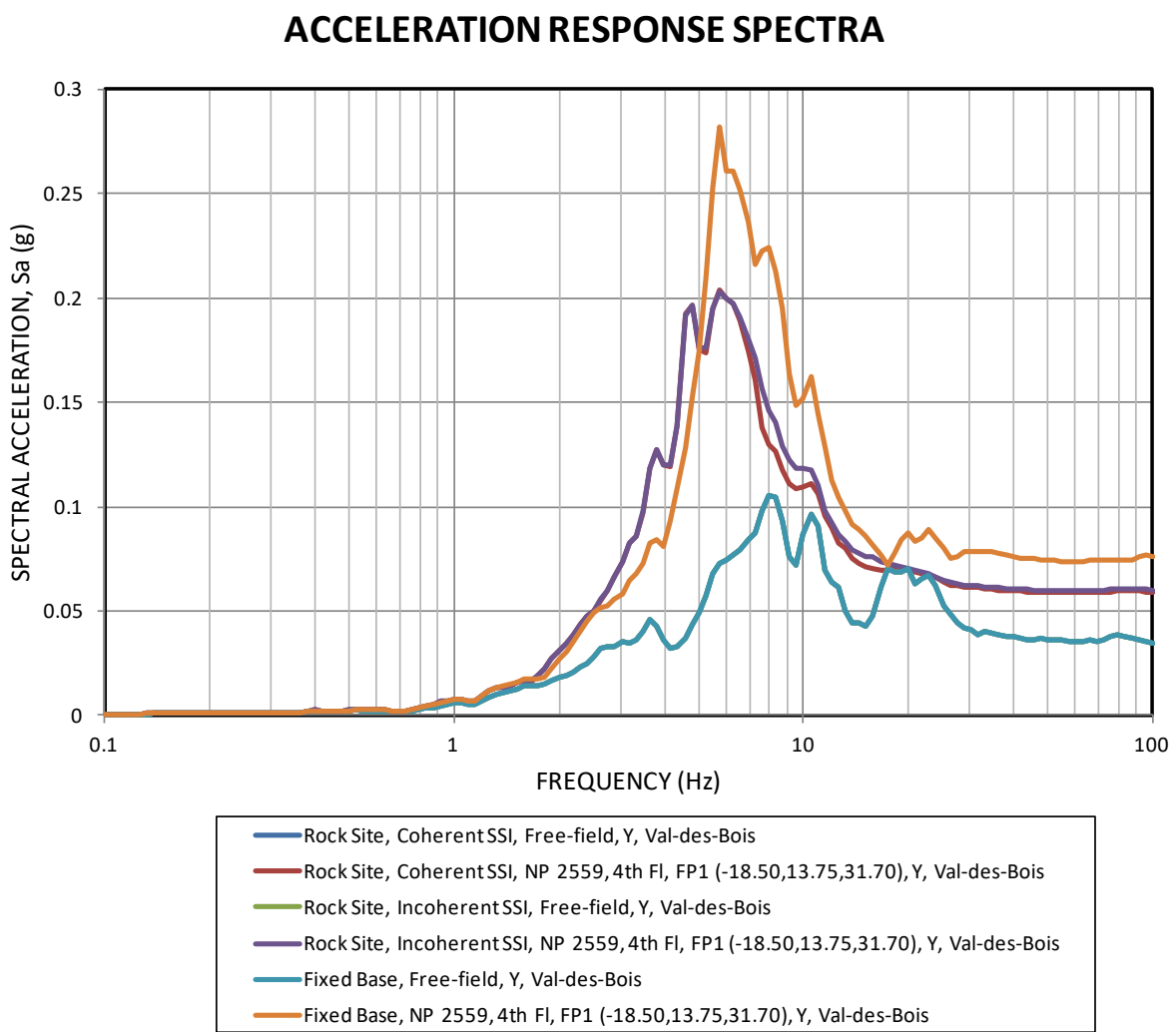

Fig. I–19. KKNPP Unit 7, reactor building, node point 2559, 4th floor; Val-des-Bois earthquake; Y (E-W) direction; fixed-base, coherent SSI, incoherent SSI.

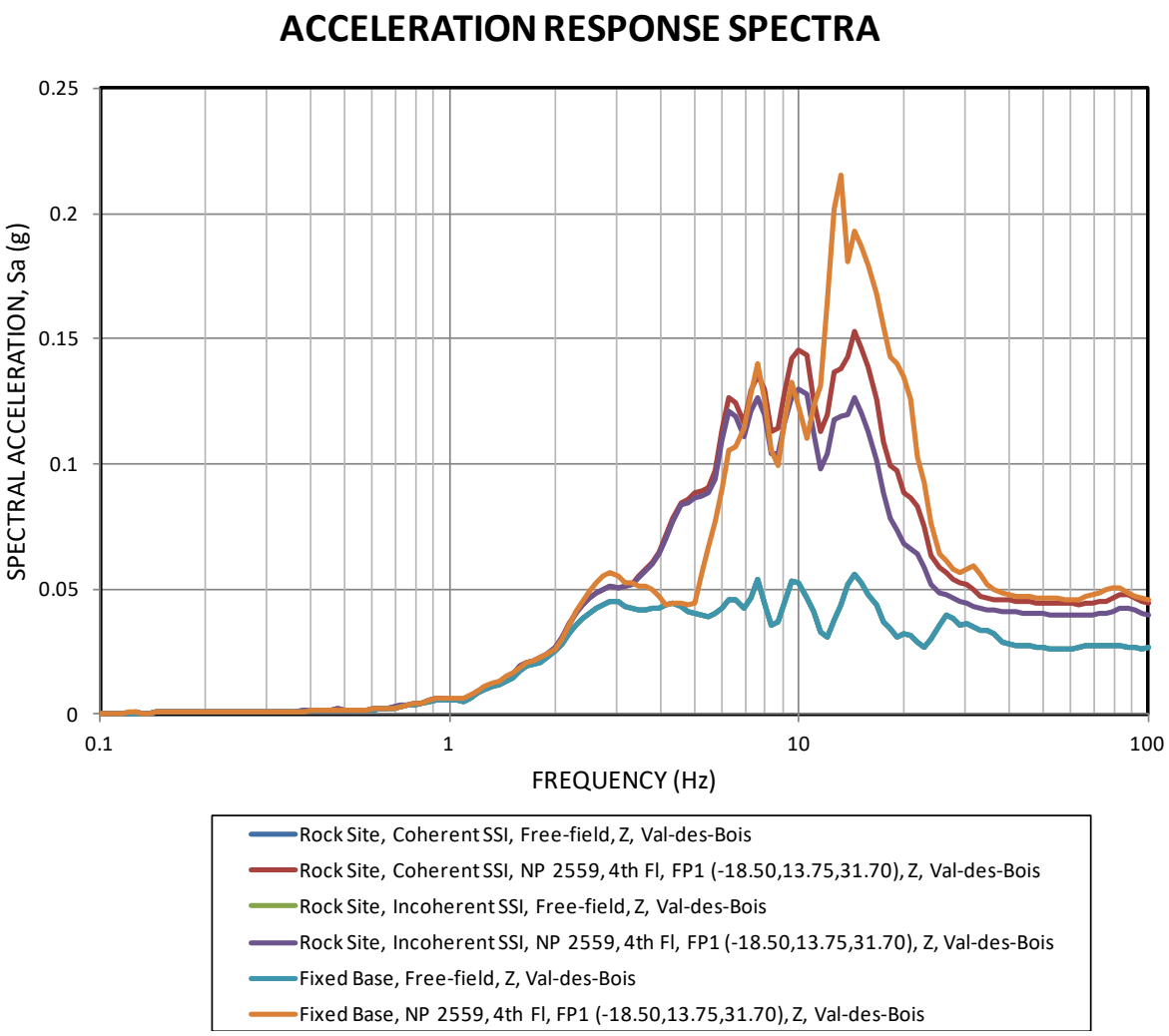

Fig. I–20. KKNPP Unit 7, reactor building, node point 2559, 4th floor; Val-des-Bois earthquake; Z (Vertical)-direction; fixed-base, coherent SSI, incoherent SSI.

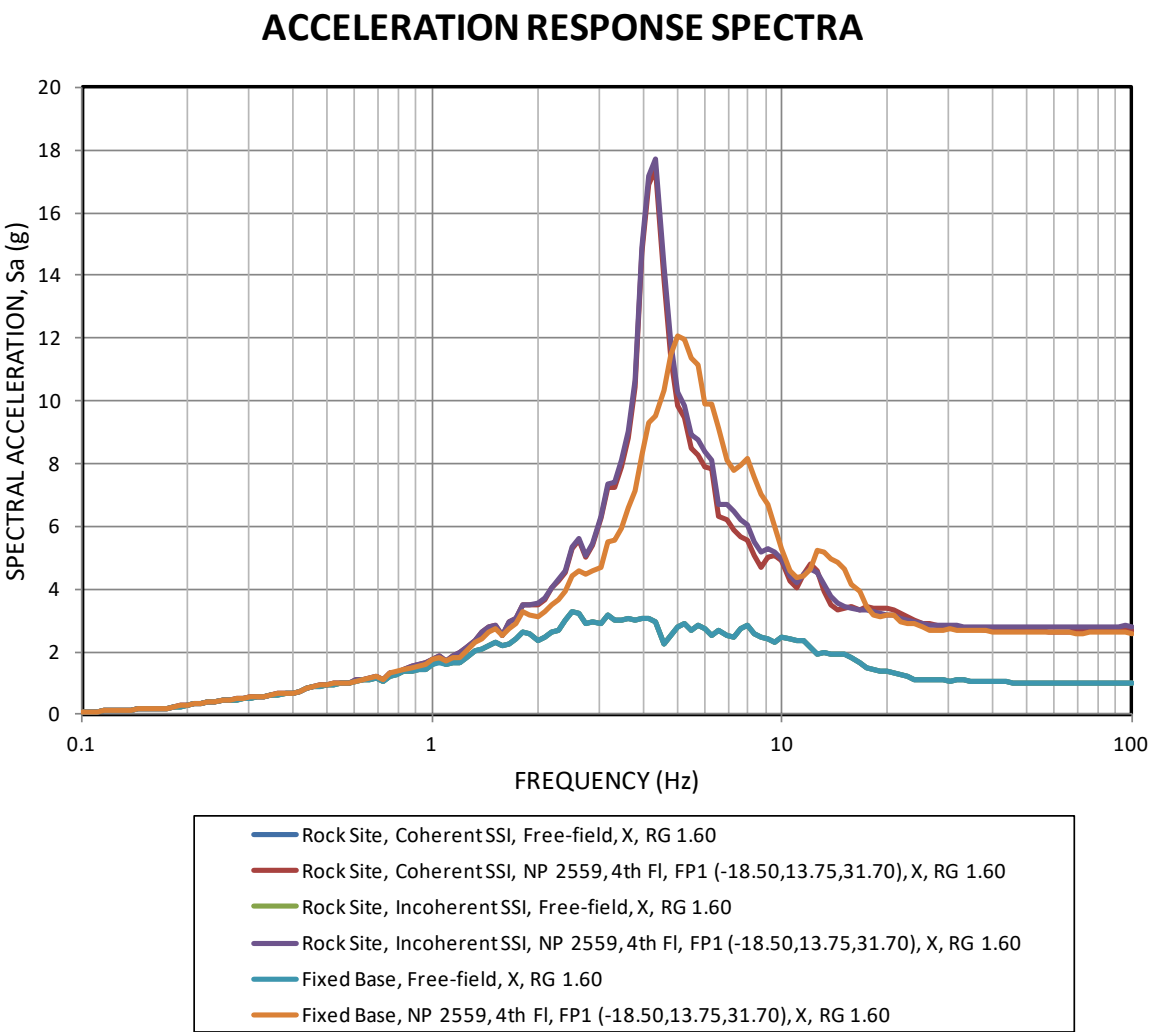

Fig. I–21. KKNPP Unit 7, reactor building, node point 2559, 4th floor; RG 1.60; X (N-S) - direction; fixed-base, coherent SSI, incoherent SSI.

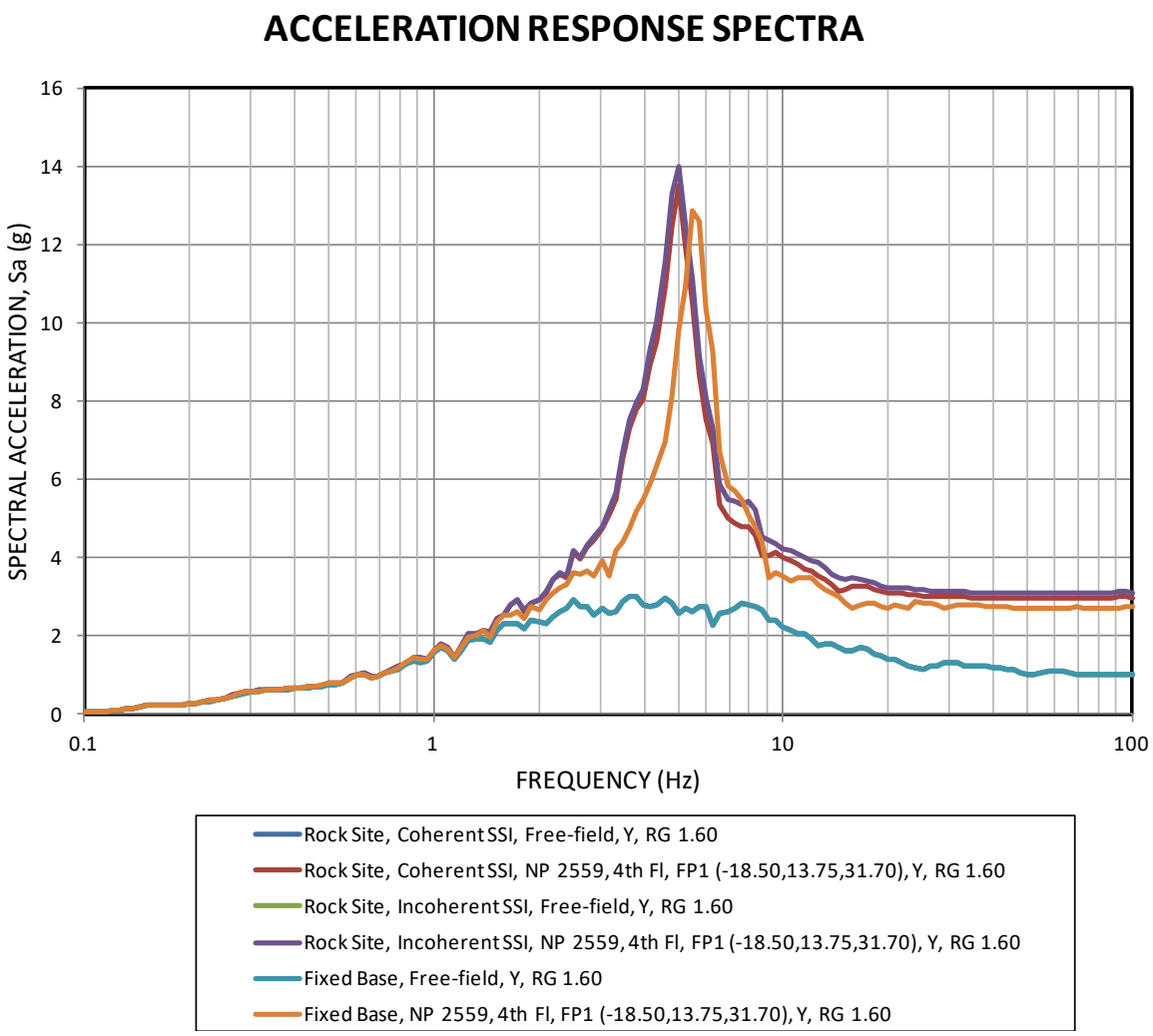

Fig. I–22. KKNPP Unit 7, reactor building, node point 2559, 4th floor; RG 1.60; Y(E-W) - direction; fixed-base, coherent SSI, incoherent SSI.

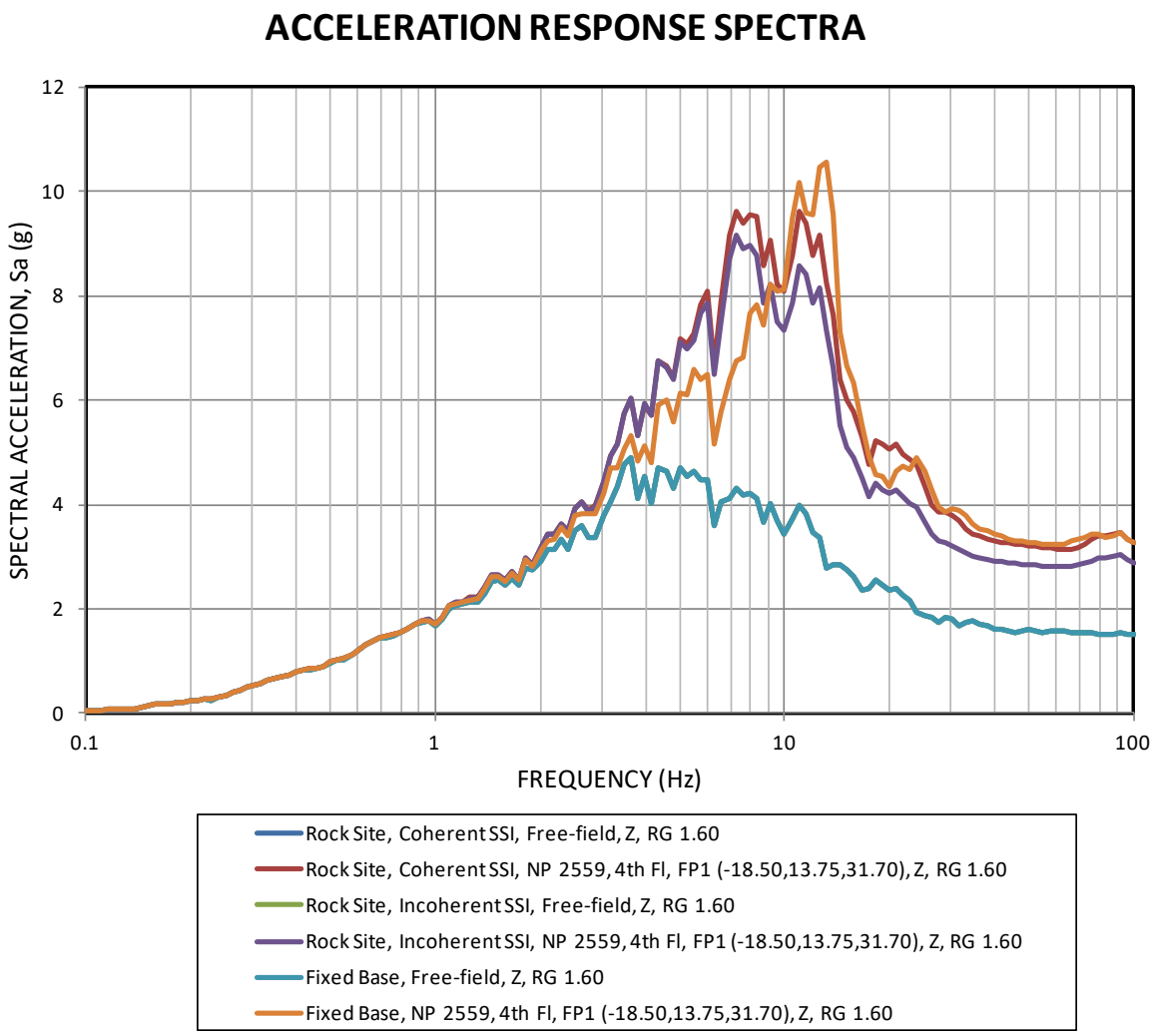

Fig. I–23. KKNPP Unit 7, reactor building, node point 2559, 4th floor; RG 1.60; Z (Vert) - direction; fixed-base, coherent SSI, incoherent SSI.

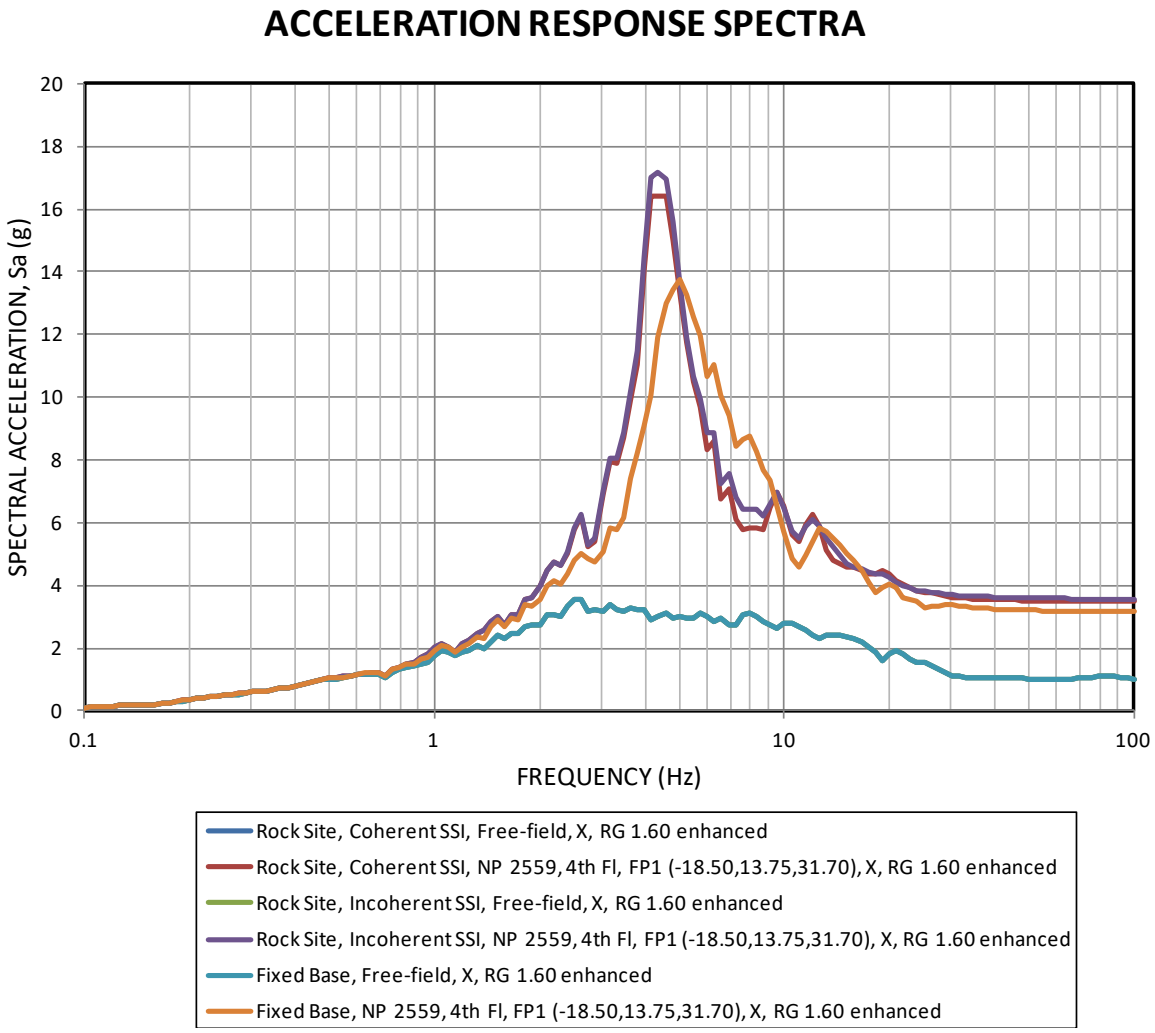

Fig. I–24. KKNPP Unit 7, reactor building, node point 2559, 4th floor; RG 1.60, enhanced; X(N-S)-direction; fixed-base, coherent SSI, incoherent SSI.

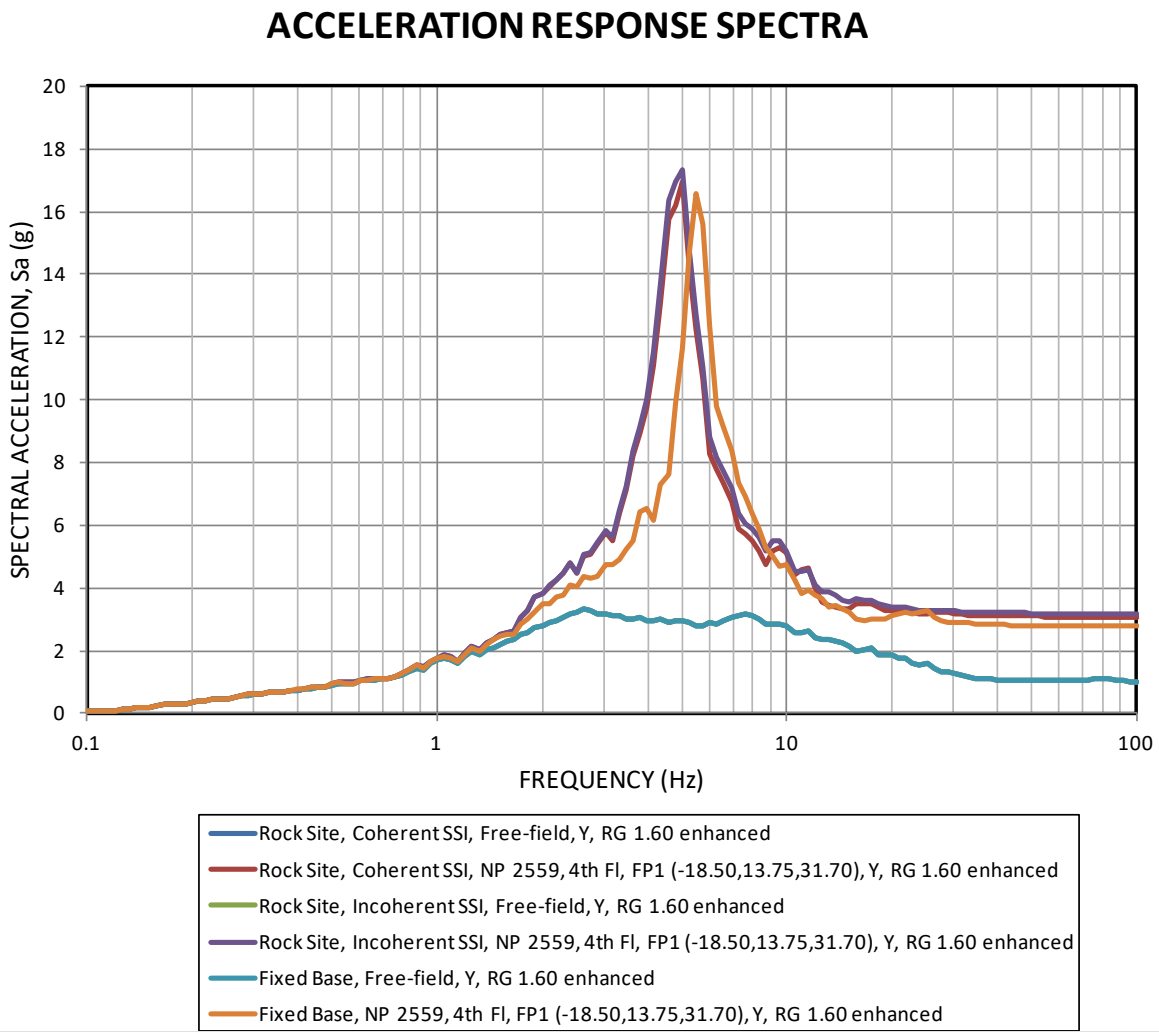

Fig. I–25. KKNPP Unit 7, reactor building, node point 2559, 4th floor; RG 1.60, enhanced; Y(E-W) direction; fixed-base, coherent SSI, incoherent SSI.

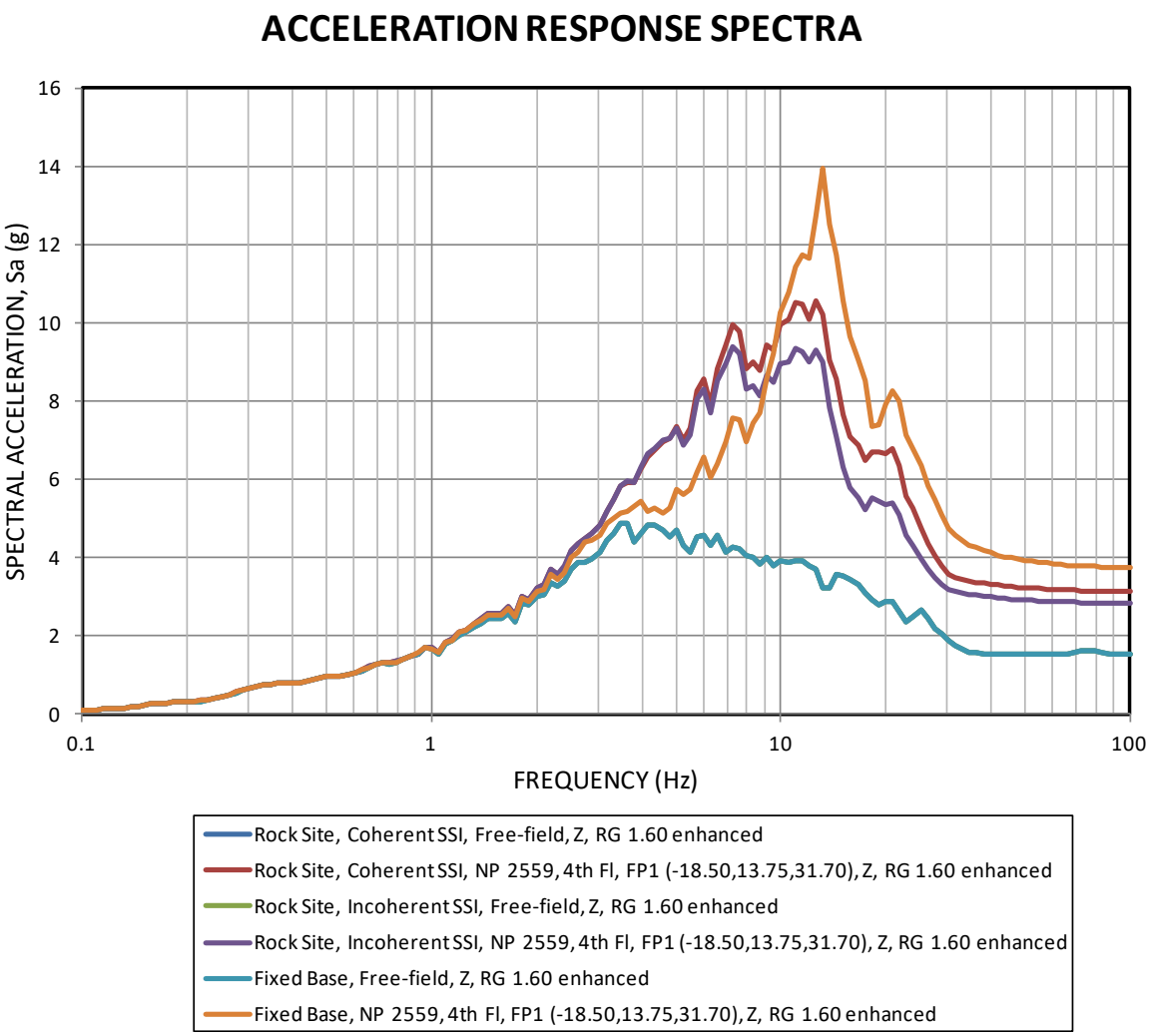

Fig. I–26. KKNPP Unit 7, reactor building, node point 2559, 4th floor; RG 1.60, enhanced; Z(Vert) direction; fixed-base, coherent SSI, incoherent SSI.

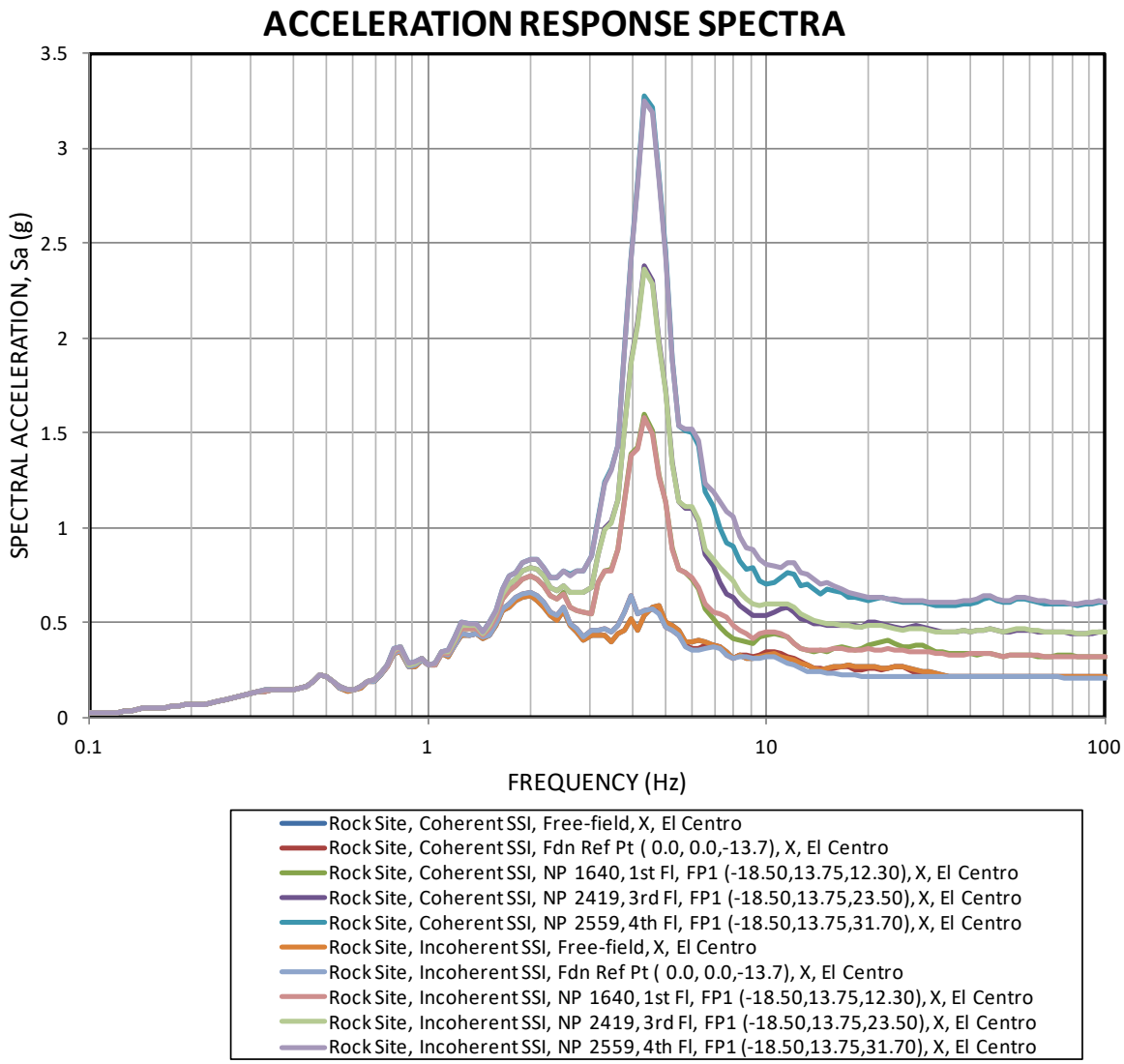

Fig. I–27. KKNPP Unit 7, reactor building, node points: 2559, 4th floor; 2419, 3rd floor; 1640, 1st floor; foundation ref. point; free-field; El Centro earthquake; X(N-S)-direction; coherent SSI, incoherent SSI.

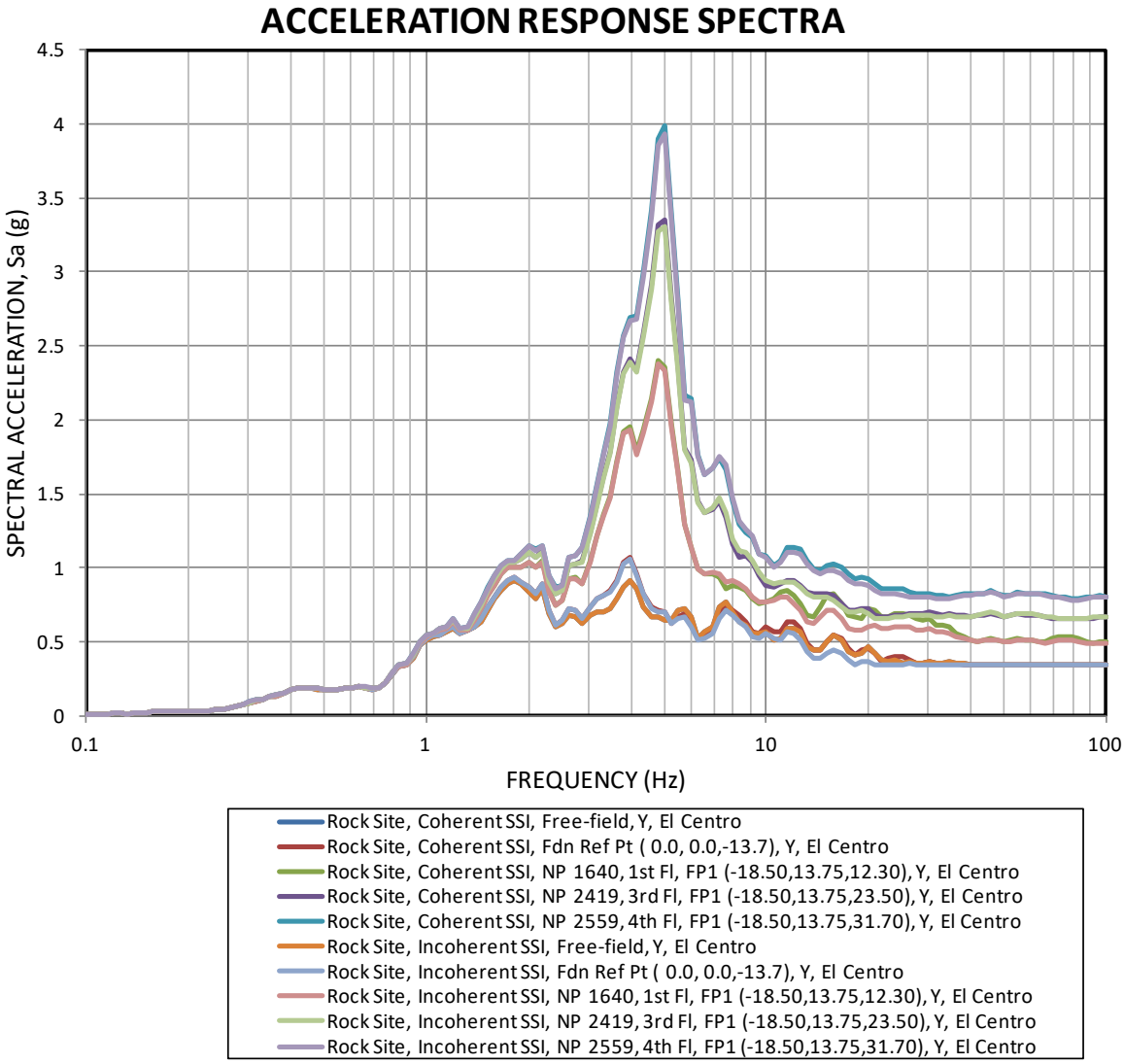

Fig. I–28. KKNPP Unit 7, reactor building, node points: 2559, 4th floor; 2419, 3rd floor; 1640, 1st floor; foundation ref. point; El Centro earthquake; Y (E-W) - direction; coherent SSI, incoherent SSI.

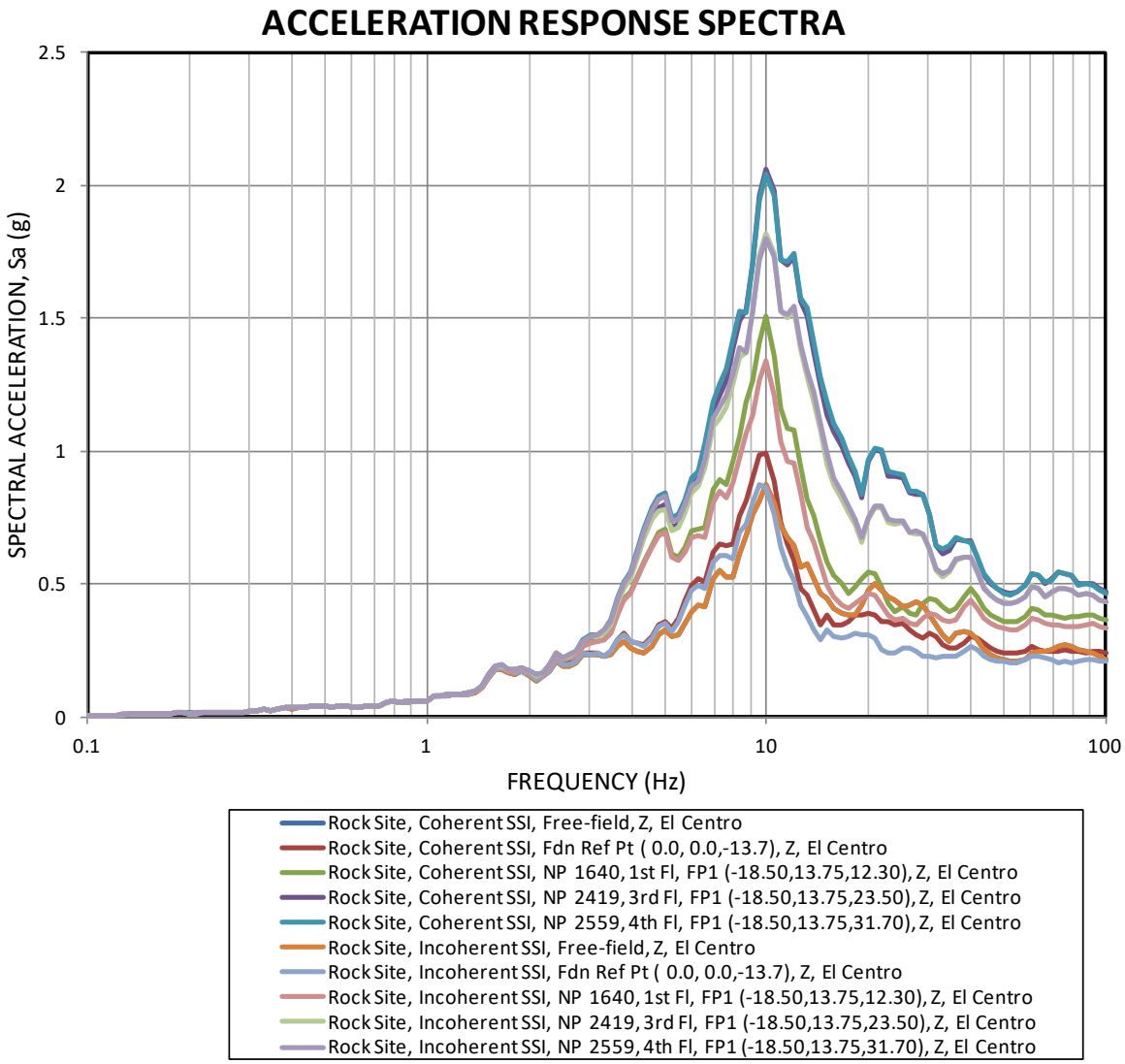

Fig. I–29. KKNPP Unit 7, reactor building, node points: 2559, 4th floor; 2419, 3rd floor; 1640, 1st floor; foundation ref. point; El Centro earthquake; Z(Vert)-direction; coherent SSI, incoherent SSI.

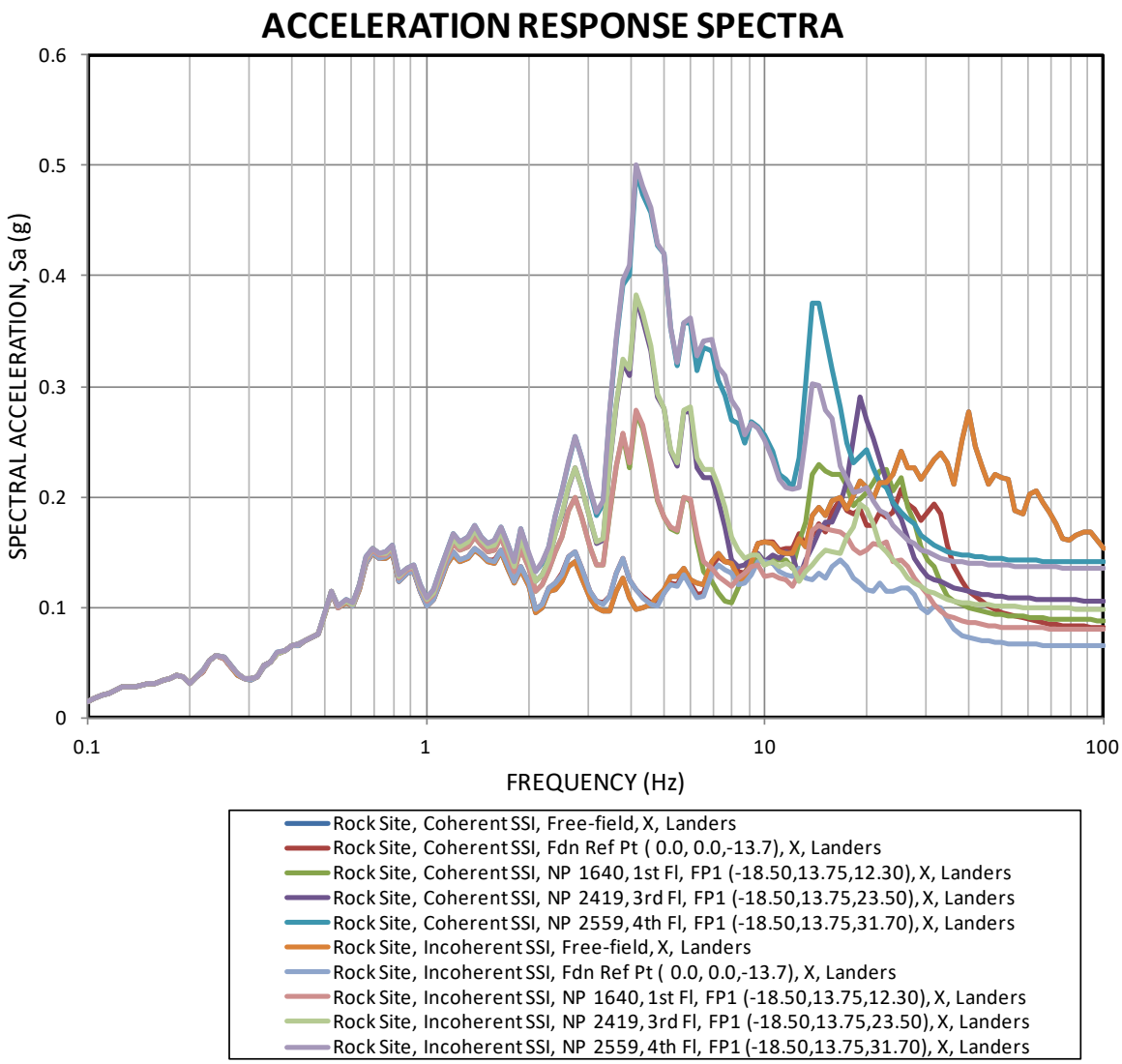

Fig. I–30. KKNPP Unit 7, reactor building, node points: 2559, 4th floor; 2419, 3rd floor; 1640, 1st floor; foundation ref. point; Landers earthquake; X(N-S)-direction; coherent SSI, incoherent SSI.

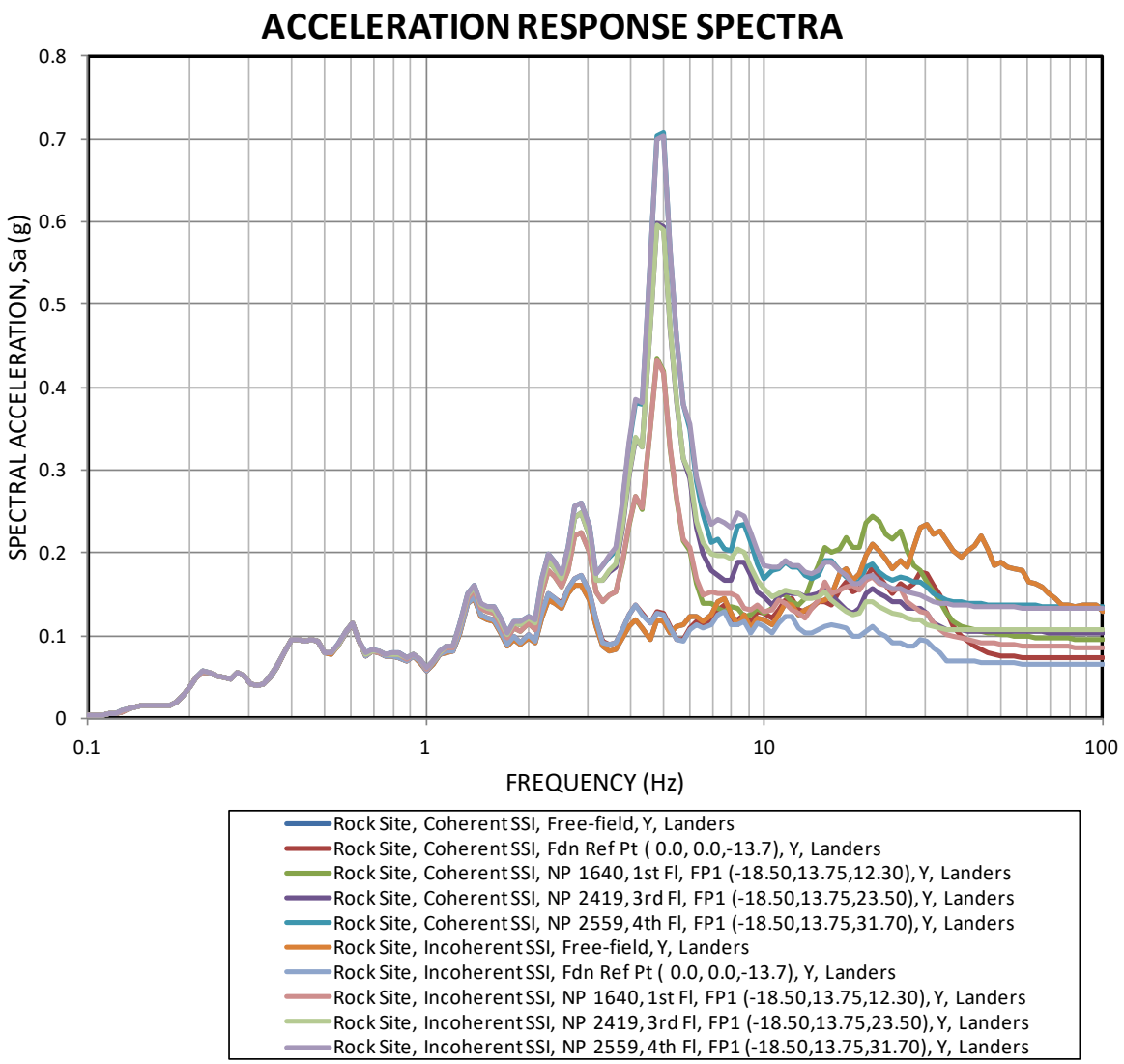

Fig. I–31. KKNPP Unit 7, reactor building, node points: 2559, 4th floor; 2419, 3rd floor; 1640, 1st floor; foundation ref. point; Landers earthquake; Y(E-W)-direction; coherent SSI, incoherent SSI.

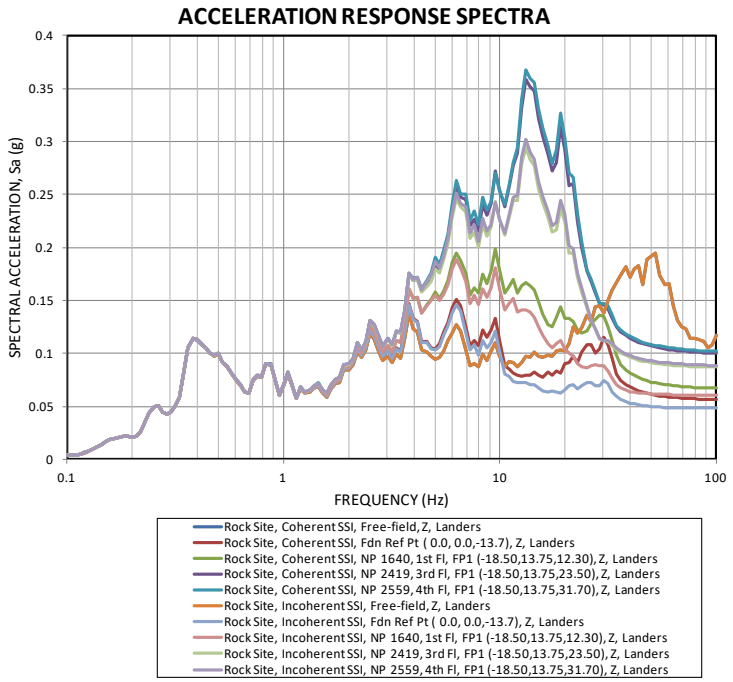

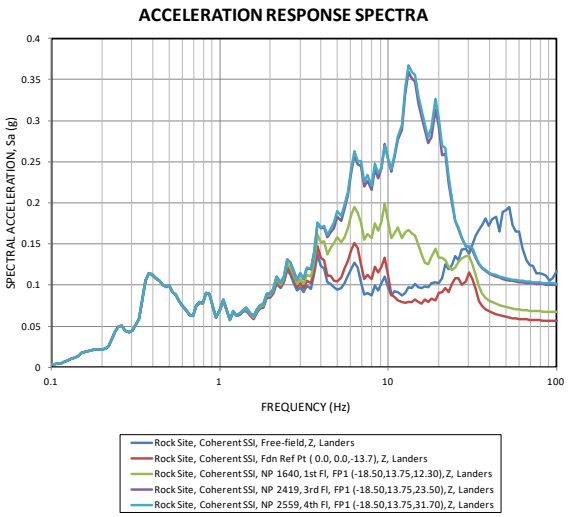

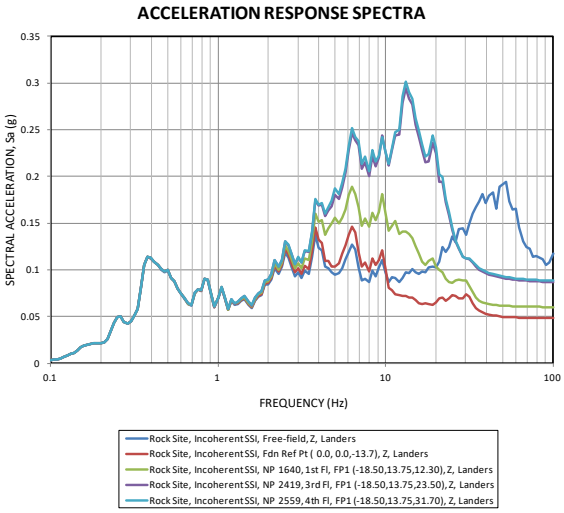

Fig. I–32.a) KKNPP Unit 7, reactor building, node points: 2559, 4th floor; 2419, 3rd floor; 1640, 1st floor; foundation ref. point; Landers earthquake; Z(Vert)-direction; coherent SSI, incoherent SSI (above), b) KKNPP Unit 7, reactor building, node points: 2559, 4th floor; 2419, 3rd floor; 1640, 1st floor; foundation ref. point; Landers earthquake; Z(Vert)-direction; coherent SSI (left below), c) KKNPP Unit 7, reactor building, node points: 2559, 4th floor; 2419, 3rd floor; 1640, 1st floor; foundation ref. point; Landers earthquake; rock; Z(Vert)-direction; incoherent SSI (right below).

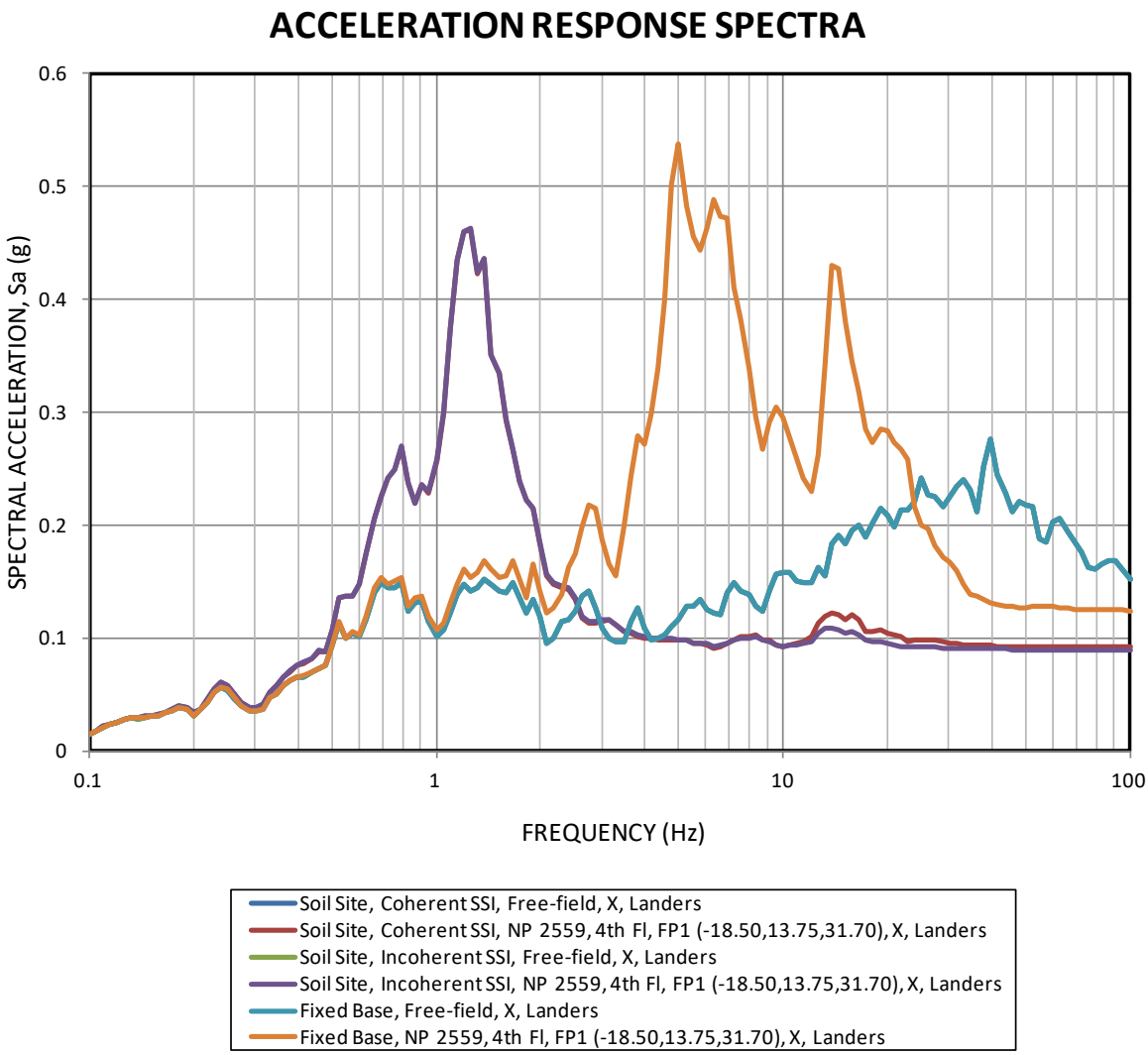

Fig. I–33. KKNPP Unit 7, reactor building, node point 2559, 4th floor; Landers earthquake; rock; X (N - S) - direction; fixed-base, coherent SSI, incoherent SSI.

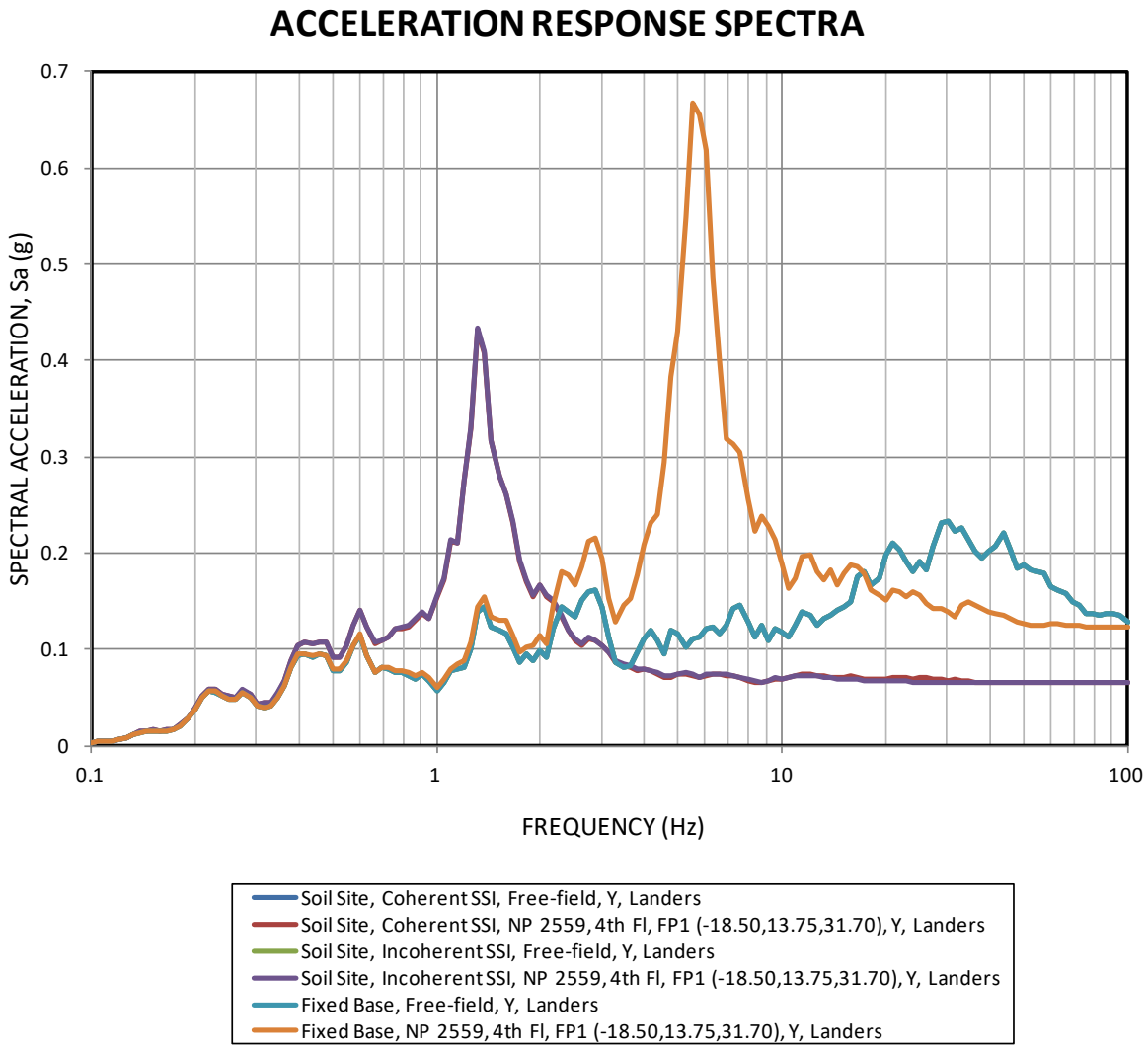

Fig. I–34. KKNPP Unit 7, reactor building, node point 2559, 4th floor; Landers earthquake; rock; Y (E-W) - direction; fixed-base, coherent SSI, incoherent SSI.

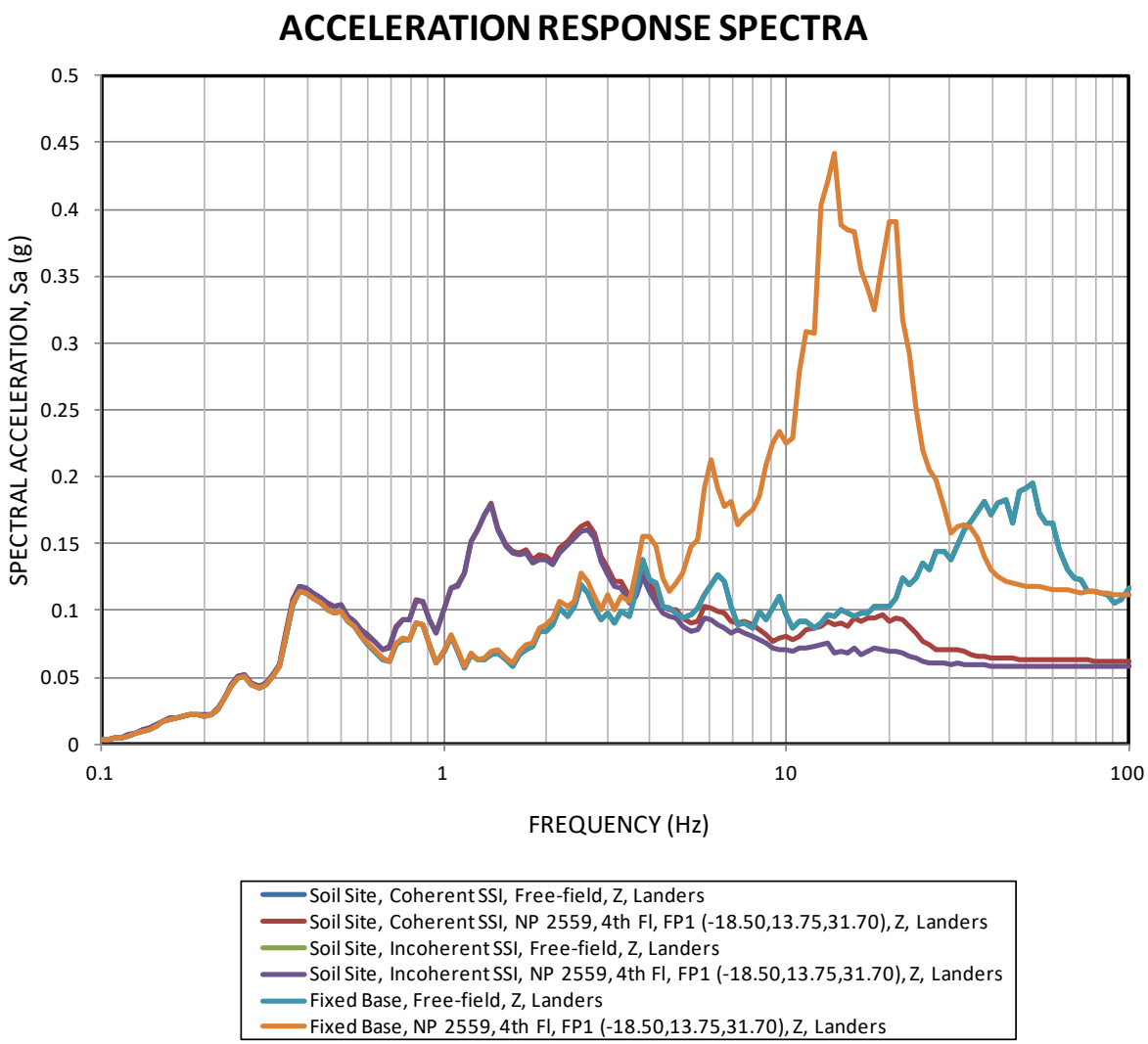

Fig. I–35. KKNPP Unit 7, reactor building, node point 2559, 4th floor; Landers earthquake; rock; Z(Vert) direction; fixed-base, coherent SSI, incoherent SSI.

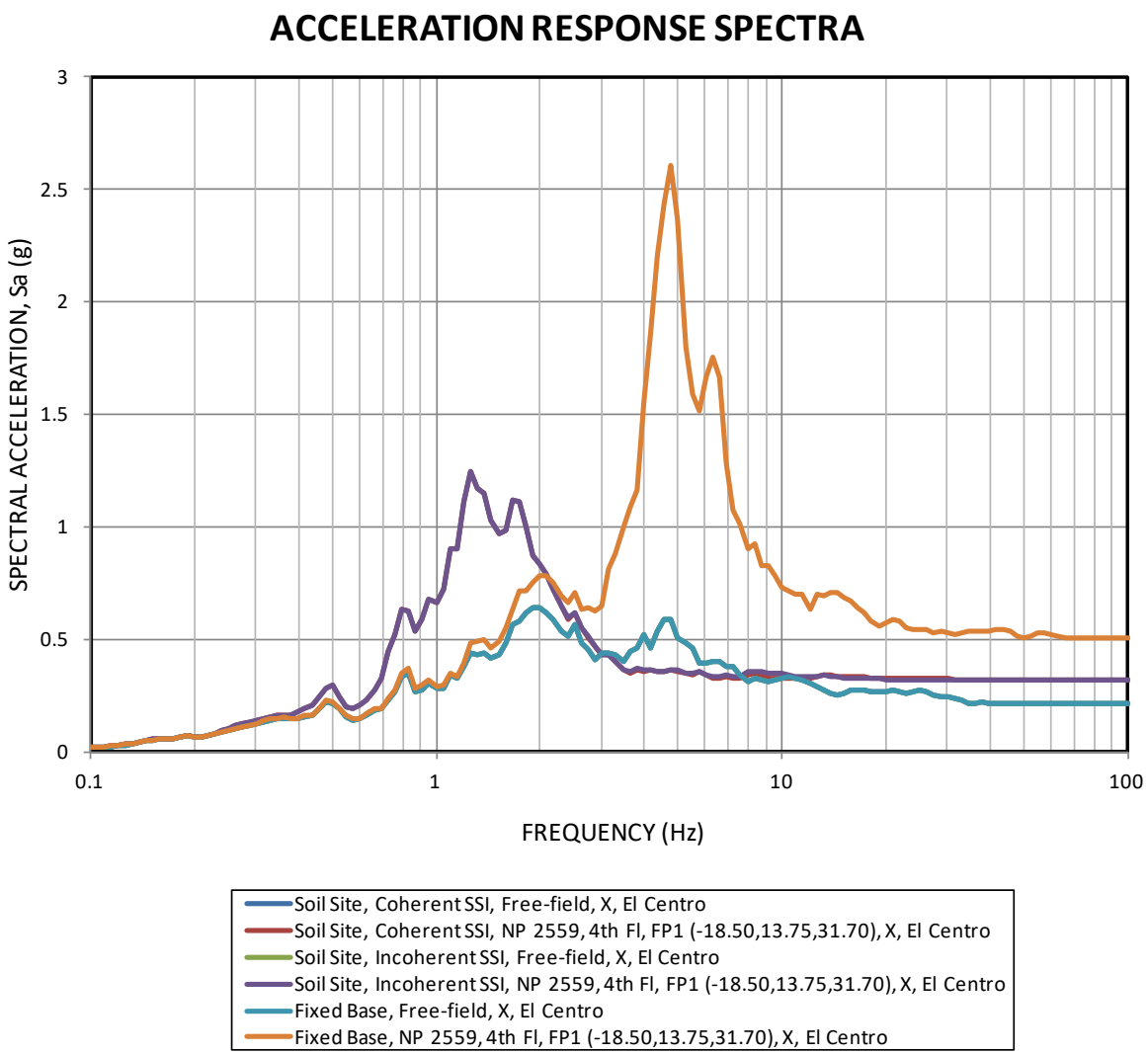

Fig. I–36. KKNPP Unit 7, reactor building, node point 2559, 4th floor; El Centro earthquake; soil; X(N-S)-direction; fixed-base, coherent SSI, incoherent SSI.

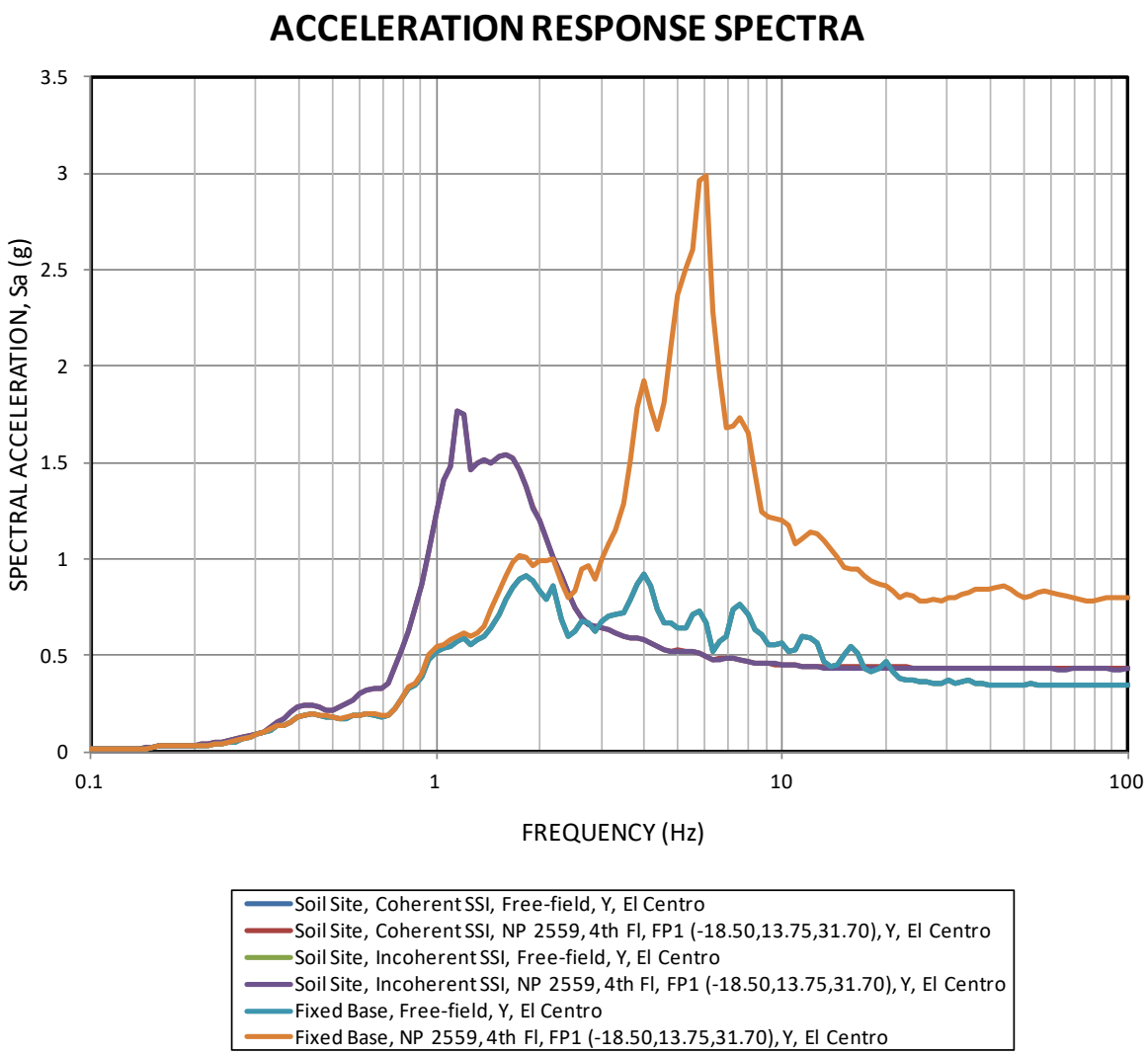

Fig. I–37. KKNPP Unit 7, reactor building, node point 2559, 4th floor; El Centro earthquake; soil; Y(E-W)-direction; fixed-base, coherent SSI, incoherent SSI.

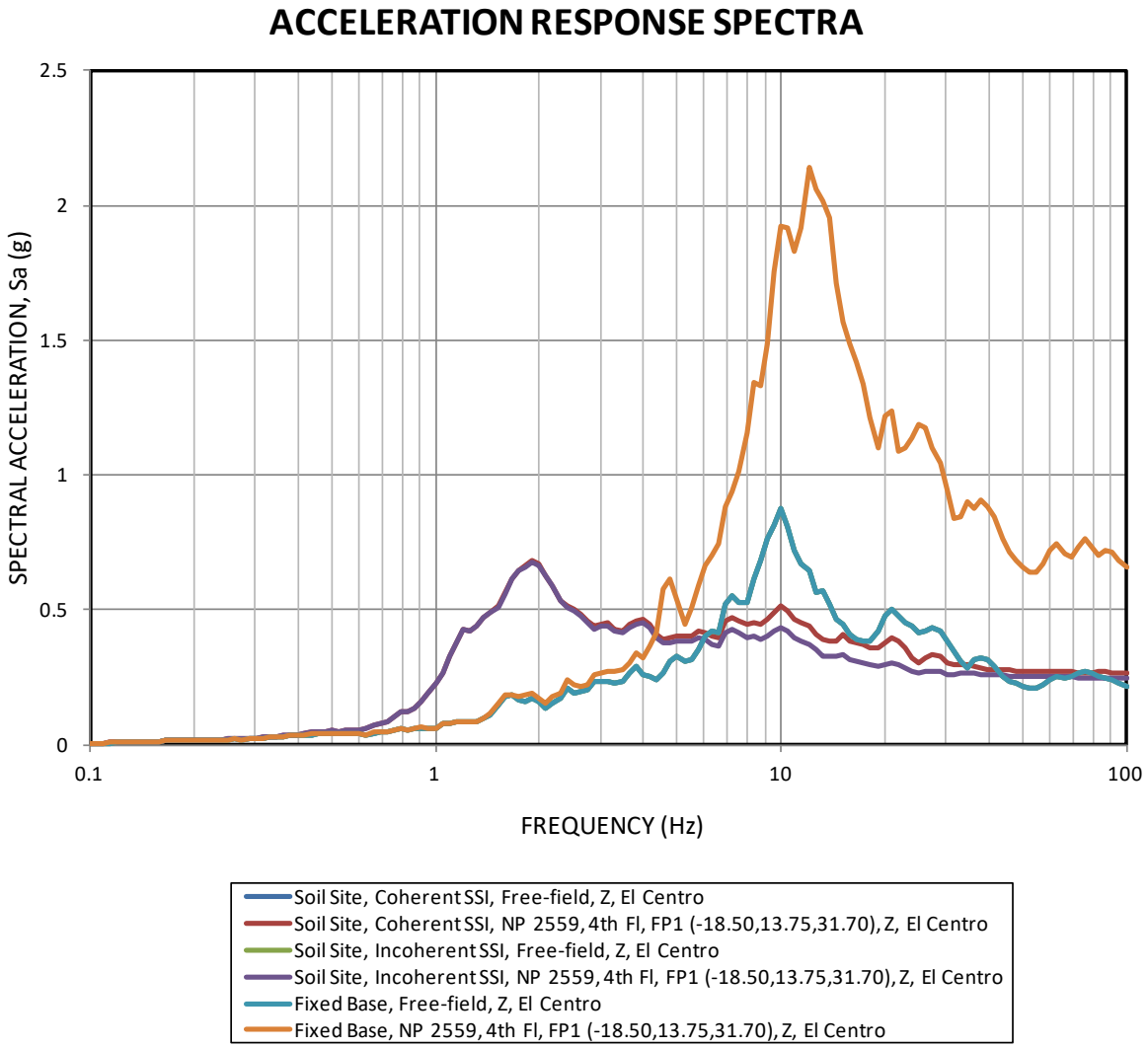

Fig. I–38. KKNPP Unit 7, reactor building, node point 2559, 4th floor; El Centro earthquake; soil; Z(Vert)-direction; fixed-base, coherent SSI, incoherent SSI.

REFERENCES TO ANNEX I

[I–1] US NUCLEAR REGULATORY COMMISSION Regulatory Guide 1.60, Design Response Spectra for Seismic Design of Nuclear Power Plants, Rev. 2 (2014).

[I–2] ZERVA, A., Spatial Variation of Seismic Ground Motions: Modelling and Engineering Applications, CRC Press, New York, NY (2009).

[I–3] ABRAHAMSON, N. A., Program on Technology Innovation: Spatial Coherency Models for Soil Structure Interaction, EPRI, Palo Alto, CA and the U.S. Department of Energy, Germantown, MD, 1014101 (2006).

[I–4] ABRAHAMSON, N., Hard Rock Coherency Functions Based on the Pinyon Flat Data (2007).

[1–5] US NUCLEAR REGULATORY COMMISSION, NUREG-0800, Standard review plan, seismic system analysis, 3.7.2 Rev. 3 (2007).

[I–6] INTERNATIONAL ATOMIC ENERGY AGENCY, Review of Seismic Evaluation Methodologies for Nuclear Power Plants Based on a Benchmark Exercise, IAEA-TECDOC-1722, IAEA, Vienna (2014).

[I–7] JOHNSON, J.J., GODOY, A.R., GURPINAR, A., KENNEALLY, R.M., Impacts of the Niigataken Chūetsu-Oki (NCO) Earthquake on the Kashiwazaki-Kariwa Nuclear Power Plant, Post-Earthquake Response, and Lessons Learned: U.S. Perspective, U.S. NRC (2018).

[1–8] SHORT, S.A., HARDY, G.S., MERZ, K.L., and JOHNSON, J.J., Program on Technology Innovation: Validation of CLASSI and SASSI Codes to Treat Seismic Wave Incoherence in Soil-Structure Interaction (SSI) Analysis of Nuclear Power Plant Structures, EPRI, Palo Alto, CA and the U.S. Department of Energy, Germantown, MD, 1015111 (2007).

[1–9] JOHNSON, J.J., SHORT, S.A., HARDY, G.S., Modelling Seismic Incoherence Effects on NPP Structures: Unifying CLASSI and SASSI Approaches, Paper K05-5, 19th Structural Mechanics in Reactor Technology (SMiRT19), Toronto, Canada (2007).

Annex II

SITE RESPONSE ANALYSIS

II–1. DESCRIPTION OF THE PROBLEM AND SOLUTION

The soil profile consists of 30.0m of sandy gravel overlying a 20m thick layer of stiff over consolidated clay on top of a rock layer considered as a homogeneous half-space (Figure II–1). The water table is located at a depth of 10.0m below the ground surface. The incident motion is imposed at an outcrop of the half-space in the form of an acceleration time history; only the horizontal component and of the input motion is taken into account; however, some runs will be carried out with both a horizontal and a vertical incident motion. Under the assumption of vertically propagating shear waves, the numerical model is a 1-D geometric model; however, to reflect the coupling between the shear strain and volumetric strains each node of the model possesses two (1-phase medium or 2-phase undrained layer) or four (2-phase medium pervious layer) degrees of freedom corresponding to the vertical and horizontal displacements (respectively vertical and horizontal translations of solid skeleton and vertical and horizontal velocities of the fluid).

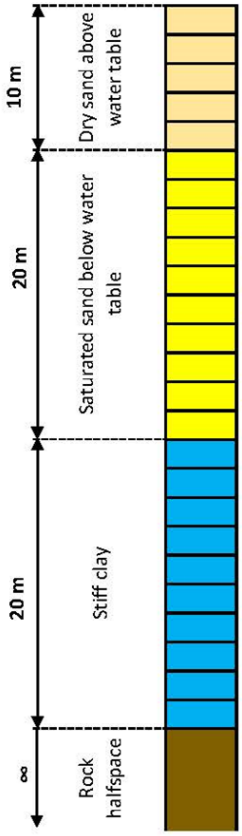

Two situations have to be considered depending on the depth of the soil element:

– above the water table a one-phase medium (solid phase) is considered;

– below the water table a two-phase medium (solid phase and fluid phase) is considered.

The dynamic equilibrium equations relevant to each situation are recalled below. For more details on the derivation of these equations, one can refer to Refs [II–1, II–2].

Soil above the water table

The wave equation to be solved is:

$$\nabla.\sigma + \rho g = \rho a \qquad \text{(II-1)}$$

where

$\underset{\sim}{\sigma}$ solid stress tensor

ρ soil mass density

$\underset{\sim}{a}$ solid acceleration

$\underset{\sim}{g}$ body forces (gravity)

Soil below the water table

The following notations are used

ρ_S solid mass density

ρ_f fluid mass density

φ soil porosity

$\rho = (1-\varphi)\rho_S + \varphi\rho_f = \rho^S + \rho^f$ soil mass density

$\rho_b = (\rho - \rho_f) = (1-\varphi)(\rho_S - \rho_f)$ soil buoyant mass density

K_f fluid bulk modulus

$\underset{\sim}{\sigma}^S$ solid effective stress tensor

p_w excess (with respect to hydrostatic) pore water pressure

$\underset{\sim}{a}^S, \underset{\sim}{v}^S$ solid acceleration and velocity

$\underset{\sim}{a}^f, \underset{\sim}{v}^f$ fluid acceleration and velocity

$\underset{\sim}{k}$ permeability tensor

It is further assumed that the grains are incompressible with respect to the skeleton and that the strains are small. The equations to be solved are:

- Solid phase:

$$\nabla.\underset{\sim}{\sigma}'^S - (1-\varphi)\nabla p_w - \rho_w g \varphi^2 \underset{\sim}{k}^{-1}.(\underset{\sim}{v}^S - \underset{\sim}{v}^f) + \rho_b \underset{\sim}{g} = \rho^S \underset{\sim}{a}^S \qquad \text{(II-2)}$$

- Fluid phase:

$$-\varphi\nabla p_w + \rho_w g\varphi^2 \underset{\sim}{k}^{-1}.(\underset{\sim}{v}^S - \underset{\sim}{v}^f) = \rho^f \underset{\sim}{a}^f \qquad \text{(II-3)}$$

- Fluid balance of mass:

$$\frac{dp_w}{dt} = -\frac{K_f}{\varphi}\left[\nabla.[(1-\varphi)\underset{\sim}{v}^S] + \nabla.[\varphi \underset{\sim}{v}^f]\right] \qquad \text{(II-4)}$$

Equations (II–2) and (II–4) are valid regardless of the assumption retained regarding the possible diffusion of excess pore pressures: in undrained conditions $\underset{\sim}{v}^S = \underset{\sim}{v}^f$ while under partially drained conditions $\underset{\sim}{v}^S \neq \underset{\sim}{v}^f$ and the rate of dissipation is controlled by the permeability.

For undrained conditions Equations (II–2) and (II–3) are reduced to:

$$\nabla.\underset{\sim}{\sigma}'^S - \nabla p_w + \rho_b \underset{\sim}{g} = \rho \underset{\sim}{a}^S \qquad \text{(II-5)}$$

And the excess pore water pressure is computed from equation (II–4):

$$\frac{dp_w}{dt} = -\frac{K_f}{\varphi}\nabla.\underset{\sim}{v}^S \qquad \text{(II-6)}$$

II–2. CONSTITUTIVE MODEL FOR THE SOIL LAYERS

The constitutive model selected for the calculations is the multi-yield plasticity model [II–3–II–5] implemented in the computer program DYNAFLOW [II–6]. The constitutive parameters of the multi-yield model are expressed in terms of traditional soil properties. A short description of the model and of its parameters is presented hereafter. The constitutive model is written in terms of effective stresses.

II–2.1. Basic Relations

The multi-yield constitutive soil model is a kinematic hardening model based on a relatively simple plasticity theory [II–4] and is applicable to both cohesive and cohesionless soils. The concept of a "field of work-hardening moduli" [II–3, II–7 and II–8] is used by defining a collection $f_0, f_1, \ldots, f_n$ of nested yield surfaces in the stress space. Von Mises type surfaces are employed for cohesive materials (clay), and Mohr-Coulomb type surfaces are employed for frictional materials (sandy gravels).

The yield surfaces define regions of constant shear moduli in the stress space, and in this manner the model discretizes the smooth elastic-plastic stress-strain curve into n linear segments. The outermost surface f_n corresponds to the maximum shear strength and plays the role of a failure surface.

II–2.1.1. Cohesionless materials

For cohesionless materials, the selected yield surfaces correspond to a pressure sensitive material and are of the Mohr-Coulomb's type:

$$f = \left[\frac{3}{2}\mathrm{tr}(\underset{\sim}{s} - \bar{p}\underset{\sim}{\alpha})^2\right]^{\frac{1}{2}} + k\bar{p}g(\theta) \qquad \text{(II-7)}$$

where:

$\bar{p} = p' - a,\ a = c/\tan\phi$ is the attraction.
$\underset{\sim}{s} = \underset{\sim}{\sigma}' - p'\underset{\sim}{\delta}$ is the deviatoric stress tensor
$p' = \frac{1}{3}\mathrm{tr}\underset{\sim}{\sigma}'$ is the mean effective stress
$\underset{\sim}{\delta}$ is the Kronecker tensor
$\underset{\sim}{\alpha}$ is a tensor defining the position of the yield surface
k is the size of the yield surface

The function $g(\theta)$ determines the shape of the cross-section in the deviatoric plane and is defined as follows :

$$g(\theta) = \frac{2M_k}{(1+M_k)-(1-M_k)\sin 3\theta} \qquad \text{(II-8)}$$

where:

$$\sin 3\theta = -\sqrt{6}\,\bar{J}_3/\bar{J}_2^{3/2}$$

$$\bar{J}_2 = \mathrm{tr}\underset{\sim}{\bar{s}}^2 \quad , \quad \bar{J}_3 = \mathrm{tr}\underset{\sim}{\bar{s}}^3 \quad , \quad \underset{\sim}{\bar{s}} = \underset{\sim}{s} - \bar{p}\underset{\sim}{\alpha}$$

M_k is a material parameter that is equal, for a round-cornered Mohr-Coulomb cone, to:

$$M_k = \frac{3-\sin\phi}{3+\sin\phi} \qquad \text{(II-9)}$$

The plastic flow rule in this case is defined as: $\dot{\underset{\sim}{\varepsilon}}^p = \langle\dot{\lambda}\rangle\underset{\sim}{P}$, where $\dot{\underset{\sim}{\varepsilon}}^p$is the plastic strain rate, $\underset{\sim}{P}$is the plastic potential: $\underset{\sim}{P} = \underset{\sim}{P}' + P''\underset{\sim}{\delta}$, $\dot{\lambda}$ is the plastic load factor. To account for experimental evidence from tests on frictional materials, a non-associative flow rule is used for the dilatational component of the plastic potential, P'', whereas the deviatoric component is modelled by an associative flow rule:

$$3P'' = \frac{(\eta/\bar{\eta})^2-1}{(\eta/\bar{\eta})^2+1}X_{PP} \qquad \text{(II-10)}$$

where $\bar{\eta}, X_{pp}$are material parameters. This equation expresses the dependence of soil dilatational behaviour on the mobilized stress ratio $\eta = \frac{\left(\frac{3}{2}\underset{\sim}{s}:\underset{\sim}{s}\right)^{\frac{1}{2}}}{p'}$.

The material hysteretic behaviour and shear stress-induced anisotropic effects are simulated by a kinematic rule. Upon contact, the yield surfaces are translated in the stress space by a stress point, and the direction of translation is selected such that the yield surfaces do not overleap but remain tangent to each other at the stress point.

For the case of the pressure sensitive materials, a purely kinematic rule is adopted. The dependence of the moduli on the mean effective stress is assumed to be of the following form:

$$x = x_1\left(\frac{p'}{p'_1}\right)^n \qquad \text{(II-11)}$$

where $x = G$ (shear modulus), B (bulk modulus), H (plastic modulus) and n is the power exponent, a material constant.

The constitutive equations $\dot{\underset{\sim}{\sigma}}' = \underset{\sim}{E}:(\dot{\underset{\sim}{\varepsilon}} - \dot{\underset{\sim}{\varepsilon}}^p)$, where $\dot{\underset{\sim}{\varepsilon}}$is the strain rate tensor and $\underset{\sim}{E}$ the fourth order isotropic tensor of elasticity, are integrated numerically using a stress relaxation procedure. The return-mapping algorithm, proposed in [9], has been modified for the multi-yield plasticity case by Prevost [II–10, II–11].

II–2.1.2. Cohesive materials

For the cohesive material (stiff clay) the selected yield surfaces correspond to a pressure non-sensitive material and are of the Von Mises type:

$$f = \left[\frac{3}{2}\mathrm{tr}(\underset{\sim}{s} - \underset{\sim}{\alpha})^2\right]^{\frac{1}{2}} - k \qquad \text{(II-12)}$$

with the same definition of the parameters as for the Mohr-Coulomb yield surfaces.

II–2.2. Constitutive Model Parameters

The constitutive parameters of the multi-yield constitutive soil model, are summarized in Table II–1, and described in the foregoing:

(1) *State parameters*

Mass density of the solid phase ρ_s and, for the case of porous saturated media, porosity φ and permeability k.

(2) *Low strain elastic parameters*

Low strain moduli G_1 and B_1 for the case of the pressure sensitive materials, which are related through the value of Poisson's coefficient ν, as follows:

$$B_1 = \frac{2G_1(1+\nu)}{3(1-2\nu)} \qquad \text{(II-13)}$$

The dependence of the moduli on the mean effective stress p', is assumed to be given by equation (II–11) and is accounted for, by introducing two additional parameters; the power exponent n and the reference mean effective stress p'_1 (which is arbitrary).

For pressure non sensitive materials, the parameters are simply G and B the shear and bulk moduli. Equation (II–13) still applies to G and B.

(3) *Yield and failure parameters*

These parameters describe the position α_i, size M_i and plastic modulus H'_i, corresponding to each yield surface f_i, $i = 0, 1, \ldots m$. For a given number of m+1 yield surfaces, all these parameters can be evaluated based on experimental stress-strain curves obtained from triaxial or simple shear soil tests [II–10, II–12].

For the case of pressure sensitive materials, a modified hyperbolic expression proposed in Ref. [II-13] is used to simulate soil stress-strain relations. Four parameters, namely the friction angle at failure ϕ, and the shear stress-strain curve coefficients α , x_u, x_l, apart from the low strain shear modulus G_1, are needed to describe the sizes M_i and plastic moduli H'_i of yield surfaces. Finally, the coefficient of lateral stress K_0 is necessary to evaluate the initial positions α_i of the yield surfaces.

For pressure non sensitive materials the same type of relationship is used; the friction angle at failure is replaced by the maximum shear stress (or cohesion).

TABLE II–1. LIST OF PARAMETERS FOR THE MULTI-YIELD CONSTITUTIVE MODEL

Constitutive Parameter	**Symbol**	**Type**
Solid mass density	ρ_s	State Parameters
Fluid mass density	ρ_f	
Porosity	φ	
Permeability	k	
Low strain elastic moduli	G_1, B_1	Low Strain Elastic Parameters
Reference mean effective stress	p'_1	
Power exponent	n	
Fluid bulk modulus	K_f	
Friction angle at failure	ϕ	Yield and Failure Parameters
Cohesion	c	
At rest earth pressure coefficient	K_0	
Shape of shear stress-strain curve	α , x_l , x_u	Dilation Parameters
Dilation angle	$\bar{\phi}$	
Dilation parameter (cyclic)	X_{pp}	

(4) *Dilation parameters*

They are used to evaluate the volumetric part of the plastic potential $3P''$. These parameters only apply to pressure sensitive materials and are analysed in detail in the foregoing:

- dilation (or phase transformation) angle $\bar{\phi}$, related to the parameter $\bar{\eta}$ by the following expression:

$$\bar{\eta}_{\substack{C \\ E}} = \pm \frac{6 \sin \bar{\phi}}{3 \pm \sin \bar{\phi}} \tag{II-14}$$

where in the triaxial stress state, C stands for triaxial compression and E for triaxial extension, and for the general three-dimensional stress state, $\bar{\eta} = \bar{\eta}_C$ if $\mathrm{tr}\,\underset{\sim}{s}^3 < 0$ and $\bar{\eta} = \bar{\eta}_E$ if $\mathrm{tr}\,\underset{\sim}{s}^3 > 0$, [4];

- dilation parameter X_{PP}, is the scale parameter for the plastic dilation that depends basically on relative density and sand type (fabric, grain size).

(5) *Shear stress-strain data generation*

For the shear stress-strain data curve generation, given the maximum shear modulus G_1 and the maximum shear stress $\tau_{\max}$, two options are available in the computer program DYNAFLOW, from which the following has been chosen:

For $y = \tau/\tau_{\max}$ and $x = \gamma/\gamma_r$, $\gamma_r = \tau_{\max}/G_1$, then:

$$y = e^{-\alpha x} f(x, x_l) + \left(1 - e^{-\alpha x}\right) f(x, x_u) \tag{II-15}$$

where:

$$f(x, x_i) = \frac{\left[\left(2\frac{x}{x_i + 1}\right)^{x_i} - 1\right]}{\left[\left(2\frac{x}{x_i + 1}\right)^{x_i} + 1\right]}$$

where α, x_l and x_u are material parameters [13].

II–2.3. Saturated Fluid

In order to simulate the behaviour of the saturated soil column during an earthquake, the solid effective stress constitutive model is coupled with a fluid constitutive model. When the permeability of the various strata is rather small ($<10^{-4}$ m/s) undrained behaviour can be assumed and a simplified u–p formulation is used in which the independent variables are the (horizontal and vertical) solid displacements, u-w. The pore water pressure p_w is calculated from Eq. (II–6).

The fluid is characterized by its bulk modulus K_f and its mass density ρ_f; it is activated only after initialization of the initial stresses which is carried out under drained conditions.

II–3. CONSTITUTIVE MODEL FOR THE ROCK AND THE HALF-SPACE

The half-space situated below the soil column is modelled as a purely elastic medium without any damping. Its properties enter the definition of the transmitting boundary element used in the finite element to represent the radiation of waves to infinity.

The parameters for this material are the *P* and *S*-wave velocities and the mass density.

II–4. COMPUTER CODE AND NUMERICAL INTEGRATION

The computer code used for the analysis is DYNAFLOW.

The system of ordinary differential equations is solved by applying a step by step integration procedure resulting in a system of non-linear algebraic equations. DYNAFLOW uses one-step methods to carry out the time integration with Newmark update formulae. The iterative strategy is implemented by means of a predictor-multi corrector scheme applied at each time step. The non-linear equations are solved using a quasi-Newton algorithm with line search at each time step [II–14].

The analysis proceeds as follows:

- Initialization of the stresses under the gravity field. this step is performed under drained conditions, i. e. the fluid bulk modulus is set to 0.
- Application of the horizontal earthquake motion, at an outcrop of the half-space; this is achieved with a special transmitting element which exactly represents the stress conditions at the soil column–half-space interface. This step is carried out under undrained conditions. The fluid bulk modulus is thus activated for the soil below the water table. The maximum time step used for the computations is equal to 0.005s but may be further reduced to achieve convergence within a time step.

Within the context of vertical propagation of shear waves, the exact transmitting element placed at the bottom of the soil column is defined by:

- horizontal direction $\rho_R V_{SR}$ (II–16)

where ρ_R, and V_{SR} are the rock mass density, and the rock shear wave velocity. The boundary condition is imposed as a shear stress equal to:

- horizontal direction $\tau = \rho_R V_{SR} \dot{u}_R(t)$ (II–17)

where $\dot{u}_R(t)$ is the horizontal velocity of the input motion at an outcrop of the half-space.

In the vertical direction a transmitting boundary is imposed at the rock interface to prevent reflection of downwards propagating dilatational waves generated by shear-volumetric coupling in the constitutive model. This transmitting boundary is a dashpot with coefficient:

$$C = \rho_R V_{PR} \quad \text{(II–18)}$$

where V_{PR} is the rock dilatational wave velocity.

Since the transmitting boundary element in the vertical direction does not ensure equilibrium under gravity loads (the dashpot is inactive for permanent loads), the initialization phase actually takes place in two steps: first, the vertical node at the bottom of the finite element model is fixed in the vertical direction and the gravity loads applied to the model. The vertical reaction force at the bottom node is then retrieved and applied as an external force in the model. The second step consists of redoing the initialization phase with the transmitting boundary and the previously computed reaction force. In addition, to prevent rigid body motions due to round-off errors in the computation of the reaction force, a very weak spring element is added at the bottom boundary in the vertical direction. This weak spring does not affect the dynamic response.

When a vertical motion is imposed at the lower boundary a shear stress equal to:

– vertical direction $\sigma = \rho_R V_{SR} \dot{v}_R(t)$ (II–19)

where $\dot{v}_R(t)$ is the vertical velocity of the input motion at an outcrop of the half-space.

II–5. SOIL PROFILE AND CONSTITUTIVE PARAMETERS

This section summarizes the information and its transcription into the parameters of the constitutive model used for the analyses.

For the site response analyses the soil profile identified consists of 30.0m of sandy gravel, 20m of stiff clay, overlying a rock layer considered as a homogeneous half-space. The water table is located at a depth of 10.0m below the ground surface.

The bulk of information consists of the (P and S) wave velocity profiles, non-linear modulus degradation curves (G / G_{max} vs γ).

II–5.1. State Parameters

The values of the parameters are given in Table II–2.

II–5.2. Elastic Parameters

The shear modulus G and bulk modulus B need, for pressure sensitive materials, to be cast in the format of equation (II–11) defining the dependence of the moduli on the confining stress. Based on published results in the technical literature for cohesionless materials, the power exponent n entering equation (II–11) is taken equal to 0.5. The reference pressure p_1, which is totally arbitrary, is set to 0.10 MPa. The shear modulus and bulk modulus are computed as described and converted in values G_1 and B_1 at the reference pressure as described in below.

II–5.2.1. Soil above the water table and rock

The shear modulus is related to the shear wave velocity through:

$$G = \rho V_S^2 \quad \text{(II–20)}$$

where ρ is the soil mass density defined in Table II–2.

The bulk modulus is related to the dilatational wave velocity and shear modulus through:

$$B = \rho V_P^2 - \frac{4}{3} G \qquad \text{(II–21)}$$

TABLE II–2. CONSTITUTIVE MODEL- STATE PARAMETERS

	Sandy gravel above water table	Sandy gravel below water table	Stiff clay	Rock
Soil mass density ρ (t/m^3)	1.95	2.1	2.0	2.4
Solid mass density ρ_s (t/m^3)	N/A	2.7	N/A	N/A
Fluid mass density ρ_f (t/m^3)	N/A	1.00	N/A	N/A
Porosity φ	N/A	0.35	N/A	N/A
Permeability (m/s)	N/A	Variable	N/A	N/A

Notes: for the porous layer the total soil mass density is computed as
$\rho = (1-\varphi)\,\rho_s + \varphi\,\rho_w = 0.65 \times 2.7 + 0.35 \times 1.0 = 2.1$ t/m^3
N/A: this parameter is not relevant for the constitutive modelling of the material.

For the rock half-space, these properties complete the definition of the constitutive model (linear elastic model).

II–5.2.2. Soil below the water table

The shear modulus is related to the shear wave velocity through:

$$G = (1 - \varphi)\rho_S V_S^2 \qquad \text{(II–22)}$$

where ρ_S is the solid mass density and φ the soil porosity, both defined in Table II–2. The bulk modulus is related to the dilatational wave velocity, soil shear modulus, fluid bulk modulus and soil porosity through:

$$B = \rho V_P^2 - \frac{4}{3} G - \frac{K_f}{\varphi} \qquad \text{(II–23)}$$

where ρ is the soil mass density defined in Table II–2.

II–5.2.3. Moduli at the reference pressure

Once the shear and bulk soil moduli are computed as described previously, they are converted to values at the reference stress p_1 (0.10 MPa) in accordance with:

$$G_1 = G\sqrt{\frac{p_1}{p_0}} \quad , \quad B_1 = B\sqrt{\frac{p_1}{p_0}} \qquad \text{(II–24)}$$

p_0 is the mean effective stress at the depth where G and B are computed. It is given by:

$$p_0 = \left(\frac{1+2K_0}{3}\right)\sigma_v' \qquad \text{(II–25)}$$

K_0 is the earth pressure coefficient at rest and σ'_v the vertical effective stress.

$$K_0 = \frac{\nu}{1-\nu} = \frac{3B-2G}{3B+4G} \qquad \text{(II–26)}$$

Values of the elastic parameters and details of all the intermediate calculations (equations (II–22–II–25)) are given in Table II–3 for each layer of the finite element model.

II–5.3. Strength Parameters

For sandy gravel the drained friction angle is equal to 42°. An associated drained cohesion has been assumed. The non-zero value of the cohesion may look unusual for a cohesionless material. It can nevertheless be justified because it does not reflect a true cohesion but an apparent one due to the curved shape of the Mohr-Coulomb failure envelope; this curved shape and apparent cohesion are then due to dilatancy of the very dense material.

For the clay only the cohesion is needed. It is taken equal to 0.30MPa.

The parameters retained for the analysis are summarized in Table II–4.

II–5.4. Yield parameters

The yield parameters are estimated to fit as closely as possible the modulus degradation curves provided in the technical literature for equivalent linear analyses.

Numerical simulation of cyclic simple shear tests is carried out under representative confining pressures and the model parameters defined in equation (II–15) are determined by trial and error to approximate the backbone curves at the third cycle of loading. Those backbone curves $\tau = g(\gamma)$ are computed according to:

$$\frac{G}{G_{max}} = f(\gamma) \Rightarrow \tau = G\gamma = G_{max}\,\gamma\, f\,(\gamma) = g\,(\gamma) \qquad \text{(II–27)}$$

The value of G_{max} relevant for each numerical test is taken equal to the field value at the corresponding depth (see Table II.3):

- z = 5m σ'_m = 80 kPa G_{max} = 160 MPa
- z = 20m σ'_m = 245 kPa G_{max} = 275 MPa
- z = 40m σ'_m = 500 kPa G_{max} = 240 MPa

Results of the calibration are shown in Figure II–2 for sandy gravel and in Figure II–3 for clay.

The parameters provided in Table II–4 are deemed to be applicable for soil layers above 10m and for soil layers below 10m. Therefore, since the calibrations of those parameters

are carried out at the reference pressure of the representative samples (0.10MPa), the reference pressure used in Table II–4 for other layers is kept equal to this value; this procedure ensures that the stress dependency of the G/G_{max} curves is correctly reflected.

TABLE II–3. CONSTITUTIVE MODEL – ELASTIC PARAMETERS

Layer N°	Number of elements	Depth range	Mid depth	Mass density	Porosity	Shear wave velocity	Dilatational wave velocity	Shear modulus	Poisson's ratio	Bulk modulus	Vertical effective stress	Mean effective stress	Reference shear modulus	Reference bulk modulus	Fluid bulk modulus	Saturated dilatational wave velocity	Power exponent *n*
		(m)	(m)	(t/m^3)	-	(m/s)	(m/s)	(MPa)	-	(MPa)	(kPa)	(kPa)	(MPa)	(MPa)	(MPa)	(MPa)	-
1	1	0.0 - 0.5	0.250	1.95	0.35	134	345	35	0.41	185	4.875	4	176	939	-	-	0.50
2	1	0.5 - 1.0	0.750	1.95	0.35	176	454	60	0.41	321	14.625	12	176	939	-	-	0.50
3	1	1.0 - 1.5	1.250	1.95	0.35	200	515	78	0.41	415	24.375	20	176	939	-	-	0.50
4	1	1.5 - 2.0	1.750	1.95	0.35	217	561	92	0.41	490	34.125	27	176	939	-	-	0.50
5	1	2.0 - 2.5	2.250	1.95	0.35	231	597	104	0.41	556	43.875	35	176	939	-	-	0.50
6	1	2.5 - 3.0	2.750	1.95	0.35	243	628	115	0.41	615	53.625	43	176	939	-	-	0.50
7	1	3.0 - 3.5	3.250	1.95	0.35	254	655	125	0.41	668	63.375	51	176	939	-	-	0.50
8	1	3.5 - 4.0	3.750	1.95	0.35	263	678	135	0.41	718	73.125	59	176	939	-	-	0.50
9	1	4.0 - 4.5	4.250	1.95	0.35	271	700	143	0.41	764	82.875	66	176	939	-	-	0.50
10	1	4.5 - 5.0	4.750	1.95	0.35	279	720	152	0.41	808	92.625	74	176	939	-	-	0.50
11	1	5.0 - 5.5	5.250	1.95	0.35	286	738	159	0.41	849	102.375	82	176	939	-	-	0.50
12	1	5.5 - 6.0	5.750	1.95	0.35	292	755	167	0.41	889	112.125	90	176	939	-	-	0.50
13	1	6.0 - 6.5	6.250	1.95	0.35	299	771	174	0.41	927	121.875	98	176	939	-	-	0.50
14	1	6.5 - 7.0	6.750	1.95	0.35	304	786	181	0.41	963	131.625	105	176	939	-	-	0.50
15	1	7.0 - 7.5	7.250	1.95	0.35	310	800	187	0.41	998	141.375	113	176	939	-	-	0.50
16	1	7.5 - 8.0	7.750	1.95	0.35	315	813	194	0.41	1032	151.125	121	176	939	-	-	0.50
17	1	8.0 - 8.5	8.250	1.95	0.35	320	826	200	0.41	1065	160.875	129	176	939	-	-	0.50
18	1	8.5 - 9.0	8.750	1.95	0.35	325	838	206	0.41	1097	170.625	137	176	939	-	-	0.50
19	1	9.0 - 9.5	9.250	1.95	0.35	329	850	211	0.41	1128	180.375	144	176	939	-	-	0.50
20	1	9.5 - 10.0	9.750	1.95	0.35	334	861	217	0.41	1158	190.125	152	176	939	-	-	0.50
21	1	10.0 - 10.5	10.250	2.10	0.35	325	838	221	0.41	1181	197.75	158	176	939	1500	1940	0.50
22	1	10.5 - 11.0	10.750	2.10	0.35	327	844	224	0.41	1197	203.25	163	176	939	1600	1943	0.50
23	1	11.0 - 11.5	11.250	2.10	0.35	329	850	227	0.41	1213	208.75	167	176	939	1700	1945	0.50
24	1	11.5 - 12.0	11.750	2.10	0.35	331	855	230	0.41	1229	214.25	171	176	939	1800	1947	0.50
25	1	12.0 - 12.5	12.250	2.10	0.35	333	861	233	0.41	1245	219.75	176	176	939	1900	1950	0.50
26	1	12.5 - 13.0	12.750	2.10	0.35	335	866	236	0.41	1260	225.25	180	176	939	2000	1952	0.50
27	1	13.0 - 13.5	13.250	2.10	0.35	337	871	239	0.41	1275	230.75	185	176	939	2250	1955	0.50
28	1	13.5 - 14.0	13.750	2.10	0.35	339	876	242	0.41	1290	236.25	189	176	939	2250	1957	0.50
29	1	14.0 - 14.5	14.250	2.10	0.35	341	881	245	0.41	1305	241.75	193	176	939	2250	1959	0.50
30	1	14.5 - 15.0	14.750	2.10	0.35	343	886	248	0.41	1320	247.25	198	176	939	2250	1961	0.50
31	1	15.0 - 15.5	15.250	2.10	0.35	345	891	250	0.41	1335	252.75	202	176	939	2250	1964	0.50
32	1	15.5 - 16.0	15.750	2.10	0.35	347	896	253	0.41	1349	258.25	207	176	939	2250	1966	0.50
33	1	16.0 - 16.5	16.250	2.10	0.35	349	901	256	0.41	1363	263.75	211	176	939	2250	1968	0.50
34	1	16.5 - 17.0	16.750	2.10	0.35	351	906	258	0.41	1378	269.25	215	176	939	2250	1970	0.50
35	1	17.0 - 17.5	17.250	2.10	0.35	352	910	261	0.41	1392	274.75	220	176	939	2250	1972	0.50
36	1	17.5 - 18.0	17.750	2.10	0.35	354	915	264	0.41	1405	280.25	224	176	939	2250	1974	0.50
37	1	18.0 - 18.5	18.250	2.10	0.35	356	919	266	0.41	1419	285.75	229	176	939	2250	1976	0.50
38	1	18.5 - 19.0	18.750	2.10	0.35	358	924	269	0.41	1433	291.25	233	176	939	2250	1978	0.50

TABLE II–3. CONSTITUTIVE MODEL – ELASTIC PARAMETERS (CONT.)

39	1	19.0 - 19.5	19.250	2.10	0.35	359	928	271	0.41	1446	296.75	237	176	939	2250	1980	0.50
40	1	19.5 - 20.0	19.750	2.10	0.35	361	932	274	0.41	1460	302.25	242	176	939	2250	1982	0.50
41	1	20.0 - 20.5	20.250	2.10	0.35	363	936	276	0.41	1473	307.75	246	176	939	2250	1984	0.50
42	1	20.5 - 21.0	20.750	2.10	0.35	364	940	279	0.41	1486	313.25	251	176	939	2250	1986	0.50
43	1	21.0 - 21.5	21.250	2.10	0.35	366	945	281	0.41	1499	318.75	255	176	939	2250	1988	0.50
44	1	21.5 - 22.0	21.750	2.10	0.35	367	949	283	0.41	1512	324.25	259	176	939	2250	1990	0.50
45	1	22.0 - 22.5	22.250	2.10	0.35	369	953	286	0.41	1525	329.75	264	176	939	2250	1992	0.50
46	1	22.5 - 23.0	22.750	2.10	0.35	370	957	288	0.41	1537	335.25	268	176	939	2250	1994	0.50
47	1	23.0 - 23.5	23.250	2.10	0.35	372	960	291	0.41	1550	340.75	273	176	939	2250	1996	0.50
48	1	23.5 - 24.0	23.750	2.10	0.35	373	964	293	0.41	1562	346.25	277	176	939	2250	1998	0.50
49	1	24.0 - 24.5	24.250	2.10	0.35	375	968	295	0.41	1575	351.75	281	176	939	2250	2000	0.50
50	1	24.5 - 25.0	24.750	2.10	0.35	376	972	298	0.41	1587	357.25	286	176	939	2250	2001	0.50
51	1	25.0 - 25.5	25.250	2.10	0.35	378	976	300	0.41	1599	362.75	290	176	939	2250	2003	0.50
52	1	25.5 - 26.0	25.750	2.10	0.35	379	979	302	0.41	1611	368.25	295	176	939	2250	2005	0.50
53	1	26.0 - 26.5	26.250	2.10	0.35	381	983	304	0.41	1623	373.75	299	176	939	2250	2007	0.50
54	1	26.5 - 27.0	26.750	2.10	0.35	382	987	307	0.41	1635	379.25	303	176	939	2250	2009	0.50
55	1	27.0 - 27.5	27.250	2.10	0.35	383	990	309	0.41	1647	384.75	308	176	939	2250	2010	0.50
56	1	27.5 - 28.0	27.750	2.10	0.35	385	994	311	0.41	1659	390.25	312	176	939	2250	2012	0.50
57	1	28.0 - 28.5	28.250	2.10	0.35	386	997	313	0.41	1670	395.75	317	176	939	2250	2014	0.50
58	1	28.5 - 29.0	28.750	2.10	0.35	388	1001	315	0.41	1682	401.25	321	176	939	2250	2016	0.50
59	1	29.0 - 29.5	29.250	2.10	0.35	389	1004	317	0.41	1693	406.75	325	176	939	2250	2017	0.50
60	1	29.5 - 30.0	29.750	2.10	0.35	390	1007	320	0.41	1705	412.25	330	176	939	2250	2019	0.50
61	1	30.0 - 31.0	30.500	2.00	-	346	1766	240	0.48	5920	420.00	398	-	-	-	1766	-
62	1	30.8 - 32.0	31.500	2.00	-	346	1766	240	0.48	5920	430.00	407	-	-	-	1766	-
63	1	31.8 - 33.0	32.500	2.00	-	346	1766	240	0.48	5920	440.00	417	-	-	-	1766	-
64	1	32.8 - 34.0	33.500	2.00	-	346	1766	240	0.48	5920	450.00	426	-	-	-	1766	-
65	1	33.8 - 35.0	34.500	2.00	-	346	1766	240	0.48	5920	460.00	435	-	-	-	1766	-
66	1	34.8 - 36.0	35.500	2.00	-	346	1766	240	0.48	5920	470.00	445	-	-	-	1766	-
67	1	35.8 - 37.0	36.500	2.00	-	346	1766	240	0.48	5920	480.00	454	-	-	-	1766	-
68	1	36.8 - 38.0	37.500	2.00	-	346	1766	240	0.48	5920	490.00	464	-	-	-	1766	-
69	1	37.8 - 39.0	38.500	2.00	-	346	1766	240	0.48	5920	500.00	473	-	-	-	1766	-
70	1	38.8 - 40.0	39.500	2.00	-	346	1766	240	0.48	5920	510.00	483	-	-	-	1766	-
71	1	39.8 - 41.0	40.500	2.00	-	346	1766	240	0.48	5920	520.00	492	-	-	-	1766	-
72	1	40.8 - 42.0	41.500	2.00	-	346	1766	240	0.48	5920	530.00	502	-	-	-	1766	-
73	1	41.8 - 43.0	42.500	2.00	-	346	1766	240	0.48	5920	540.00	511	-	-	-	1766	-
74	1	42.8 - 44.0	43.500	2.00	-	346	1766	240	0.48	5920	550.00	521	-	-	-	1766	-
75	1	43.8 - 45.0	44.500	2.00	-	346	1766	240	0.48	5920	560.00	530	-	-	-	1766	-
76	1	44.8 - 46.0	45.500	2.00	-	346	1766	240	0.48	5920	570.00	540	-	-	-	1766	-
77	1	45.8 - 47.0	46.500	2.00	-	346	1766	240	0.48	5920	580.00	549	-	-	-	1766	-
78	1	46.8 - 48.0	47.500	2.00	-	346	1766	240	0.48	5920	590.00	559	-	-	-	1766	-
79	1	47.8 - 49.0	48.500	2.00	-	346	1766	240	0.48	5920	600.00	568	-	-	-	1766	-
80	1	48.8 - 50.0	49.500	2.00	-	346	1766	240	0.48	5920	610.00	577	-	-	-	1766	-
81	1	> 50	-	2.40	-	1200	3000	3456	0.40	16128	-	-	-	-	-	2939	-

TABLE II–4. CONSTITUTIVE PARAMETERS – YIELD AND FAILURE PARAMETERS

Sandy Gravel (0 < z < 30m)

	Best estimate
Friction angle at failure ϕ (°)	42
Drained cohesion c (kPa)	10
Coefficient of lateral stress K_0	0.7
Stress-strain curve parameters (equation (II–15))	
α	0.5
x_ℓ	0.1
x_u	0.9

Stiff Clay

	Best estimate
Friction angle at failure ϕ (°)	0
Cohesion c_u (MPa)	0.30
Stress-strain curve parameters (equation (II–15))	
α	8.0
x_ℓ	0.3
x_u	1.0

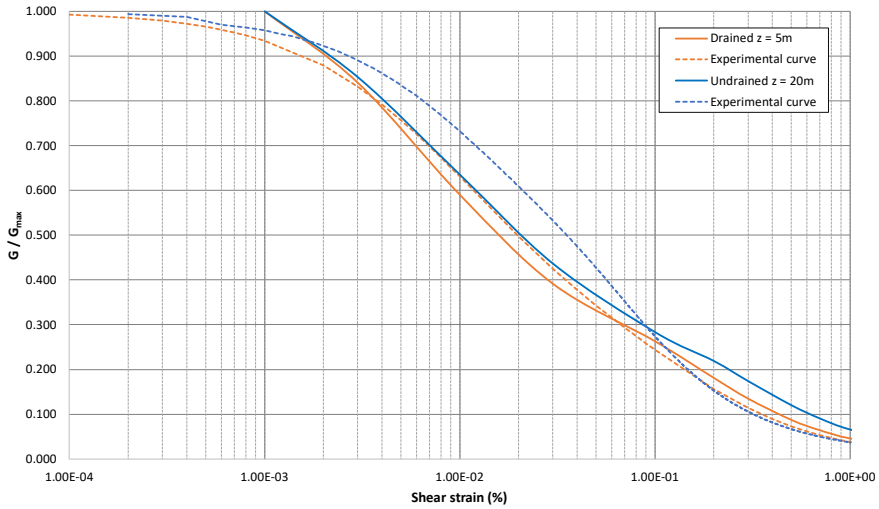

Fig. II–2. Cyclic simple shear tests on sandy gravel at 5m depth (drained test) and at 20m depth (undrained test).

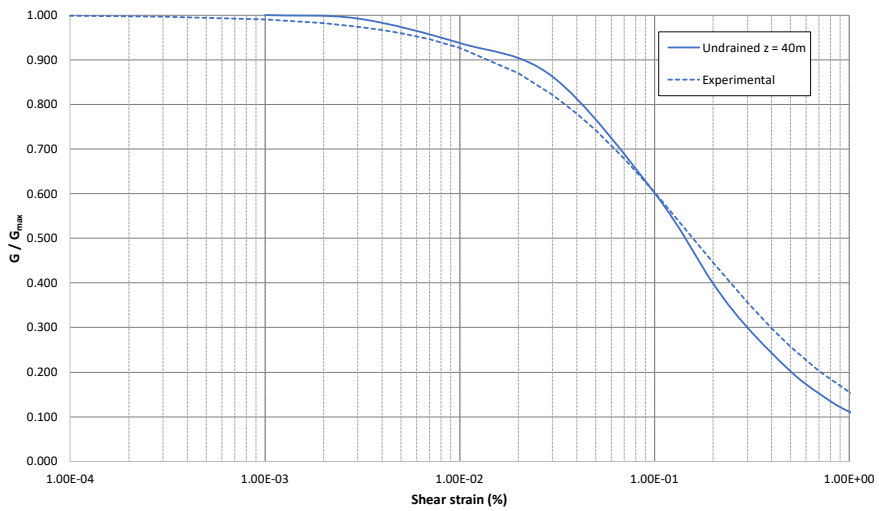

Fig. II–3. Cyclic undrained shear test on stiff clay at 40m.

II–5.5. Dilation Parameters

This part only applies to the sandy gravel. The determination of the dilation parameters is based on the following assumptions: the ratio $\frac{\tan\dot{\phi}}{\tan\phi}$ is equal to 0.75 and consistent with results presented in the literature. This ratio is applied to the friction angle determined in above, giving an angle of phase transformation equal to 34°. This value is given in Table II–5.

Drained triaxial compression tests have been simulated numerically with an assumed X_{pp} parameter equal to 0.2. Figure II–4 presents such a simulation for a test conducted under a confining pressure of 80 kPa.

TABLE II–5. CONSTITUTIVE PARAMETERS – DILATION PARAMETERS

Sandy Gravel

		(°)
Dilation angle $\bar{\phi}$	Above water table	34
	Below water table	34
Dilation parameter X_{pp}	Above water table	0.20
	Below water table	0.005

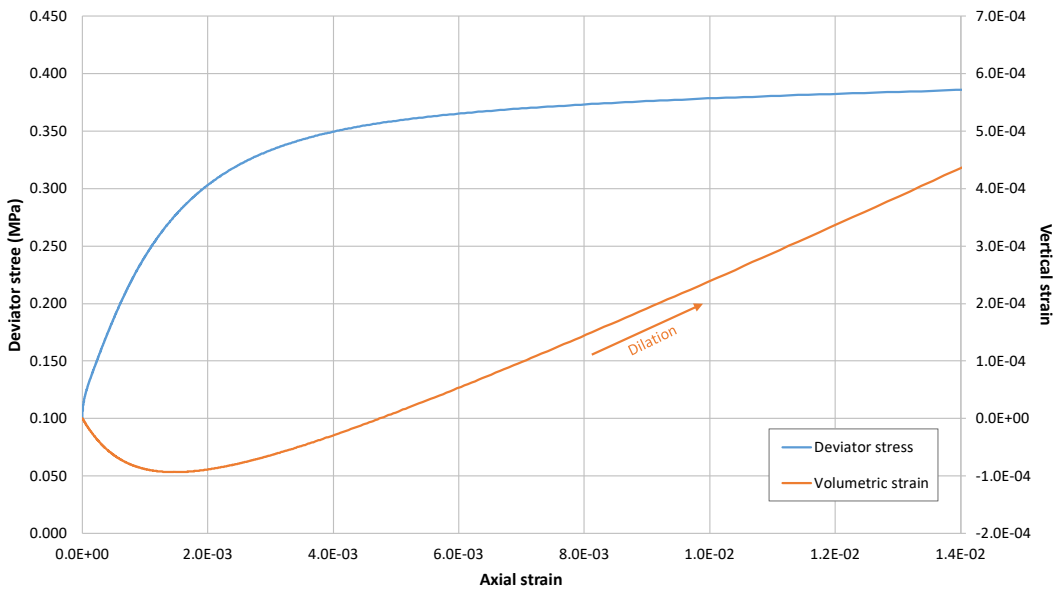

Fig. II–4. Sandy gravel – Drained triaxial compression test at 5m depth.

The slope of the "straight" line beyond the characteristic state (defined as $\dot{\varepsilon}_v = 0$) is related to the dilation angle ψ by the following relationship:

$$\frac{d\varepsilon_v}{d\varepsilon_1} = \frac{2\sin\psi}{1-\sin\psi} \tag{II–28}$$

The computed dilation angle is equal to

$$\psi = 1.5° \tag{II–29}$$

For the soil under the water table, to prevent liquefaction the value of X_{PP} is taken equal to 0.005.

II–6. TIME HISTORY

The database was browsed to find an event with a magnitude included between 6.5 and 7.5, recorded at less than 20km from the source on a rock material (V_S > 750m/s) and presenting a broadband frequency smooth spectrum.

The Iwate earthquake with magnitude 6.9 (M_w) in Japan (14/06/2008) recorded at the rock station (V_S = 825m/s) IWT010, located 16km away (Joyner-Boore distance) from the source, has been retained (component NS).

The acceleration, velocity and displacement time histories are shown in Figs II–5 to Figs II–7.

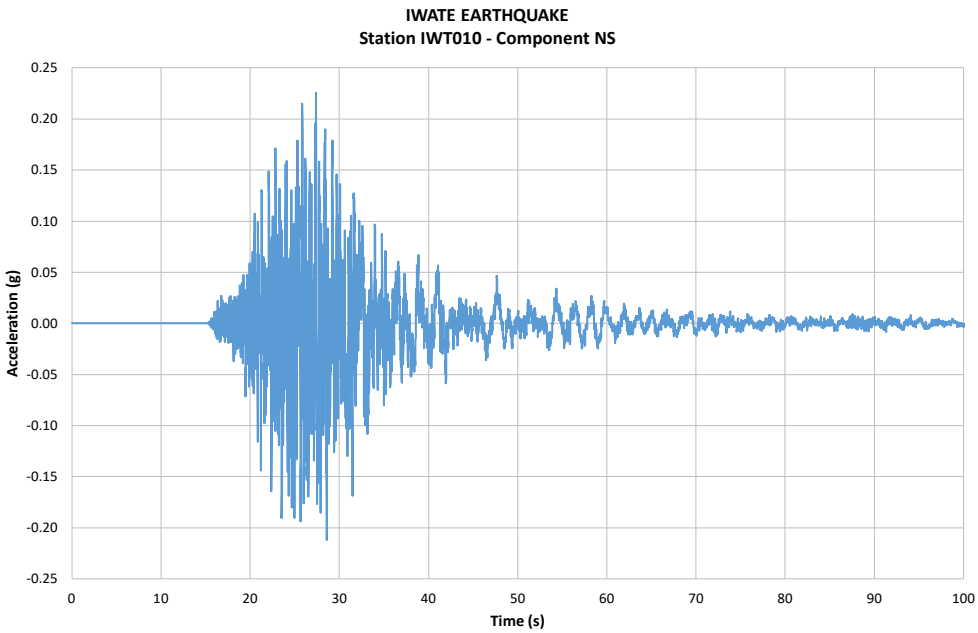

Fig. II–5. Acceleration time history.

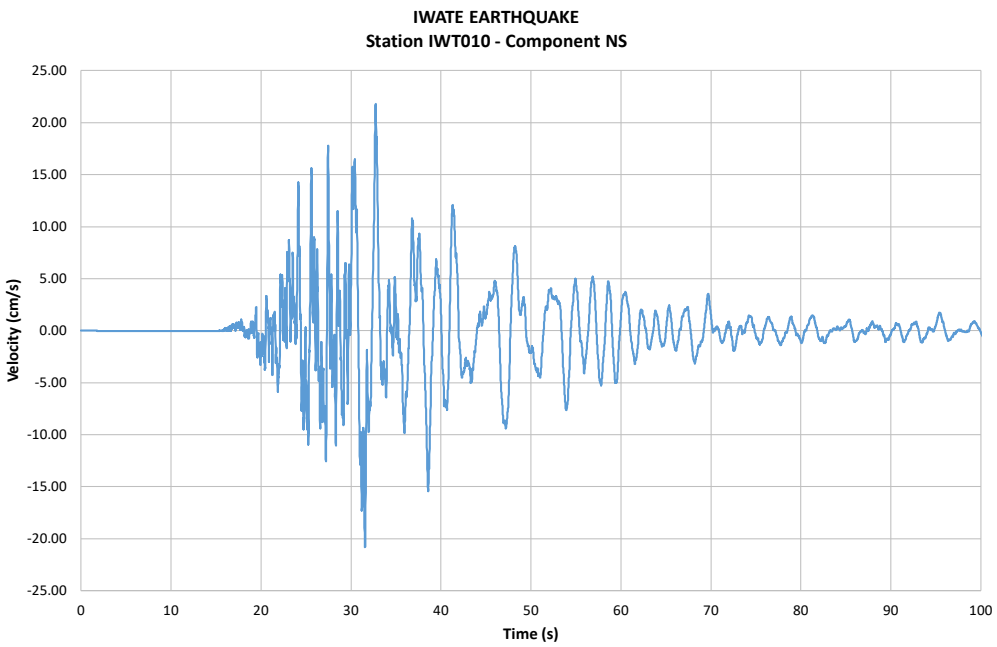

Fig. II–6. Velocity time history.

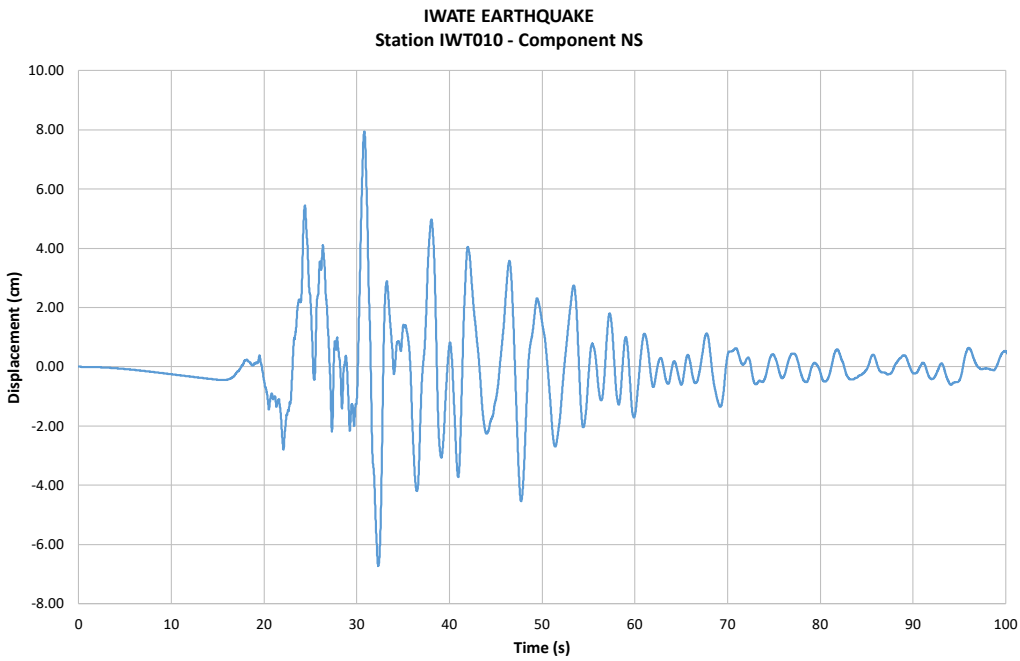

Fig. II–7. Displacement time history.

The 5% damped response spectrum is shown in Figure II.8.

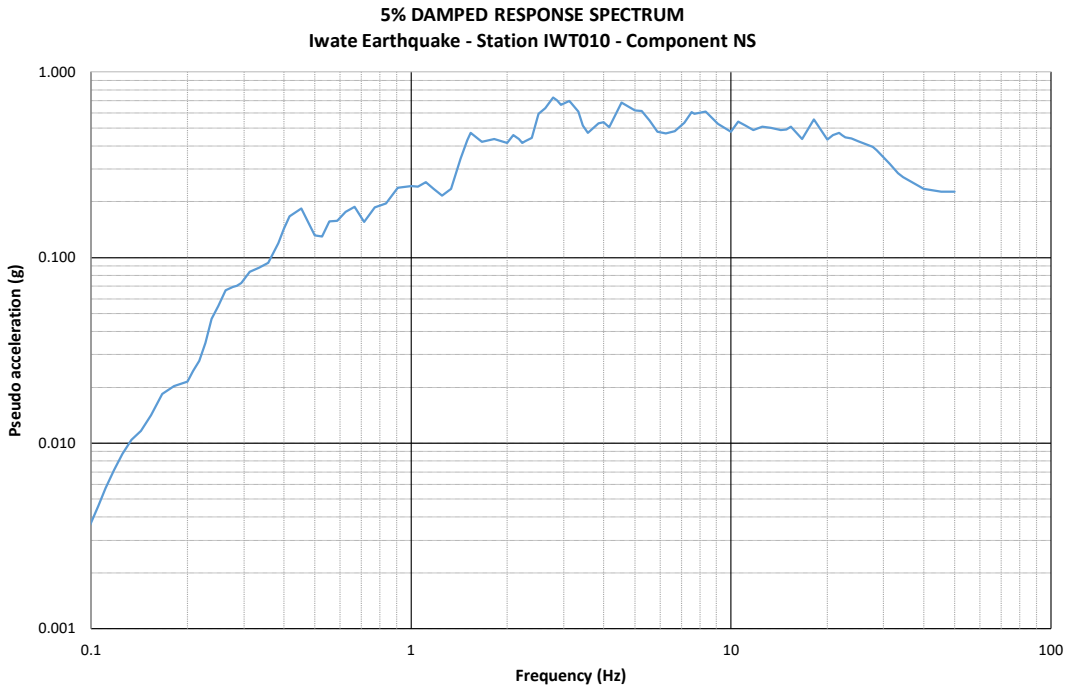

Fig. II–8. 5% damped response spectrum.

II–7. FINITE ELEMENT MODELLING

The soil column is discretized in one dimensional finite element with two nodes; each node possesses two (or four) degrees of freedom. The vertical dimension of the finite element mesh size is set according to the following criterion:

$$0.50m \leq h\frac{V_S}{10f_{max}} \qquad \text{(II–30)}$$

where f is the maximum frequency of interest (taken equal to 25 Hz) and V_s the soil shear wave velocity. The lower limit (0.50m) is set to prevent numerical instabilities due to high frequencies of individual elements.
Since the soil column is expected to be highly non-linear for the levels of earthquake shaking considered in the analysis, and given the elastic shear wave velocities V_s, the element size has been set equal to 0.50m along the whole depth of the gravel layer. In the clay the element thickness is taken equal to 1m.

II–8. STUDIED CASE

Studied cases are presented in Table II–6. The purpose of the analyses are:

- Show the differences between equivalent linear (EqL) and non-linear (NL) calculations as a function of input amplitude; the input PGA is taken equal to 0.10g, 0.25g and 050g by scaling up or down the time history presented above;
- Show the differences of total vs effective stress analyses as a function of permeability;

- Compare the predicted vertical motion assuming P-wave propagation to the motion calculated from the horizontal motion with V/H GMPEs [II–15, II–16].

It needs to be noted that:

- The material properties for the SHAKE analyses (G/G_{max} curves) will be computed from the constitutive model presented in soil profile and constitutive parameters (above) in order to ensure full compatibility of the input parameters between the EqL and NL analyses.
- The linear calculations with Dynaflow (case 1b) will consider the strain compatible properties calculated with Shake + Rayleigh damping.
- The P-wave analyses in Shake or Dynaflow (cases 6a–6b) are run with the V_S strain compatible properties calculated for the horizontal motion (no further iterations on G and β); V_P will be calculated assuming a constant bulk modulus (equal to the elastic one) and the strain compatible shear modulus.
- The 1-phase analyses in effective stresses (cases 2a–2b and 7a–7b) are run with a penalty formulation for the bulk modulus.

TABLE II–6. STUDIED CASES

Case	1a – 1b	2a – 2b	3	4	**5**	**6**
Continuum	1-Phase	1-Phase 2-Phase	2-Phase	2-Phase	2-Phase	2-Phase
Model	Total stresses	Effective stresses	Effective stresses	Effective stresses	Effective stresses	Effective stresses
Constitutive relationship	Equivalent linear/nonlinear	Elastoplastic	Elastoplastic	Elastoplastic	Elastoplastic	Elastoplastic
Permeability (m/s)	-	0	10^{-5}	10^{-4}	10^{-3}	10^{-2}
Input motion	Horizontal	Horizontal	Horizontal	Horizontal	Horizontal	Horizontal
Software	Shake Dynaflow	Dynaflow	Dynaflow	Dynaflow	Dynaflow	Dynaflow
Case	6a – 6b	7a – 7b	8	9		
Continuum	1-Phase	1-Phase 2-Phase	2-Phase	2-Phase		
Model	Total stresses	Effective stresses	Effective stresses	Effective stresses		
Constitutive relationship	Equivalent linear/ linear	Elastoplastic	Elastoplastic	Elastoplastic		
Permeability (m/s)	-	0	10^{-5}	10^{-2}		
Input motion	Horizontal + vertical	Horizontal + vertical	Horizontal + vertical	Horizontal + vertical		
Software	Shake Dynaflow	Dynaflow	Dynaflow	Dynaflow		

II–8.1. Example 1. Comparison of equivalent linear and non-linear site response analyses (Cases 1a–1b)

Figures II–9 – II–11 show that as long as the input motion is not too strong (here PGA ~ 0.20g) the EqL and NL solutions do not differ significantly. For 0.25g differences start to appear in the acceleration response spectra: high frequencies are filtered out in the EqL solution (see Section 3) and a peak appears at 3Hz corresponding to the natural frequency of the soil column. At 0.5g the phenomena are amplified with in particular a sharp peak at 2.8Hz in the EqL solution.

The value of the PGA threshold should not be considered as a universal value: it depends on the material behaviour. The example is used to point out that beyond some level EqL solution are not valid.

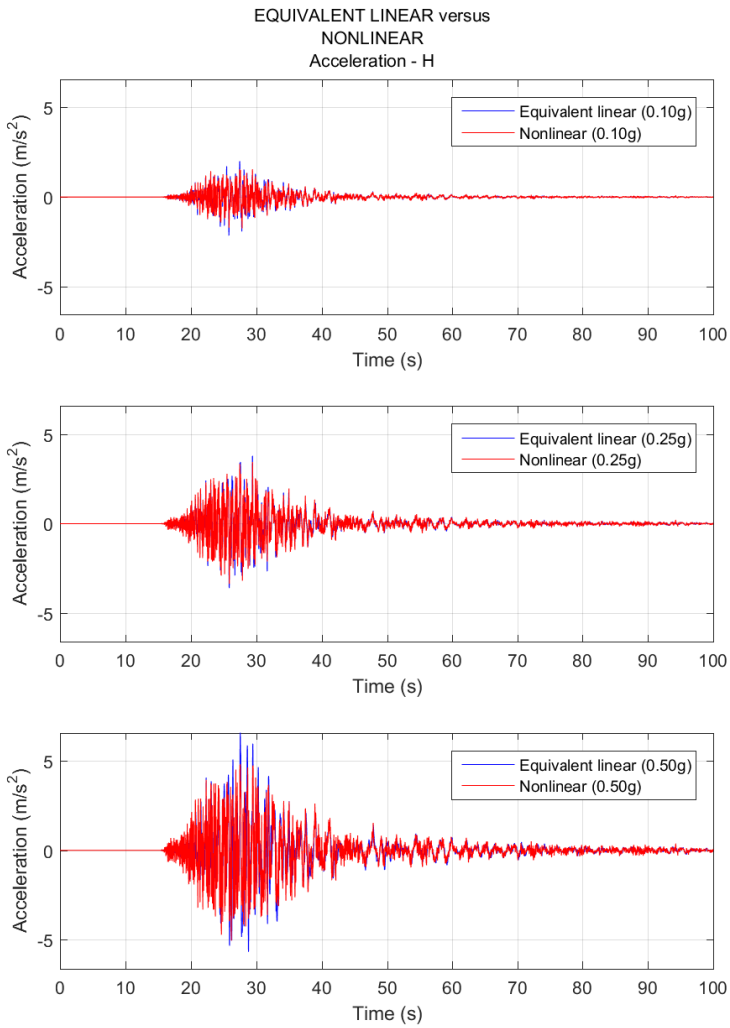

Fig. II–9. Equivalent linear versus non-linear – Acceleration – H.

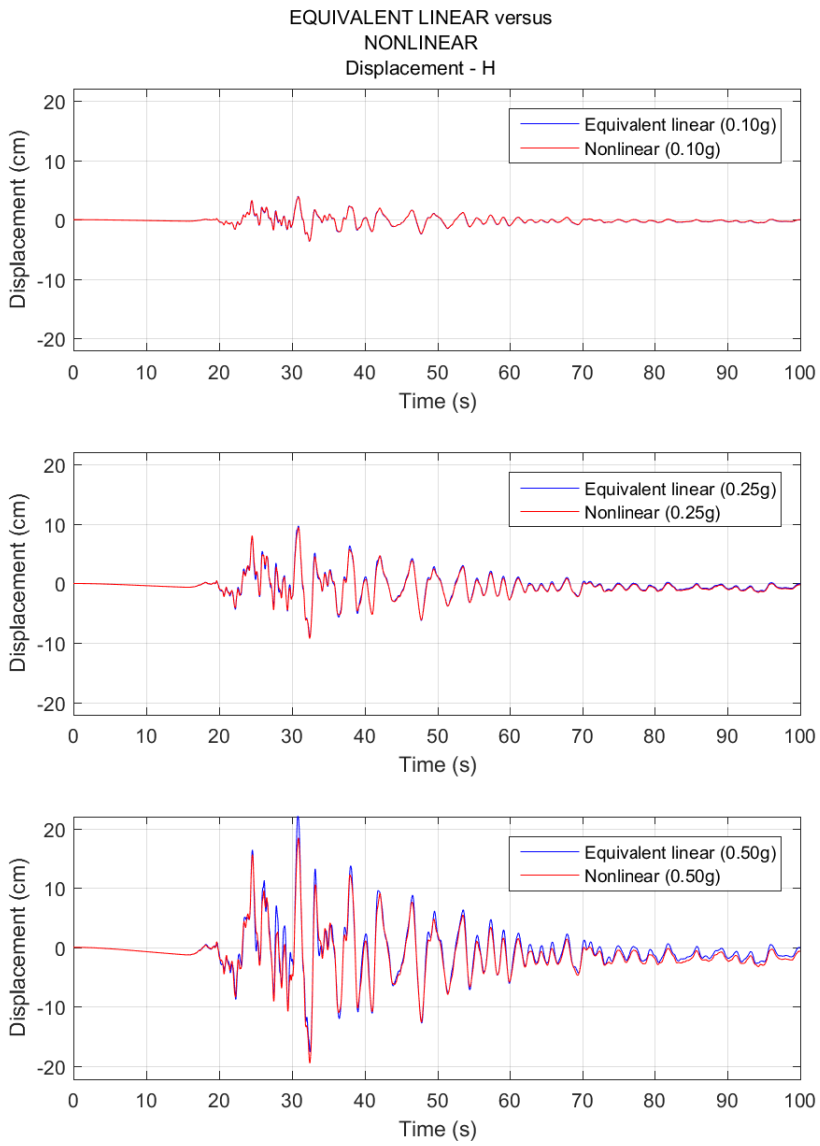

Fig. II–10. Equivalent linear versus non-linear – Displacement – H.

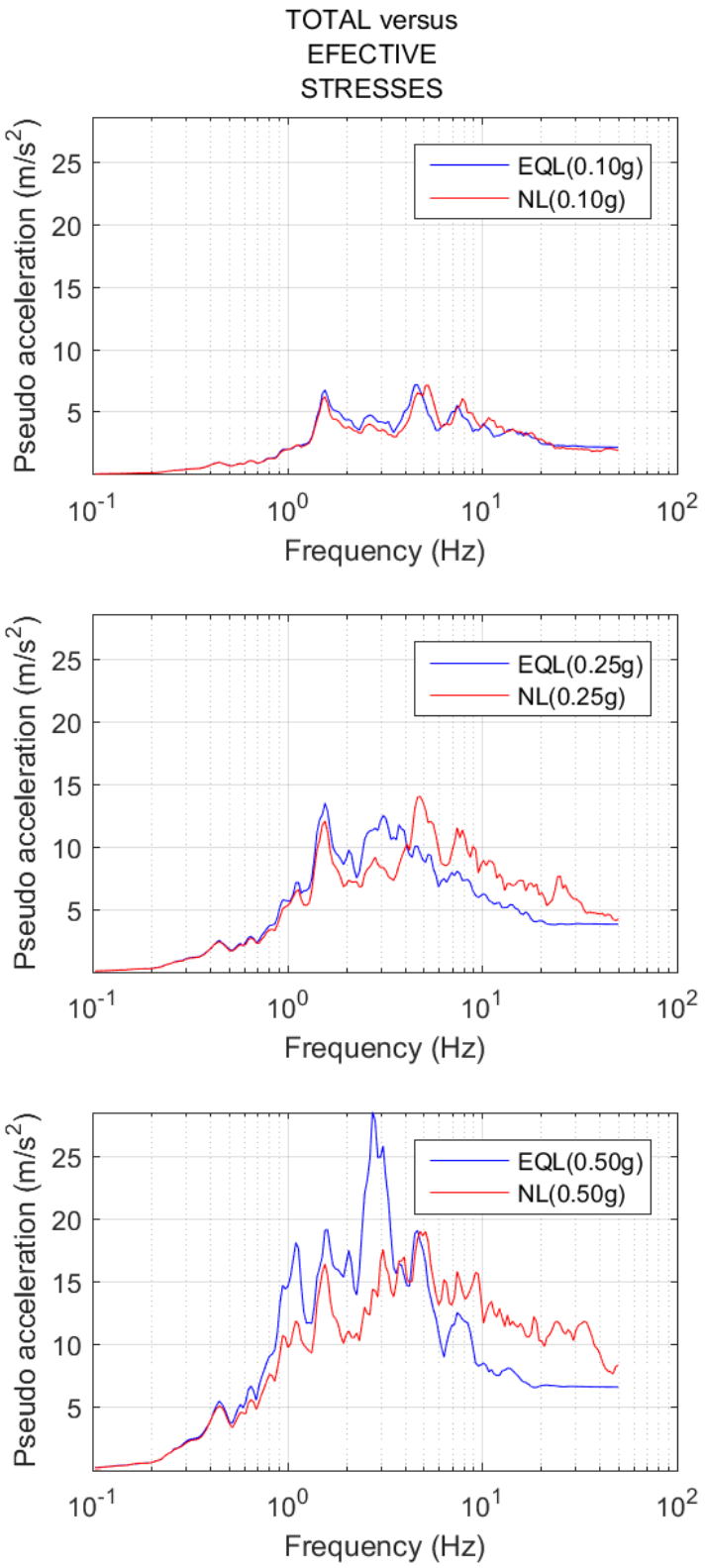

Fig. II–11. Total versus effective stresses – Acceleration.

II–8.2. Example 2. Comparison of total versus effective stresses analyses (Cases 1a–2a)

Figures II–12– II–15 present the results. At low level of excitation (PGA ≤ 0.25g) both solutions (total or effective stress analyses) are comparable except of course for the pore pressure build up that cannot be predicted by the total stress analysis. At PGA = 0.50g differences appear in the acceleration response spectra and in the vertical displacements. It can be concluded that effective stress analyses are not needed for low level of excitation but are important for high levels when the excess pore pressure becomes significant.

The value of the PGA threshold should not be considered as a universal value: it depends on the material behaviour. The example is used to point out that beyond some level total stress analyses cannot predict the correct solution.

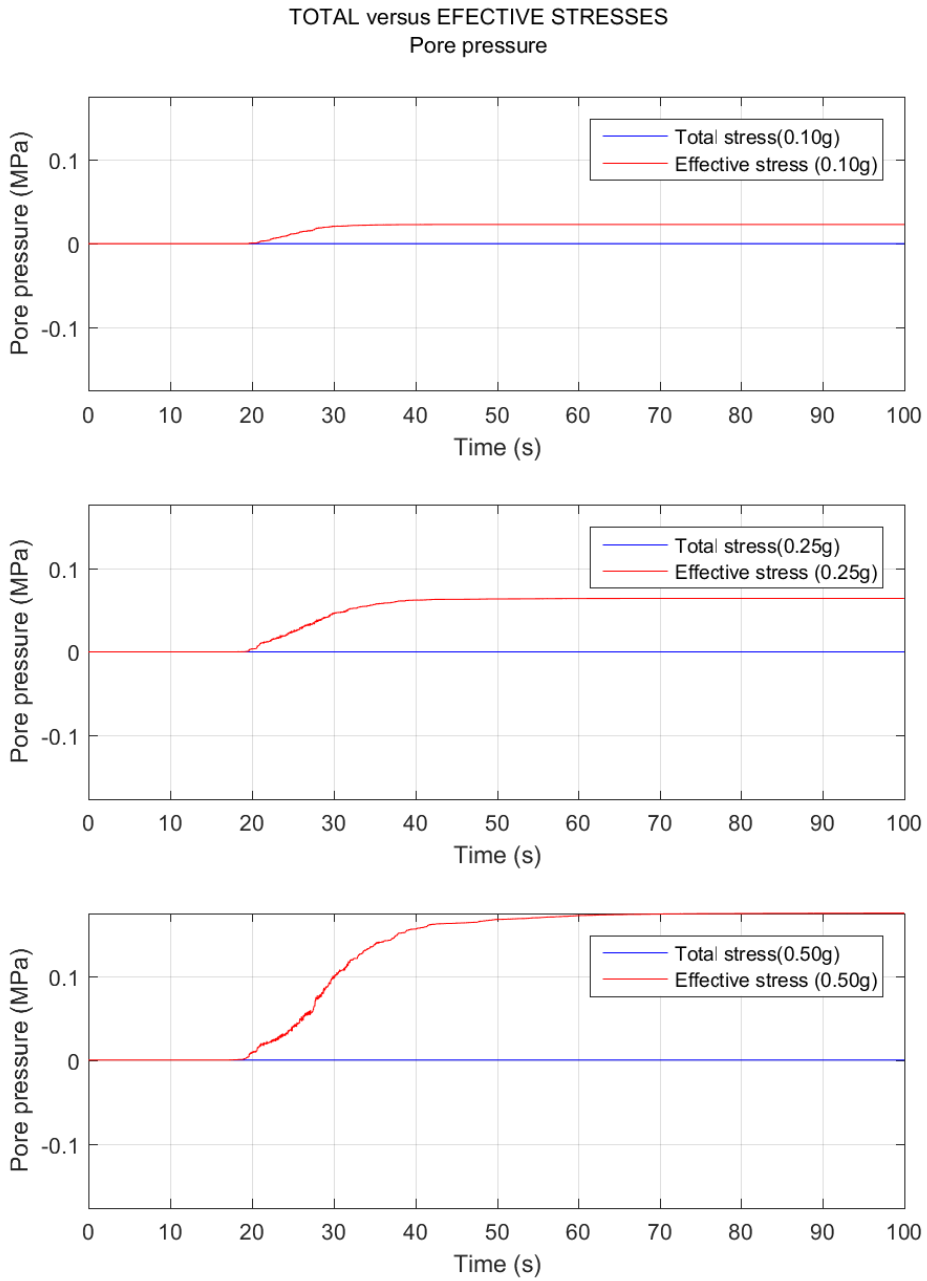

Fig. II–12. Total versus effective stresses – Pore pressure.

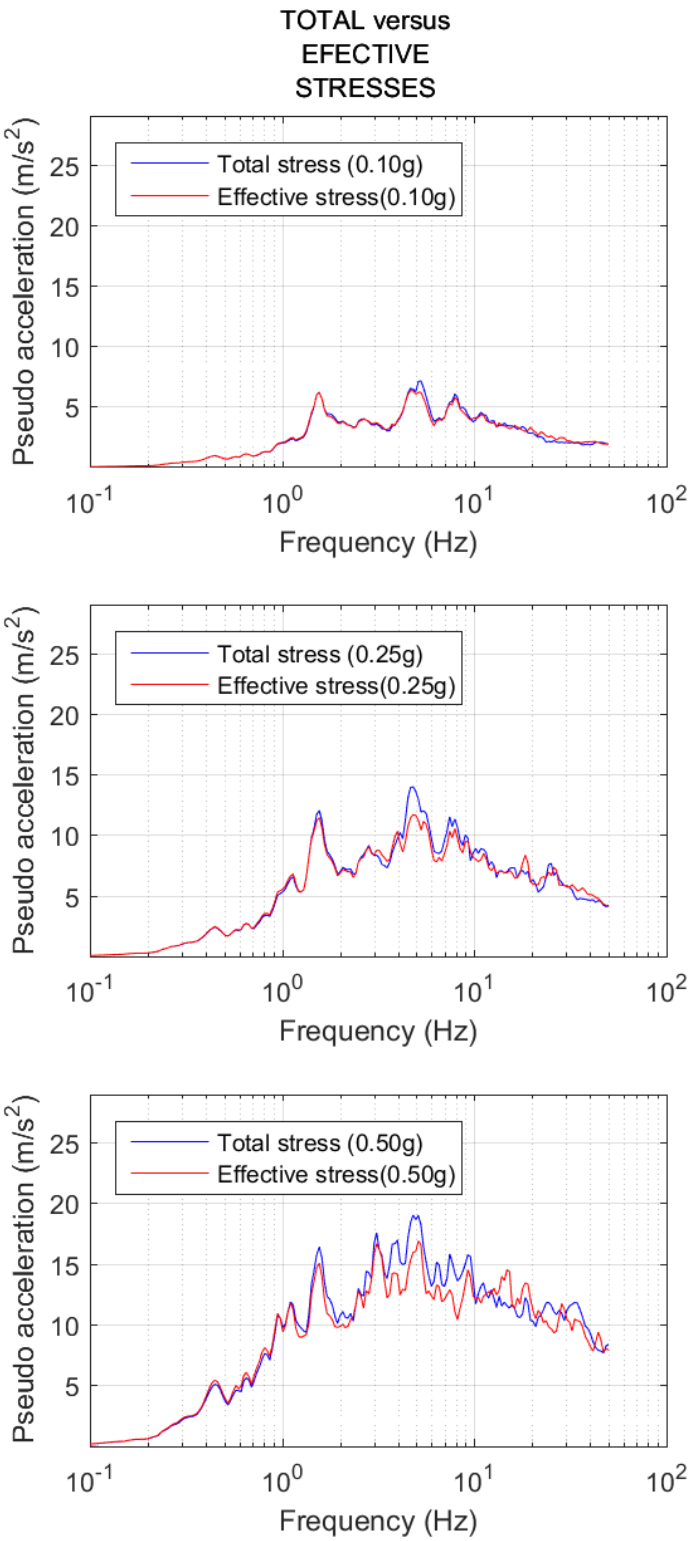

Fig. II–13. Total versus effective stresses – Acceleration.

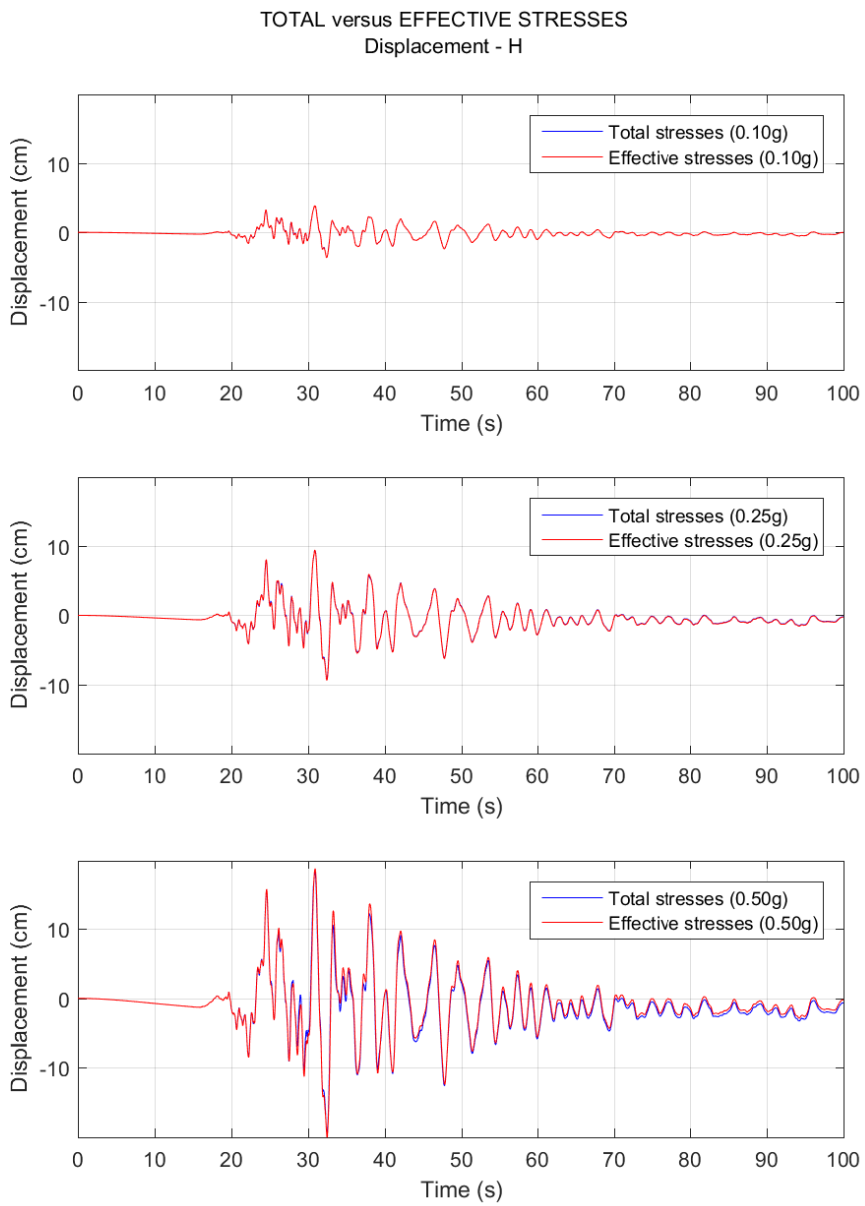

Fig. II–14. Total versus effective stresses – Displacement – H.

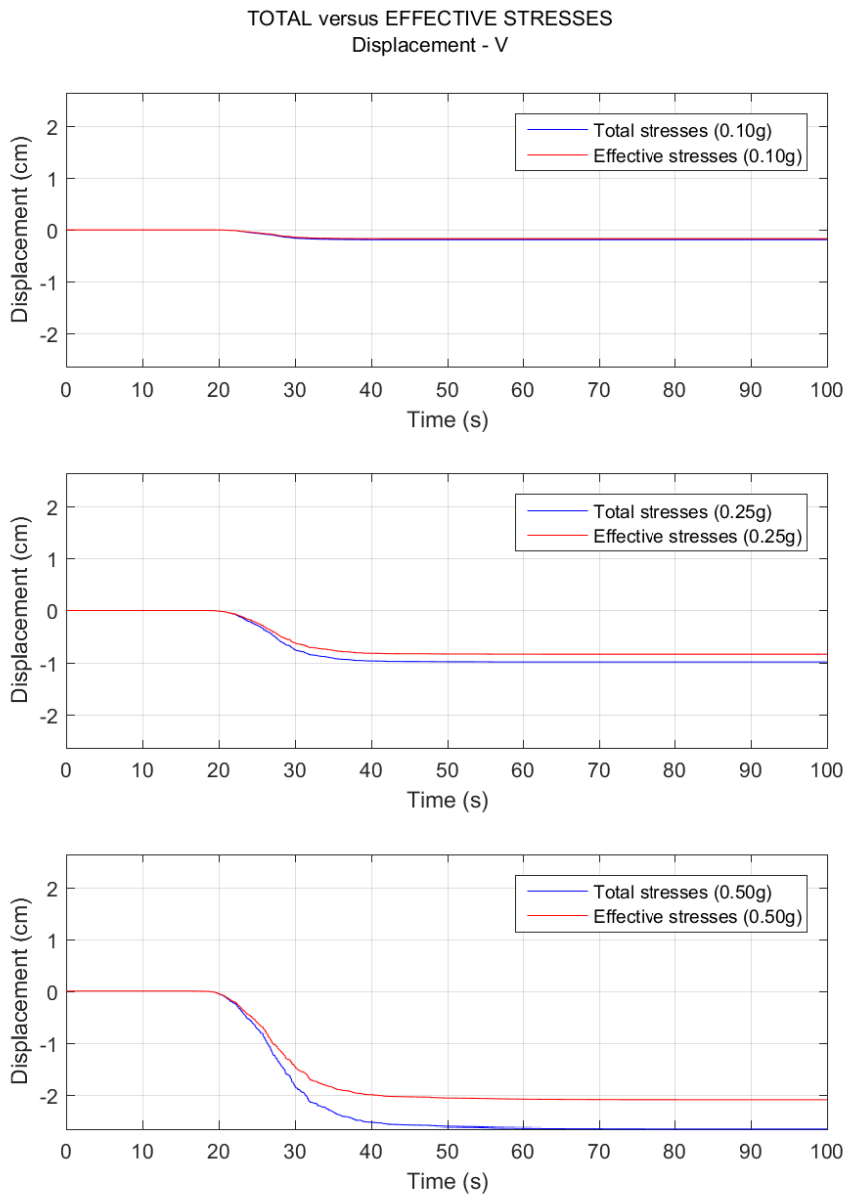

Fig. II–15. Total versus effective stresses – Displacement – V.

II–8.3. Examples 3. Comparison of 1–phase versus 2–phase effective stress analyses (Case 2a–2b)

Figures II–16– II–19 present the results. For an impervious material the effective stress analyses carried out assuming either a 1–phase medium or a 2–phase medium do not show any significant differences. Based on the results of other analyses, not presented herein, this statement holds as long as the permeability is smaller than approximately 10^{-4} m/s. Therefore, 2–phase analyses are not needed for these permeabilities.

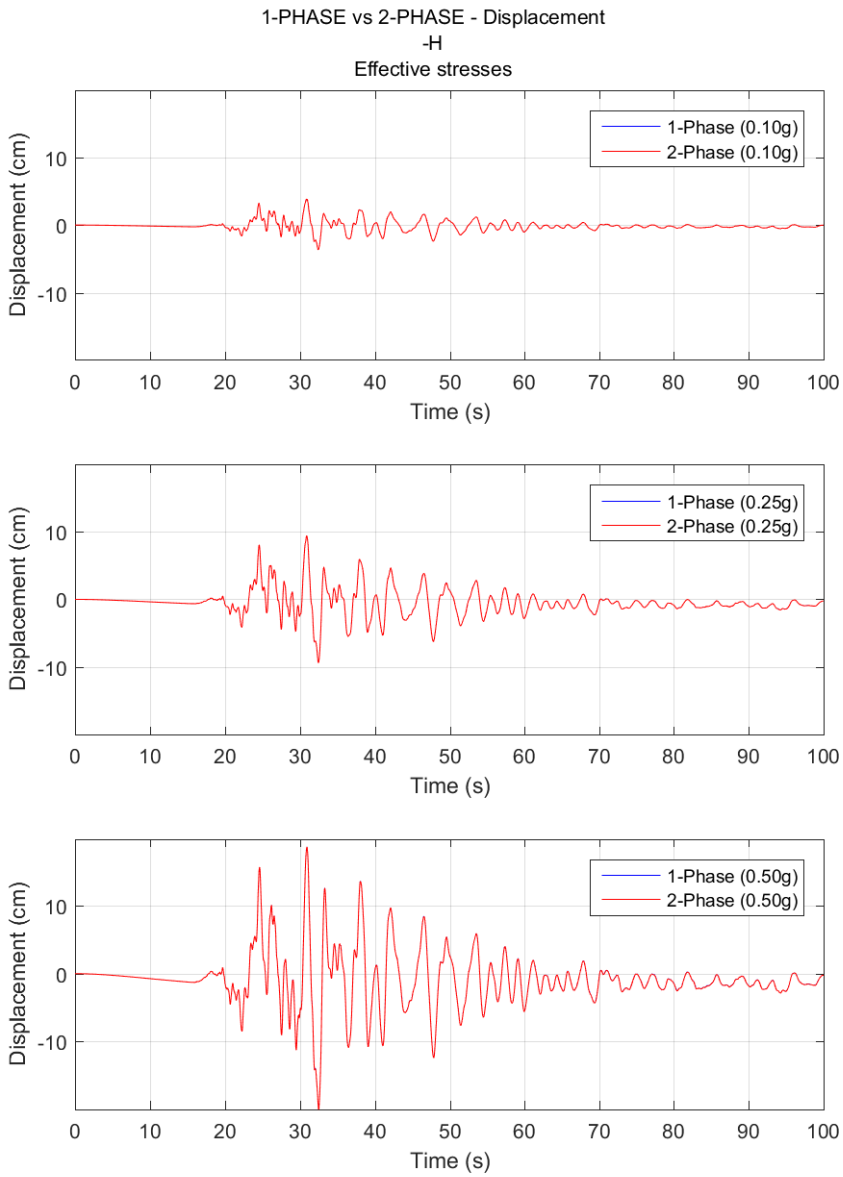

Fig. II–16. 1-Phase versus 2-Phase – Displacement – H – Effective Stresses.

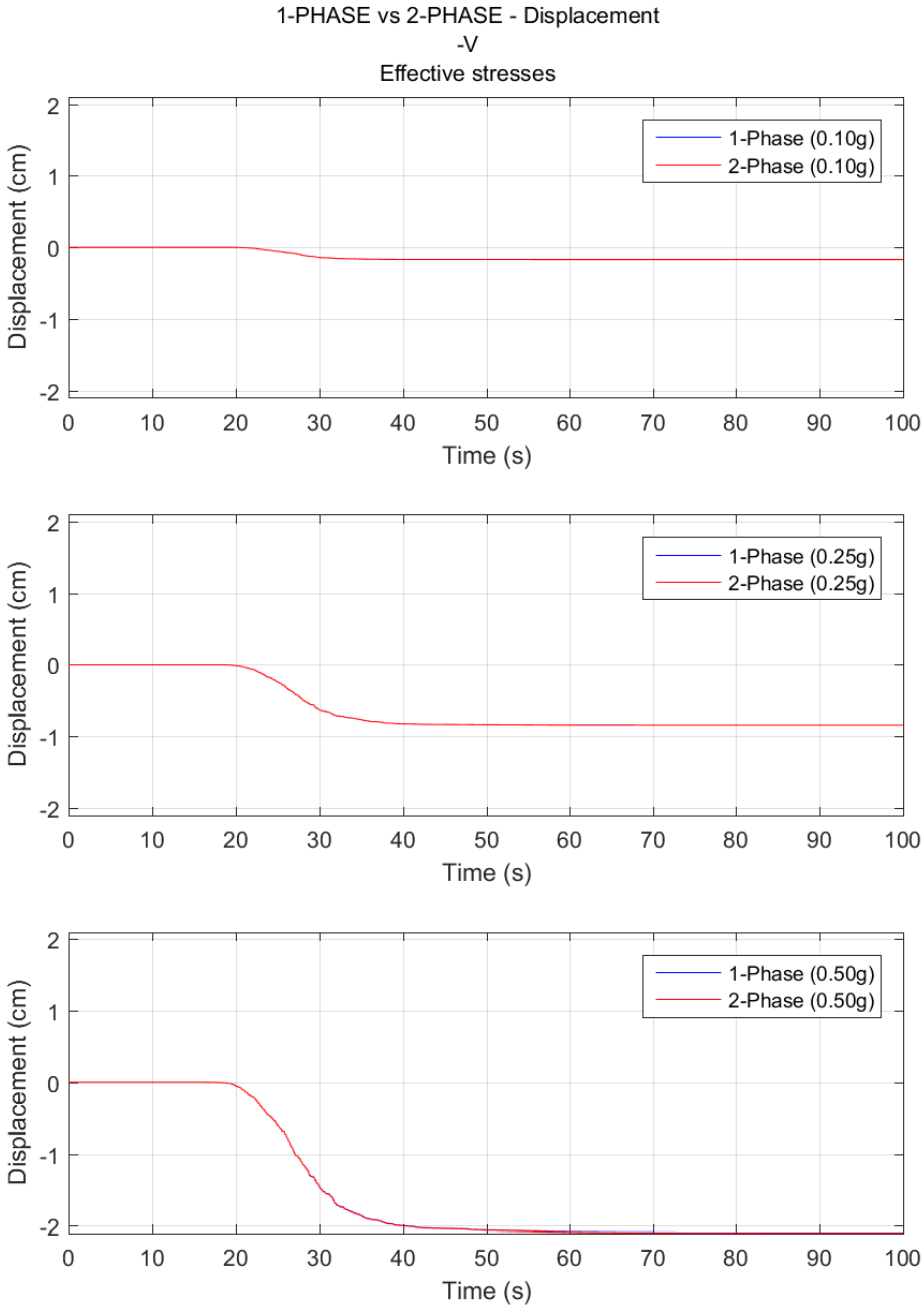

Fig. II–17. 1-Phase versus 2-Phase – Displacement V – Effective stresses.

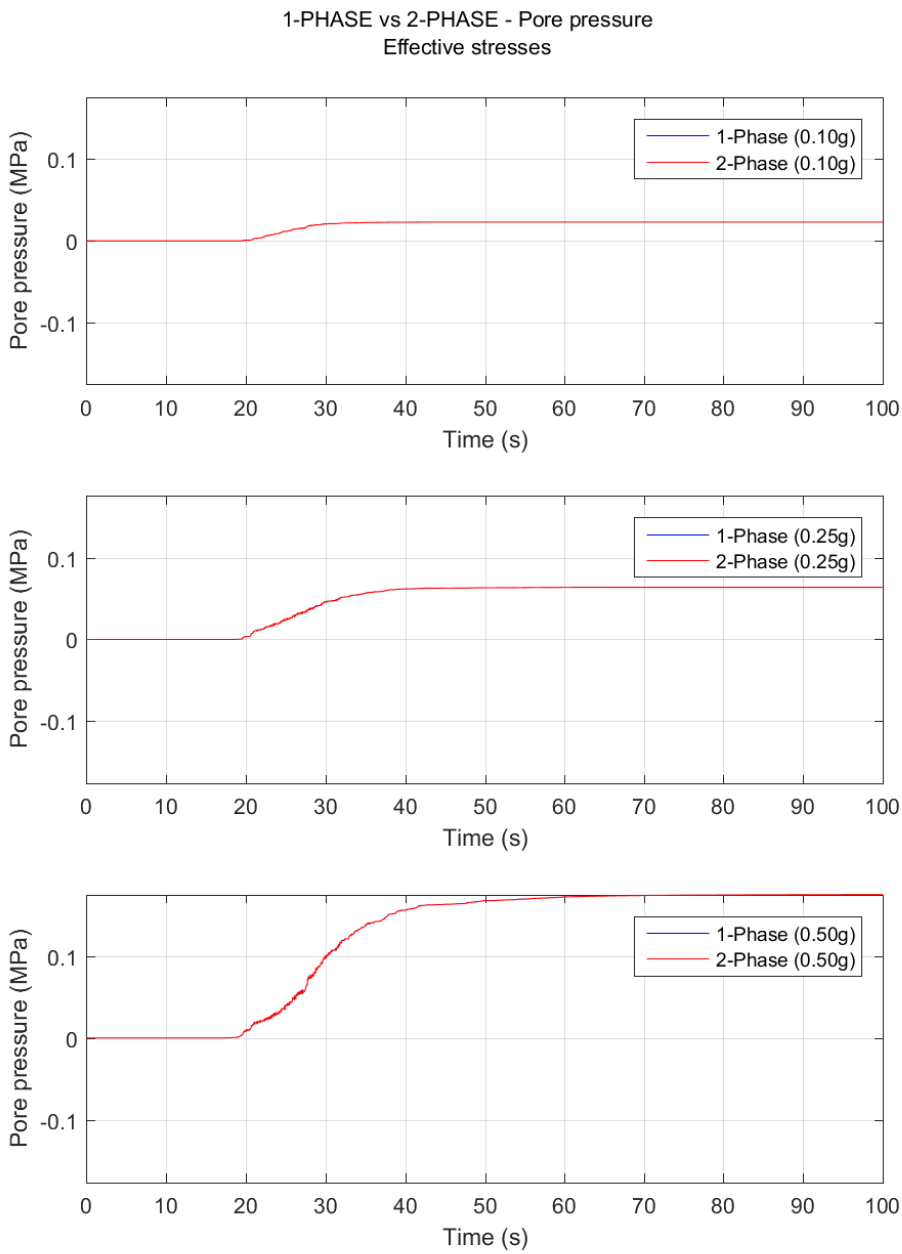

Fig. II–18. 1-Phase versus 2-Phase – Pore pressure – Effective stresses.

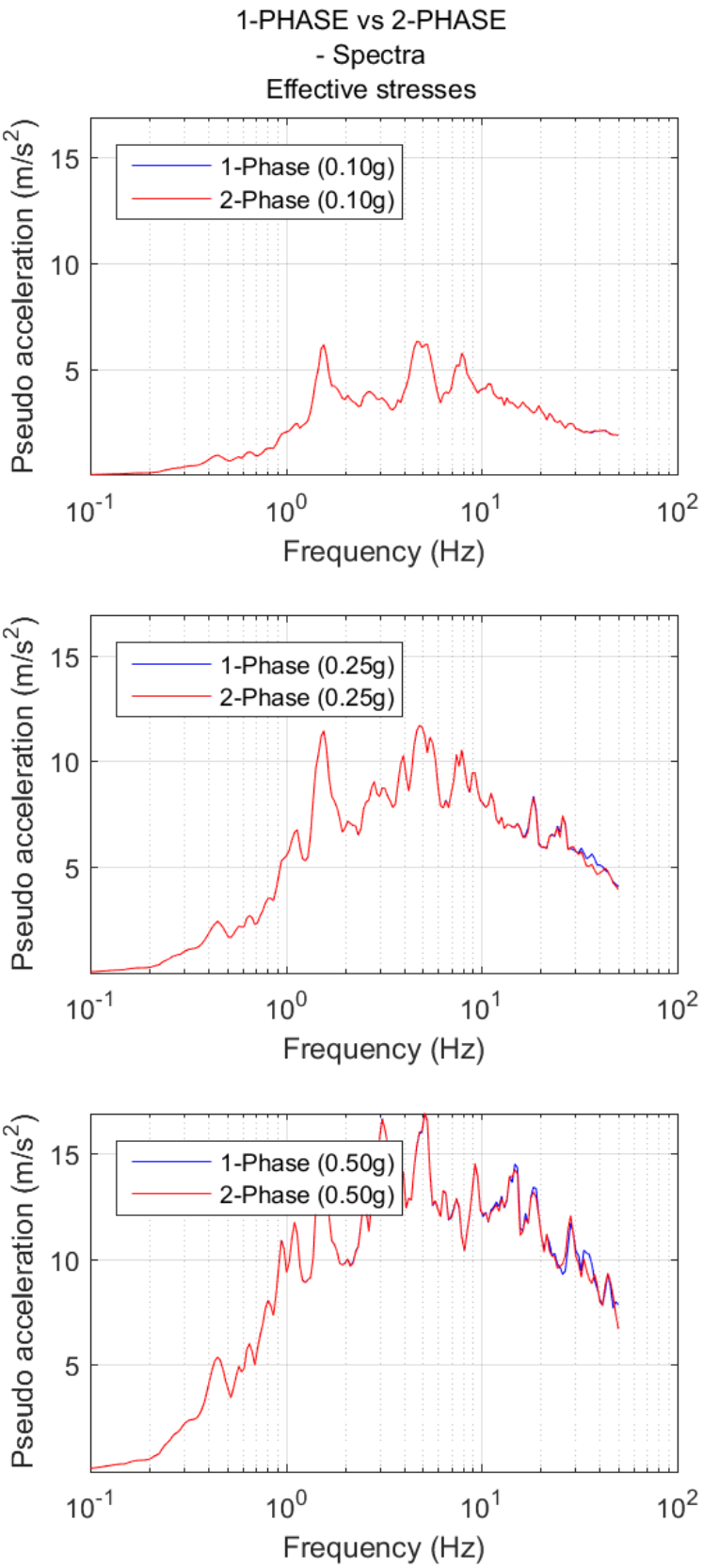

Fig. II–19. 1-Phase versus 2-Phase – Spectra – Effective stresses.

II–8.4. Example 4. 2–Phase effective stresses analyses, influence of permeability (Cases 2b and 3–6)

Figures II–20 – II–23 present the results. The impact of the value of the permeability appears to be minor on all parameters but the excess pore pressure. It is only for high permeabilities (10^{-2} m/s) and high input excitation that differences appear in the acceleration response spectrum and to a minor extent in the vertical displacement. However, distributions of excess pore pressures are significantly impacted by the permeabilities, for moderate to high input excitation; this parameter must not be overlooked as it controls the strength of the soil and may affect the stability of structures. Only for permeabilities smaller than 10^{-5}m/s can the permeability be neglected, and the soil assumed to behave fully undrained.

Again, the exact value of the permeability threshold depends on the material behaviour; the example is used to point out that below some values the response will be correctly predicted assuming undrained behaviour. Based on similar calculations by others, it seems however that the value indicated above is fairly reliable.

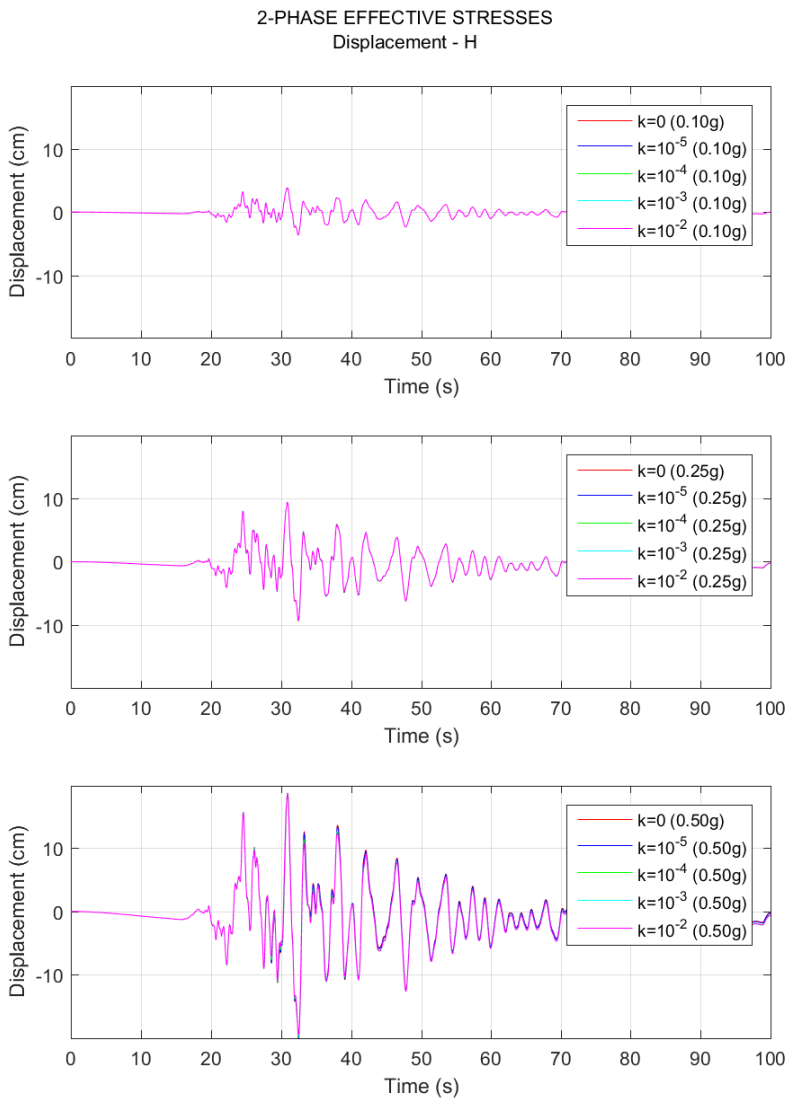

Fig. II–20. 2-Phase effective stresses – Displacement- H.

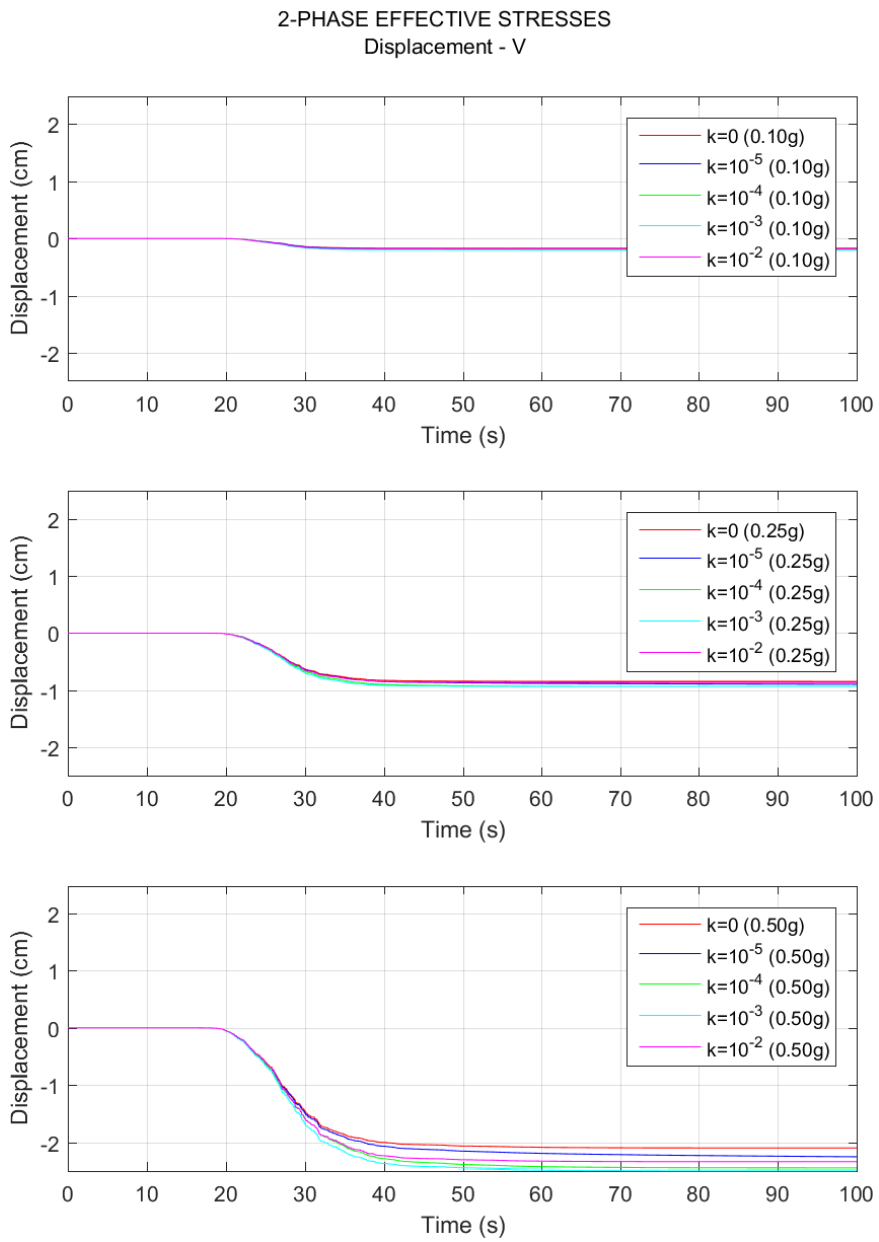

Fig. II–21. 2-Phase effective stresses – Displacement- V.

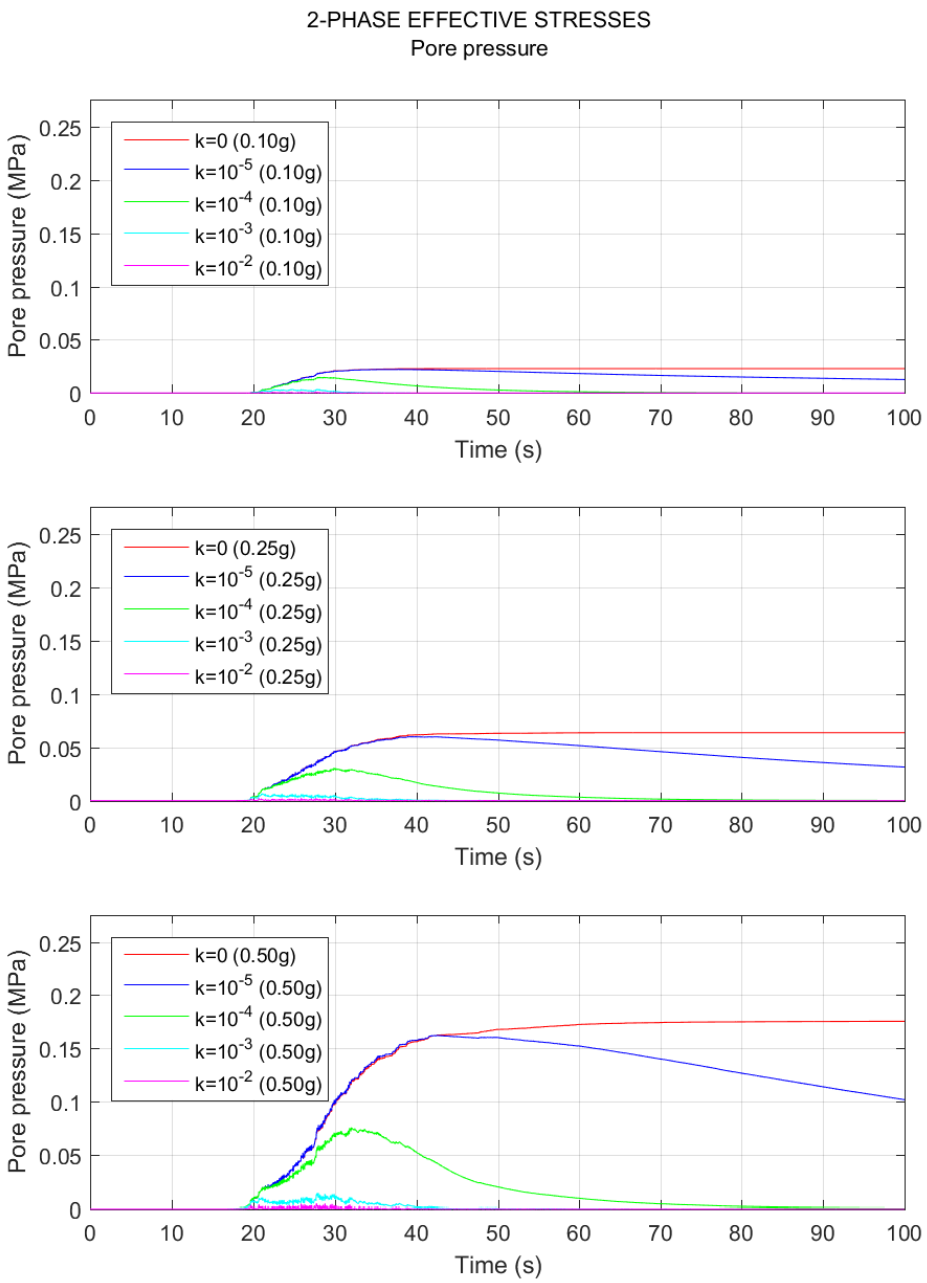

Fig. II–22. 2-Phase– Pore pressure.

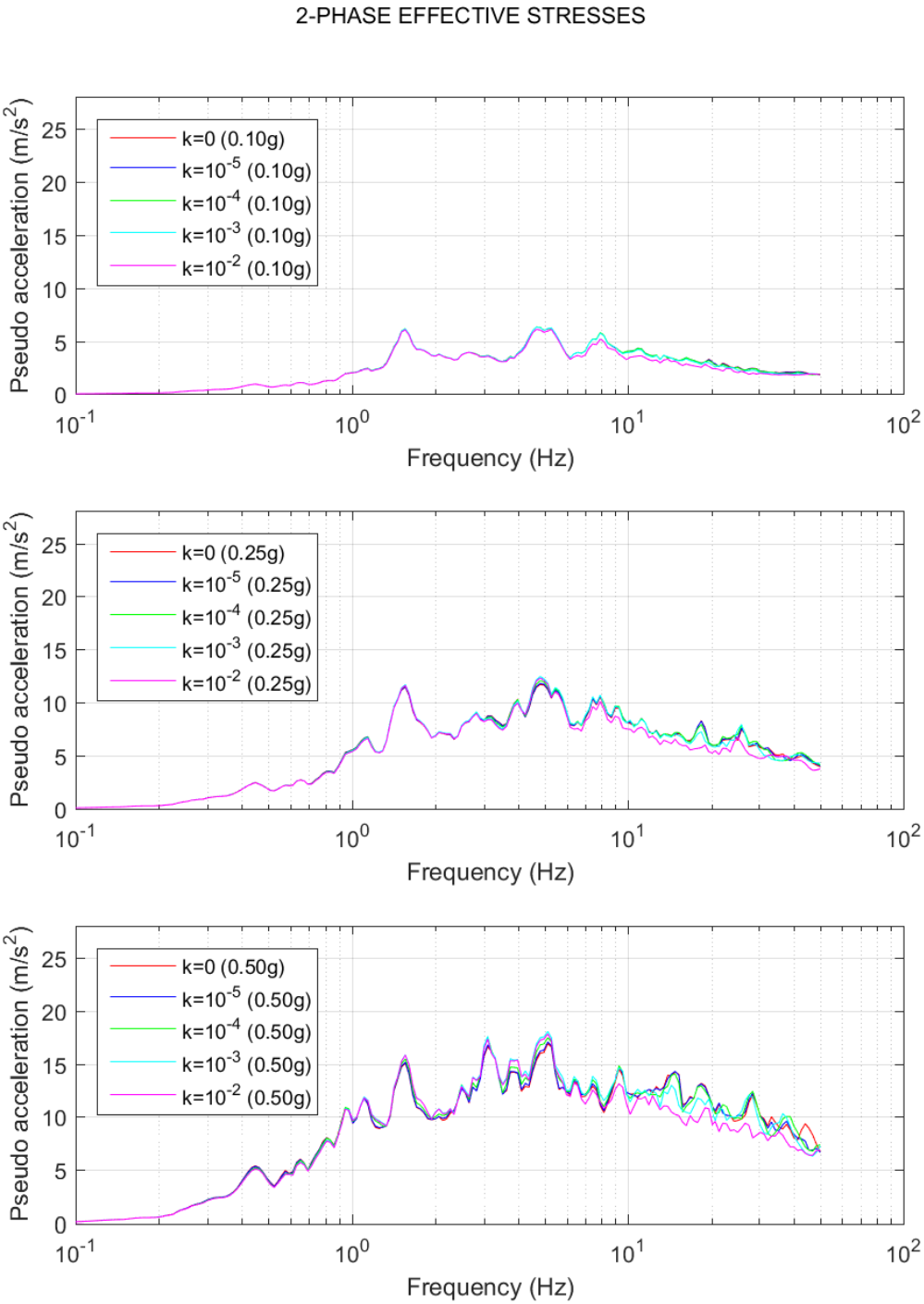

Fig. II–23. 2-Phase - Effective stresses.

II–8.5. Examples 5. Influence of vertical component (Cases 7a, 7b, 8a, 8b, 9 and 10)

Figure II–24 presents the results. Ground surface response spectra have been computed under various assumptions for the horizontal motion and the vertical motion. The two components of motion are input simultaneously in the model since the material behaviour is non-linear. From the calculated spectra V/H ratios have been computed and compared to Gülerce–Abrahamson prediction equation for a magnitude 6.39 event recorded at 15km from the source (Joyner–Boore distance). Results clear show that for frequencies less than 10Hz the vertical motion can be predicted assuming vertical propagation of P waves; however, for higher frequencies, as explained in main body of the TECDOC, the vertical motion cannot be assumed to be created only by the vertical propagation of P waves: Rayleigh waves, diffracted P–SV waves also contribute to the response.

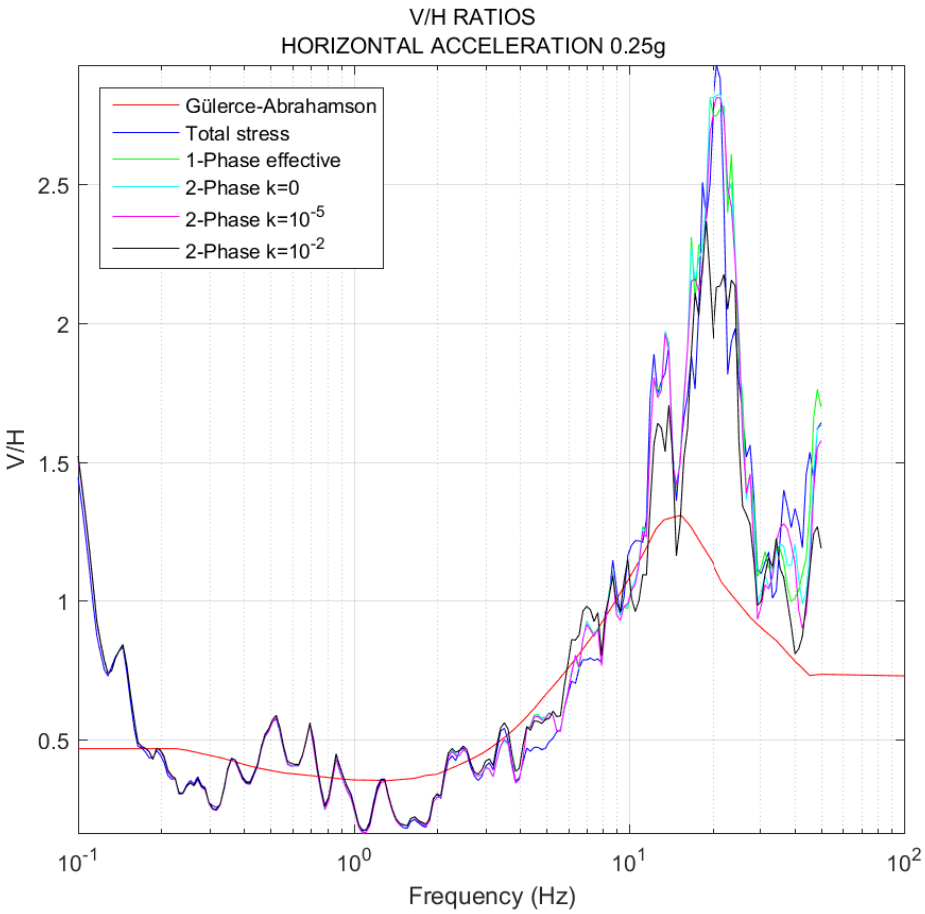

Fig. II–24. V/H Ratios – Horizontal acceleration 0.25g.

II–8.6. Example 6. Comparison of 1-D vs 2-D non-linear site response analyses

This example presents an outline of the importance of topographic effects. Motions are calculated at the location shown in the middle of the valley where a marked topography exists (Figure II–25). Calculations were made assuming:

(1) a 1-D model, extracted from the soil column at the examined location, and an EqL constitutive model,
(2) a 2-D model, including the whole valley shown in the top figure, with the strain compatible soil properties retrieved from the 1-D EqL analyses
(3) the same 2-D model as above but a fully NL constitutive model for the soil.

The calculated surface spectra clearly indicate that the 1-D model is unable to correctly predict except for long periods, above 1.5s (Figure II–26). The main difference between the spectra arise from the geometric model rather than from the constitutive model, although the 2-D linear model should be regarded with caution because damping is modelled as Rayleigh damping, while in the two other analyses, frequency independent damping is considered.

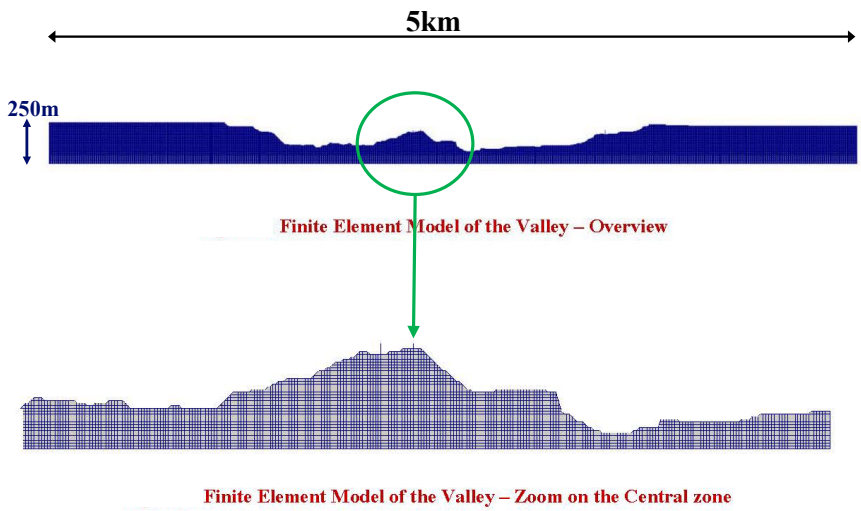

Fig. II –25. Finite element model of the valley.

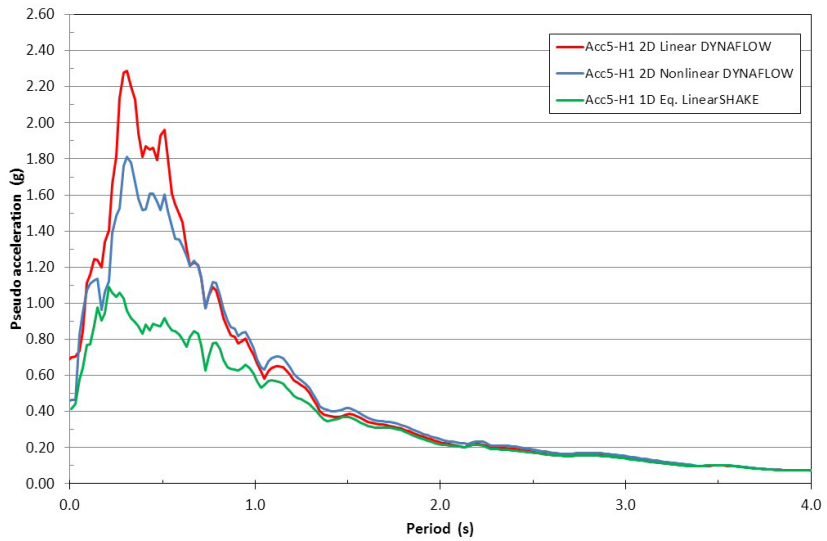

Fig. II–26. Surface response spectra.

II–8.7. Example 7. Influence of damping in linear elastic site response analyses

This example presents the sensitivity of the soil damping to the modelling assumption when damping is very low.

The "soil" column is composed of one layer of elastic rock material (2km thick with Vs = 2000m/s) overlying a half-space with Vs = 3000m/s. It is subjected to a real hard rock records recorded in Canada with a duration of 60s and a maximum acceleration equal to 0.03g; although the PGA is very small it has not been scaled up since all calculations presented in this example are linear. The record, its 5% damped response spectrum and its Fourier amplitude spectrum are shown in Figures II –27, II–28 and II–29, respectively.

Several methods were used for the calculations and the results are shown (Figure II–30) as 5% damped ground surface response spectra:

- Pure elastic calculation. A time domain solution with Dynaflow and two meshes: one with ten elements per wave length (element size 5m) and one with 20 elements per wave length (element size 2.5m). The differences were negligible and only the results with 10 elements per wave length are presented.
- Pure elastic calculation in the frequency domain using the exponential window method (EWM) developed by [II–17].
- 0.1% damping in the rock layer (the half-space is still undamped) with a frequency domain solution: classical FFT (SHAKE) and EWM.
- 1% damping in the rock layer (the half-space is still undamped) with a frequency domain solution: classical FFT (SHAKE) and EWM.
- Numerical damping in the time domain analysis with Dynaflow (Newmark's parameter equal 0.55 instead of 0.50).
- Rayleigh damping (stiffness proportional) in the time domain analysis calibrated to yield 1% damping at twice the fundamental frequency of the layer, i.e. 0.5Hz.

The main conclusions from the results are:

- For pure elastic calculation, either the time domain solution or the EWM should be used; the agreement is surprisingly good up to 25Hz. Above that value, they slightly differ but this may be due to filtering by the mesh in the time domain solution although when the number of elements per wave length is doubled the results do not change.
- For very lightly damped systems (0.1%), there is only one reliable method, the EWM; damping cannot be controlled in the time domain solution and the classical FFT overdamps the frequencies above 8Hz (in this case).
- For lightly damped systems (1%), the classical FFT and the EWM perform equally well. However, the EWM is much faster and does not need trailing zeroes to be added to the input motion; the duration of this quiet zone might be a cause of errors in FFT calculations if not properly chosen.
- Rayleigh damping is not to be used for damped systems in time domain analyses. It might even be better to rely on numerical damping, but the exact implied damping is not known.
- It is impossible to know what the exact amount of damping in very stiff rock is (0%, 0.1%, 1%) and the results are very sensitive to this choice above 1Hz.

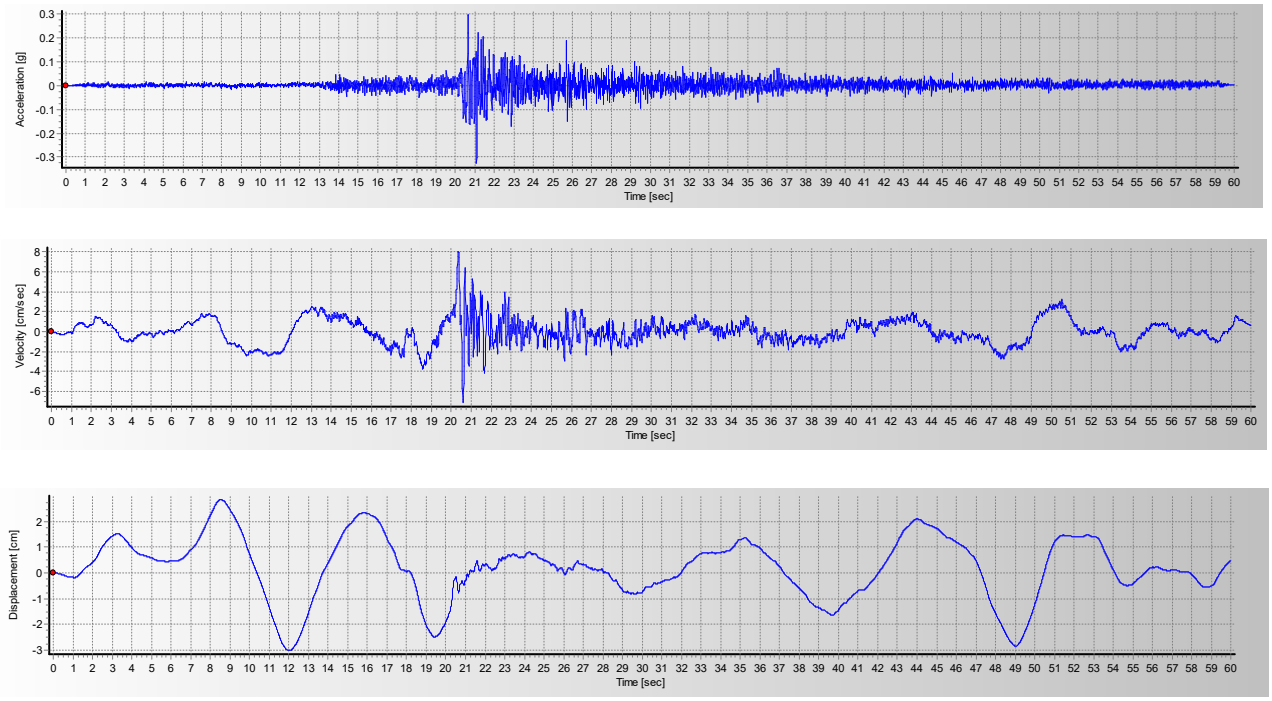

Fig. II –27. Record OT012-HNG with a duration of 60s and a maximum acceleration equal to 0.03g - Acceleration, velocity, and displacement.

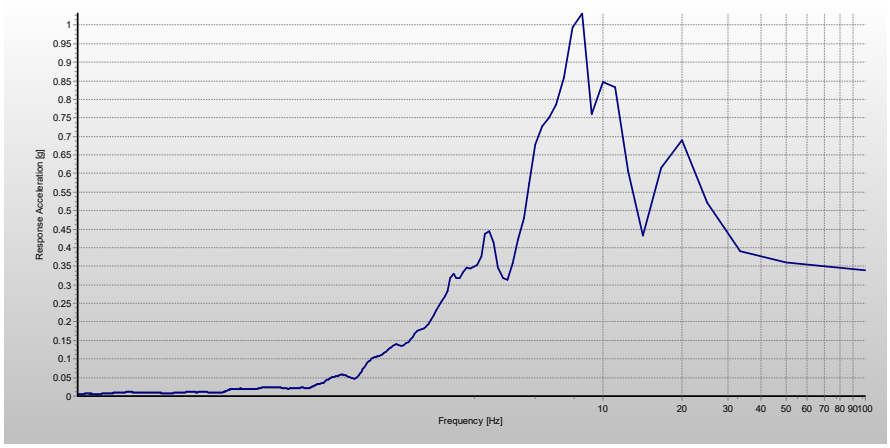

Fig. II –28. Response spectrum.

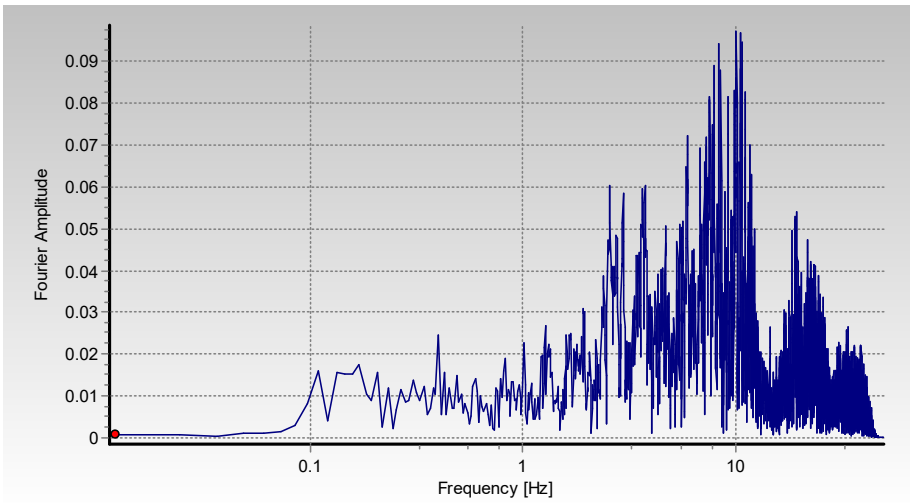

Fig. II–29. Fourier amplitude spectrum.

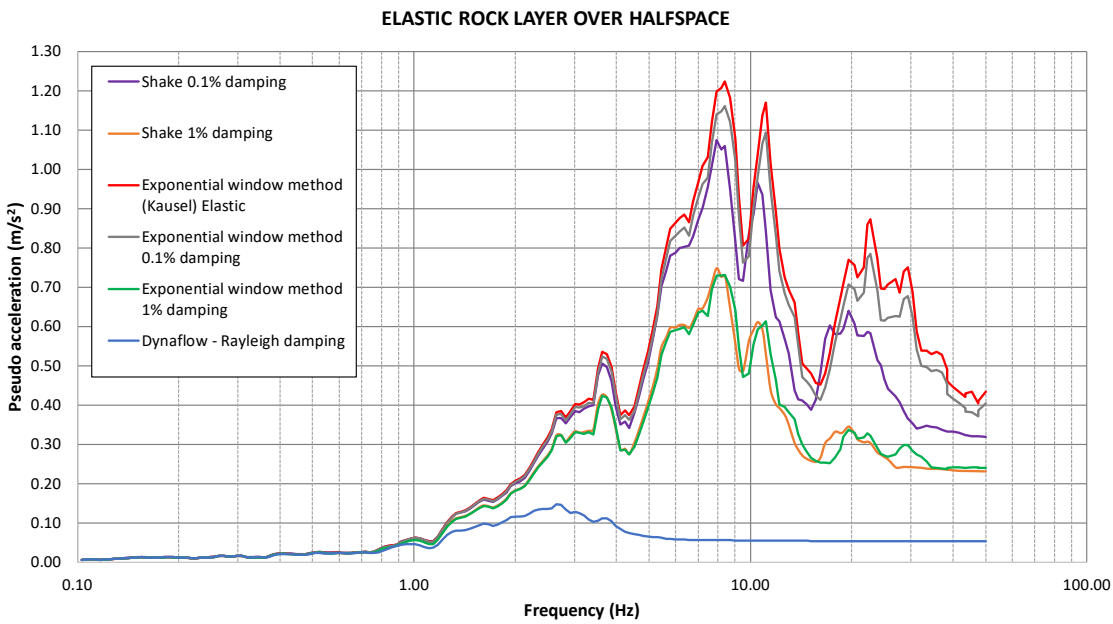

Fig. II–30. Response spectrum.

REFERENCES TO ANNEX II

[II–1] PREVOST J. H., Mechanics of continuous porous media. International Journal of Engineering Sciences, Vol 18 (1980).

[II–2] COUSSY, O., Mechanics of Continuous Porous Media. John Wiley (1995).

[II–3] PREVOST, J.H., Anisotropic undrained stress strain behaviour of clays - Journal of Geotechnical Engineering Division, Vol. 104, No GT8 (1978).

[II–4] PREVOST, J.H., A simple plasticity theory for frictional cohesionless soils - Soil Dynamics and Earthquake Engineering, Vol. 4, No 1 (1985).

[II–5] POPESCU, R., PREVOST, J. H., Centrifuge Validation of a Numerical Model for Dynamic Soil Liquefaction, Soil Dyn. and Earth. Eng., Vol. 12 (1993).

[II–6] PREVOST J.H., DYNAFLOW - A finite element analysis program for the static and transient response of linear and nonlinear two and three-dimensional systems - Department of Civil Engineering - Princeton University - Version 2002, Release 08-A (2008).

[II–7] IWAN, W.D., On a class of models for the yielding behaviour of continuous and composite systems - Journal of Applied Mechanics, ASME, Vol. 34, No E3 (1967).

[II–8] MROZ, A., On the description of anisotropic work hardening. Journal Mech. Phys. Solids (1967).

[II–9] SIMO, J. C., ORTIZ, M., A unified approach to finite deformation elastoplastic analysis based on the use of hyperelastic constitutive equations. Comp. Meth. Appl. Mech. Eng. (1985).

[II–10] PREVOST, J. H., DYNA1D - A computer program for nonlinear seismic site response analysis; Technical documentation NCEER-89-0025. Technical report, Dept. of Civil Eng. and Op. Research, Princeton University (1989).

[II–11] PREVOST, J. H., Nonlinear dynamic response analysis of soil and soil-structure interacting systems. In Proc. Seminar Soil Dyn. Geotech. Earthq. Eng., Lisboa, Portugal. Balkema, Rotterdam (1993).

[II–12] GRIFFITHS, D. V., PREVOST, J. H., Stress-strain curve generation from simple triaxial parameters. Num. Analyt. Meth. Geomech (1990).

[II–13] HAYASHI, H., HONDA, M., YAMADA, T., Modelling of nonlinear stress strain relations of sands for dynamic response analysis. In Proc. 10th World Conference on Earthquake Eng., Madrid, Spain - Balkema, Rotterdam (1992).

[II–14] Hughes, T.J.R., Analysis of transient algorithms with particular reference to stability behaviour. Computational Methods for Transient Analysis. Elsevier (1983).

[II–15] GÜLERCE, Z., ABRAHAMSON, N.A., Site-Specific design spectra for vertical ground motion, Earthquake Spectra, Vol. 27, No4 (2011).

[II–16] NUREG/CR-6728, Technical basis for revision of regulatory guidance on design ground motions: Hazard -Risk-Consistent ground motion spectra guidelines (2001).

[II–17] KAUSEL, E., Advanced Structural Dynamics, Cambridge University Press (2017).

Annex III

ANALYSIS OF A PILE FOUNDATION (FOR A BRIDGE) BY THE SUBSTRUCTURE METHOD

This example was developed to illustrate the various steps involved in the determination of the seismic forces developed in piles during earthquake shaking. The example is developed within the framework of the substructure approach explained in Section 9.3.3.1. The flow chart in Fig. III–1 summarizes the steps that need to be taken before arriving at the pile internal forces. Only the steps identified with a number in brackets are detailed below.

The pile foundation is composed of 35 concrete, cast in–place piles, 2.5m in diameter and 50m long. The pile cap is embedded in the soil along its height, but it is assumed that its base (pile heads) is at the ground surface.

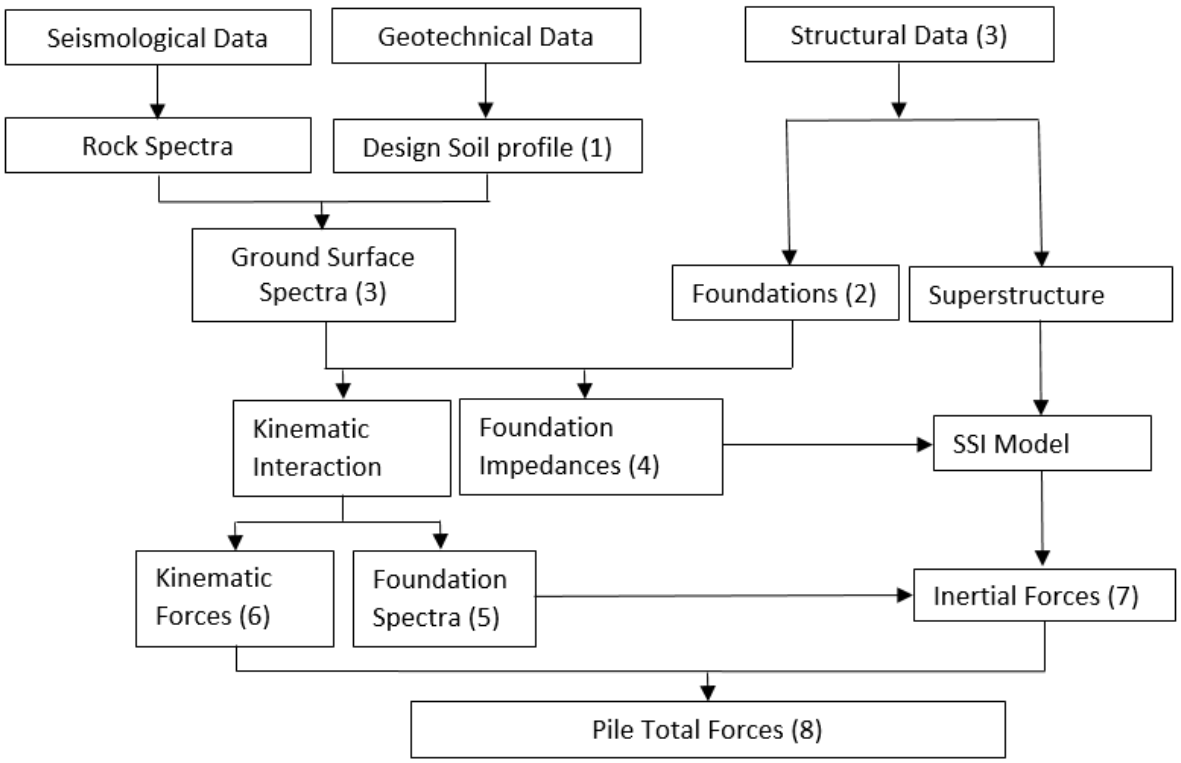

Fig. III–1. Steps for the pile internal forces.

III–1. DESIGN SOIL PROFILE – STEP (1)

The strain compatible characteristics are obtained from a free field 1-D site response analysis (step (3)) carried out with the EqL model. Figure III–2 presents wave velocity profiles.

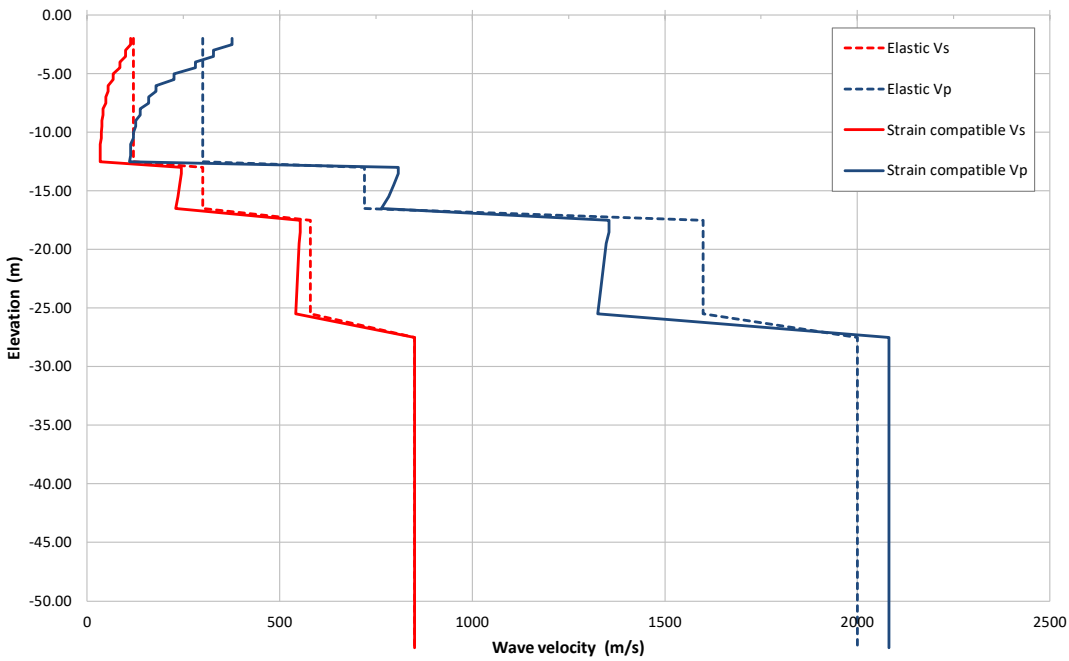

Fig. III–2. Wave velocity.

III–2. FOUNDATION MODEL – STEP (2)

Figure III–3 presents the foundation model.

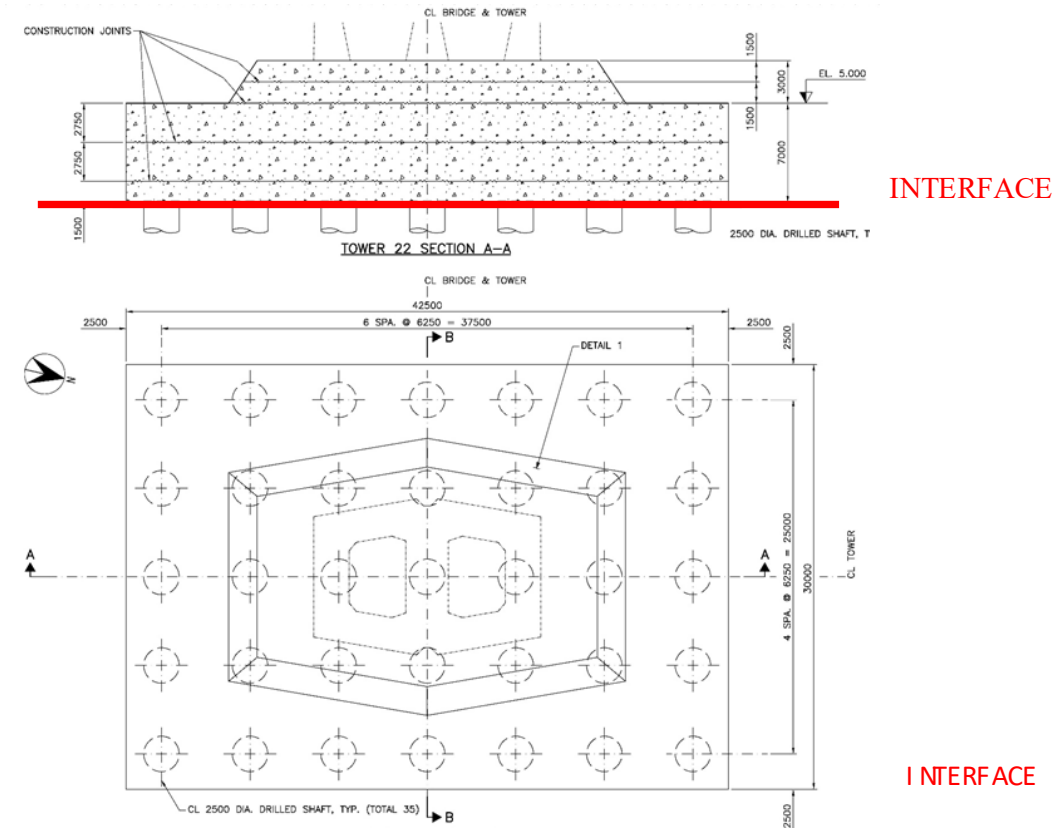

Fig. III–3. Foundation model.

III–3. FREE FIELD RESPONSE SPECTRA – STEP (3)

Figures III–4 and III–5 present shear wave velocity profile and free field response spectra, respectively.

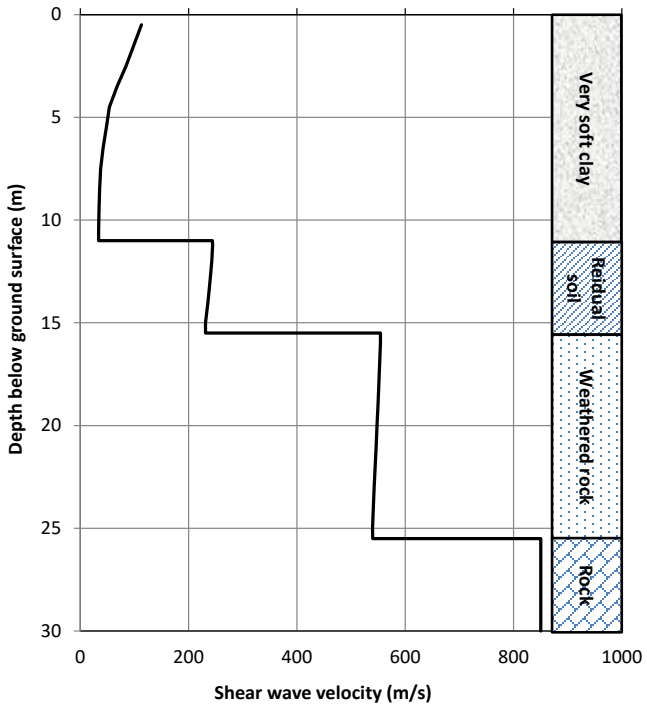

Fig. III–4. Shear wave velocity profile.

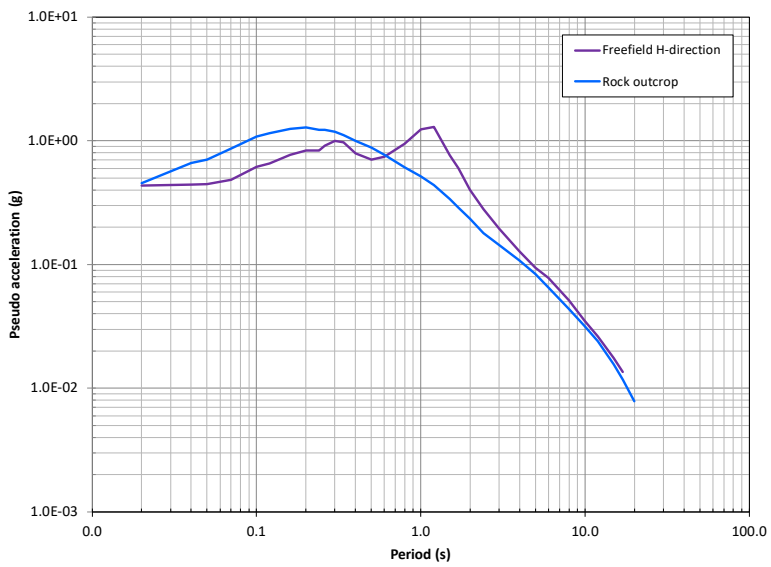

Fig. III–5. Free field response spectra.

III–4. FOUNDATION IMPEDANCE – STEP (4)

The foundation model (flexural/shear beams for the piles, rigid massless beams connecting the piles heads (modelling the kinematic conditions imposed by the pile cap)) is presented in Figure III–6. The nodes of the pile cap are not connected to the soil layer (gap between the pile cap and the soil). Soil layers, not represented in Figure III–6, are modelled as horizontal homogeneous strata with strain compatible properties retrieved from the site response analyses.

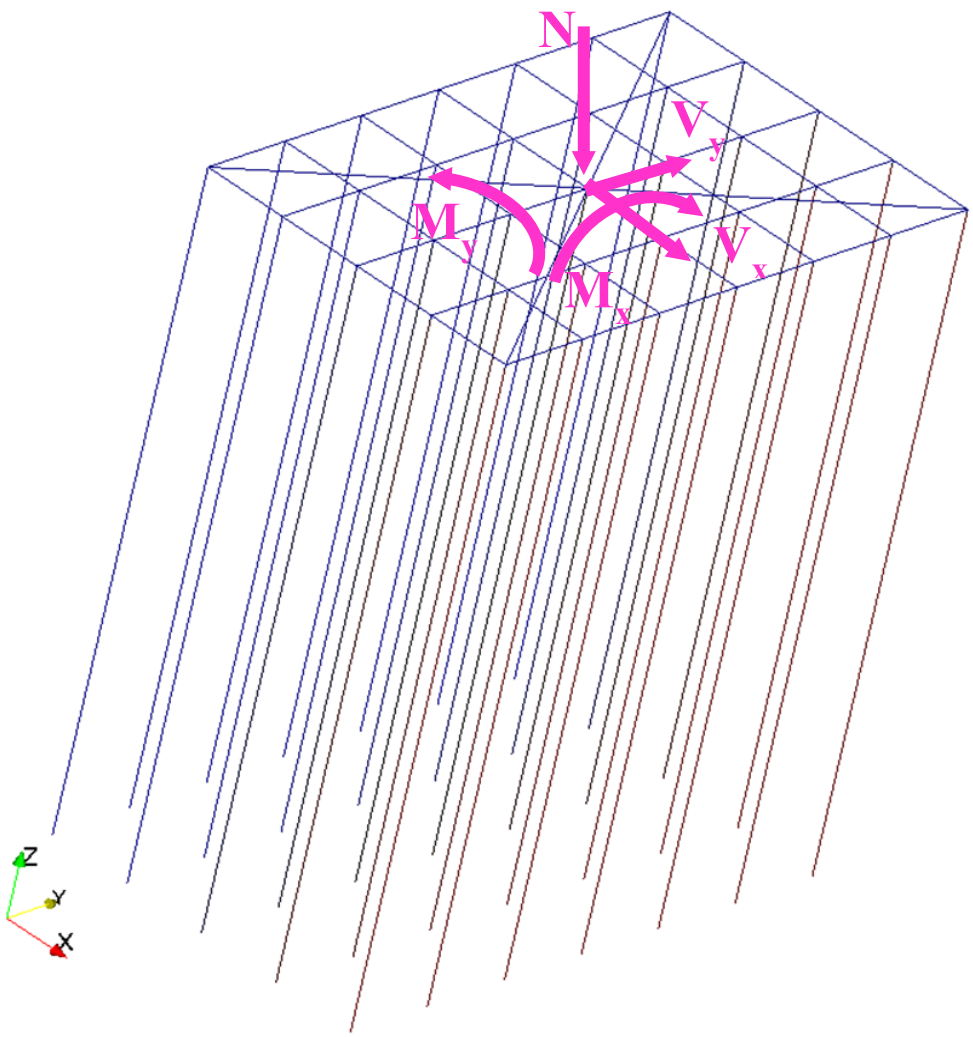

Fig. III–6. Foundation model.

The frequency dependent impedance terms are shown in Figs III–7–III–11 for all degrees of freedom, including the coupled sway-rocking terms. The real part, imaginary part and equivalent damping ratio (including both material and radiation damping) are shown.

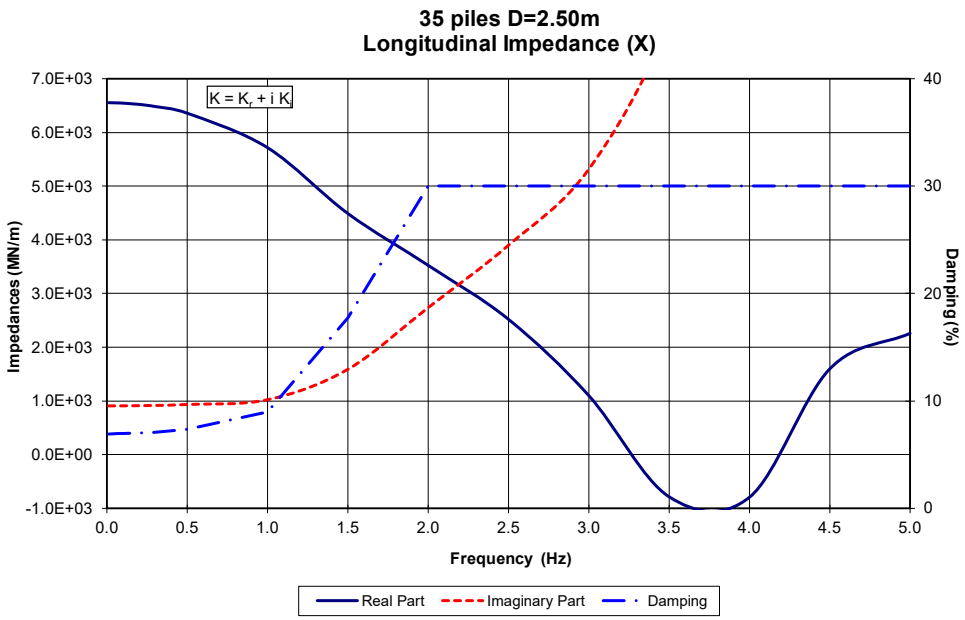

Fig. III–7. Longitudinal impedance.

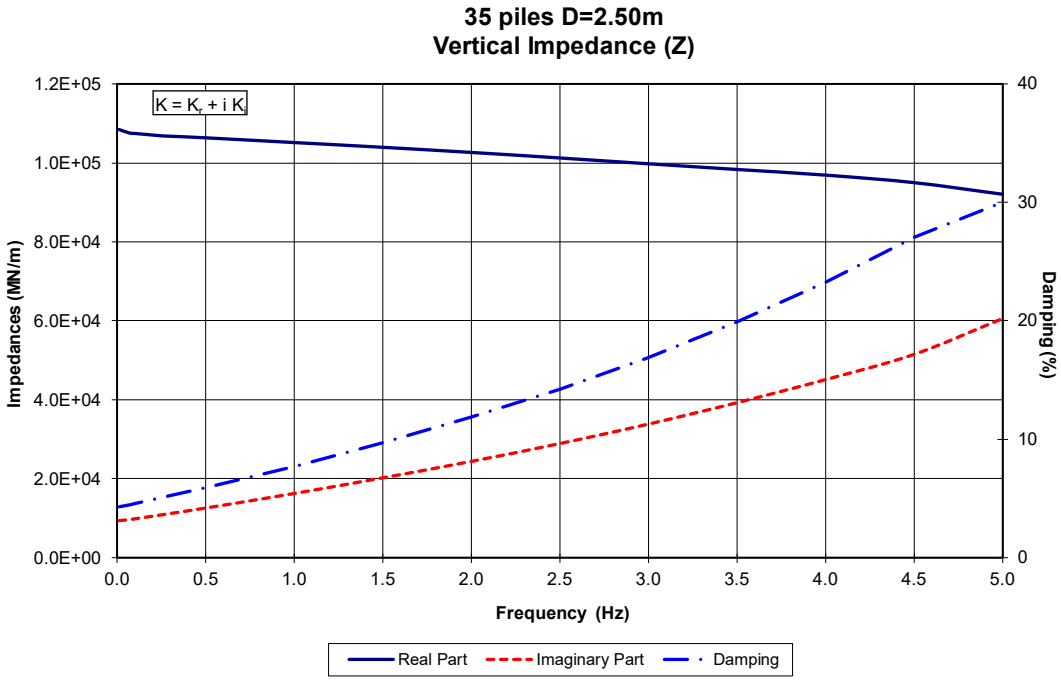

Fig. III–8. Vertical impedance.

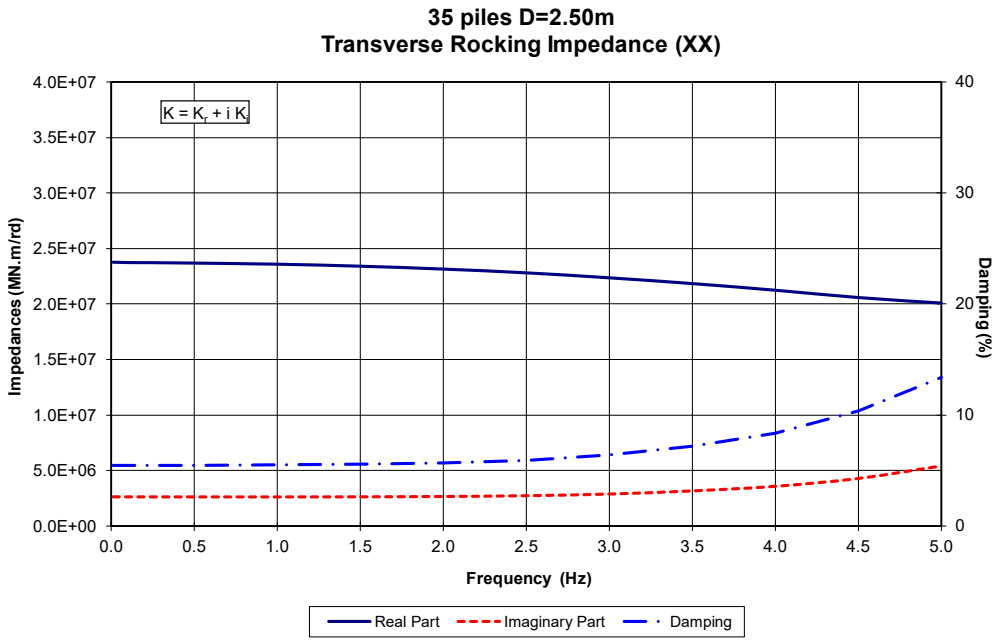

Fig. III–9. Transverse rocking impedance.

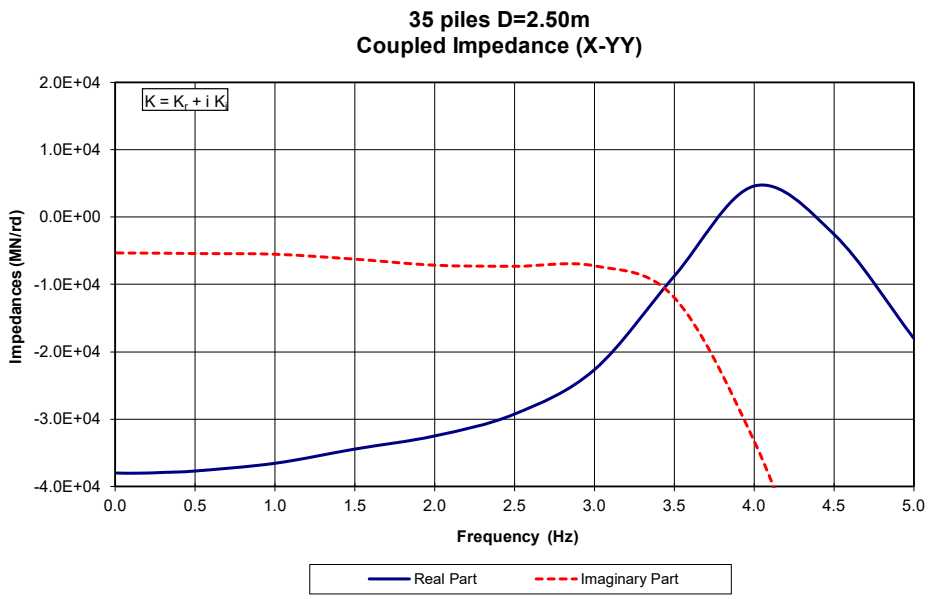

Fig. III–10. Coupled impedance.

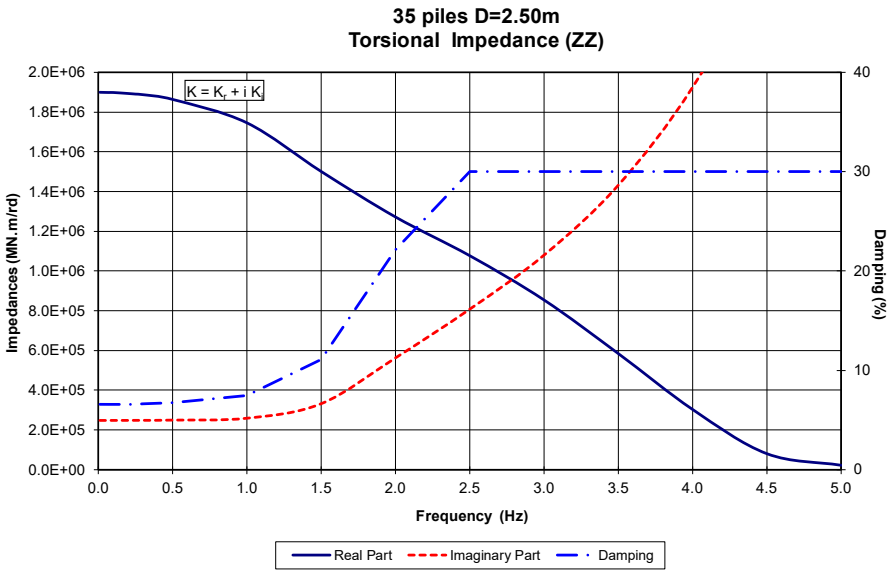

Fig. III–11. Torsional impedance.

III–4.1. Isolated pile

To illustrate the importance of the group effect, the longitudinal impedance of an isolated pile is shown in Figure III–12. Note that the impedance (real part) is almost frequency independent as opposed to the same term for the pile group because of the absence of scattering by the adjacent piles.

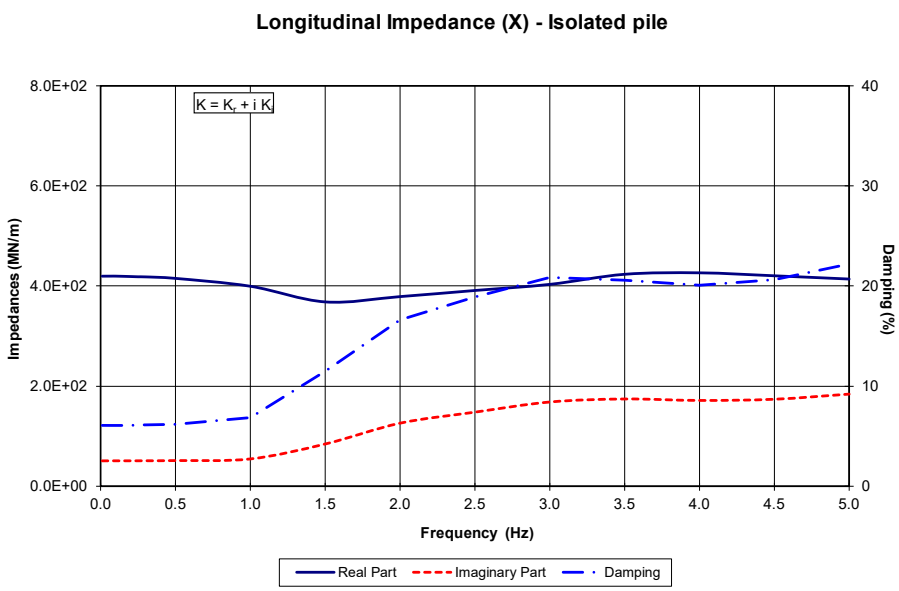

Fig. III–12. Longitudinal impedance – Isolated pile.

The group effect is calculated for both the longitudinal and vertical impedance (see Figure III–13). This group effect is significant (2.6 for the longitudinal impedance and

1.7 for the vertical one) and more important is frequency dependent for the longitudinal term. For the vertical one, it is almost frequency independent because the piles are anchored in a competent layer. The negative group effect for the horizontal impedance above 3.2Hz is caused by the scattering effect by adjacent piles in the pile group.

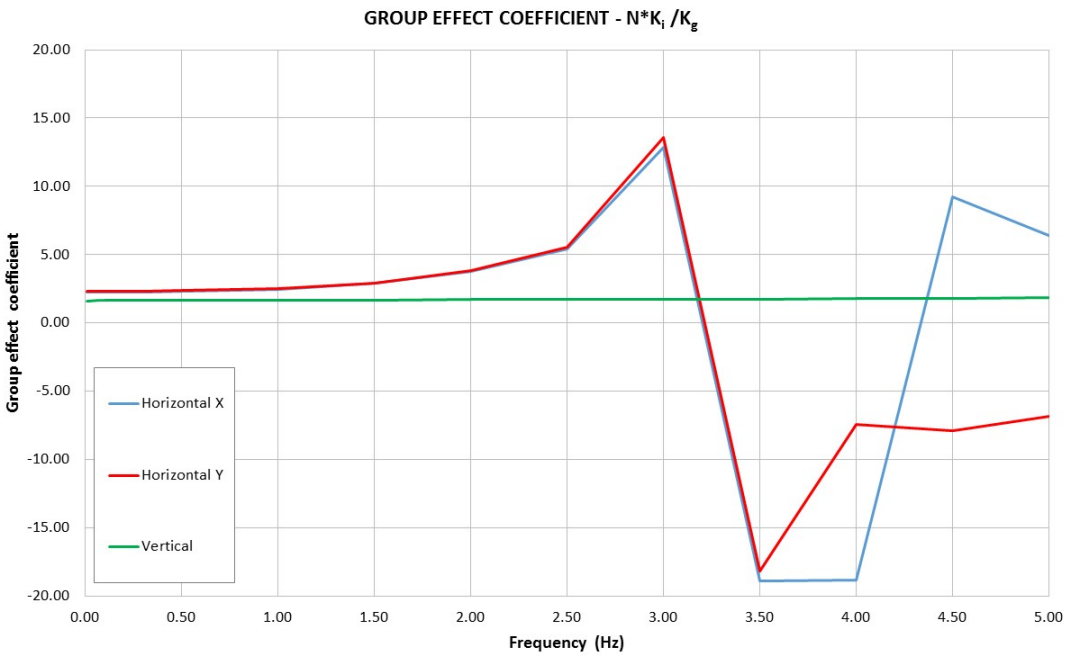

Fig. III–13. The group effect for longitudinal and vertical impedance.

III–5. FOUNDATION RESPONSE SPECTRA – STEP (5)

The foundation response spectra are different from the free field response spectra and may be higher or lower depending on the frequency range. Although the piles are anchored in a competent layer and are rather stiff (2.5m in diameter) the foundation spectra are also different from the rock spectrum. This is an example in which kinematic interaction cannot be neglected and a rigorous application of the substructure method necessitates that the structure be subjected to the true kinematic motion. Figure III–15, related to another foundation of the same structure located in a stiffer soil profile (same as above but without the very soft clay layer at the top) and with smaller piles diameters (1.80m instead of 2.5m), shows that in this case directly using the free field motion (still different from the rock motion at high frequencies) may be acceptable from a practical point of view. The latter case makes the application of the substructure method easier to implement because foundation motions do not need to be computed.

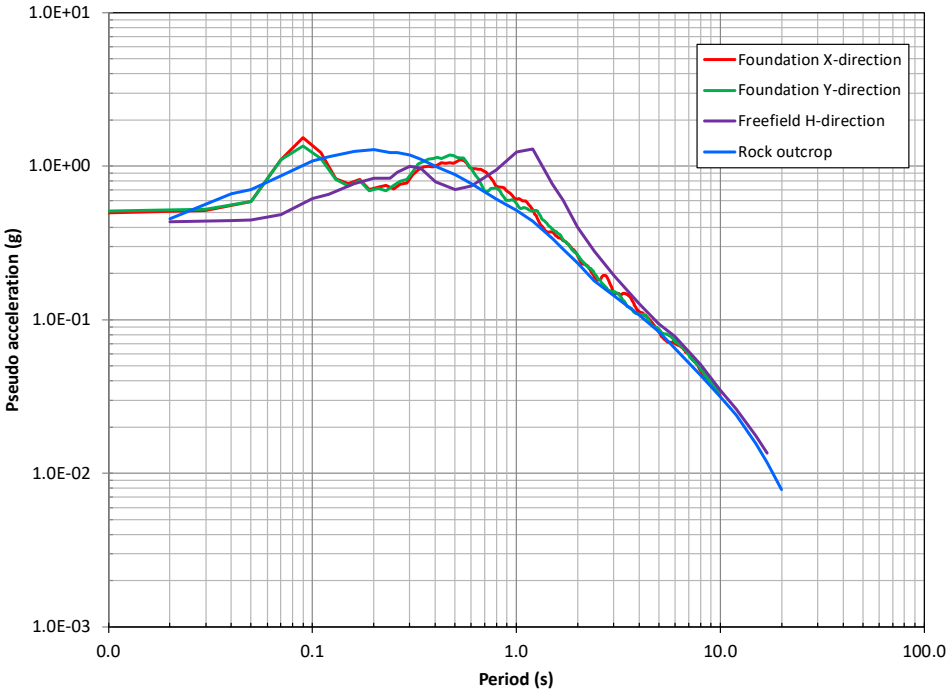

Fig. III–14. Comparison of response spectra.

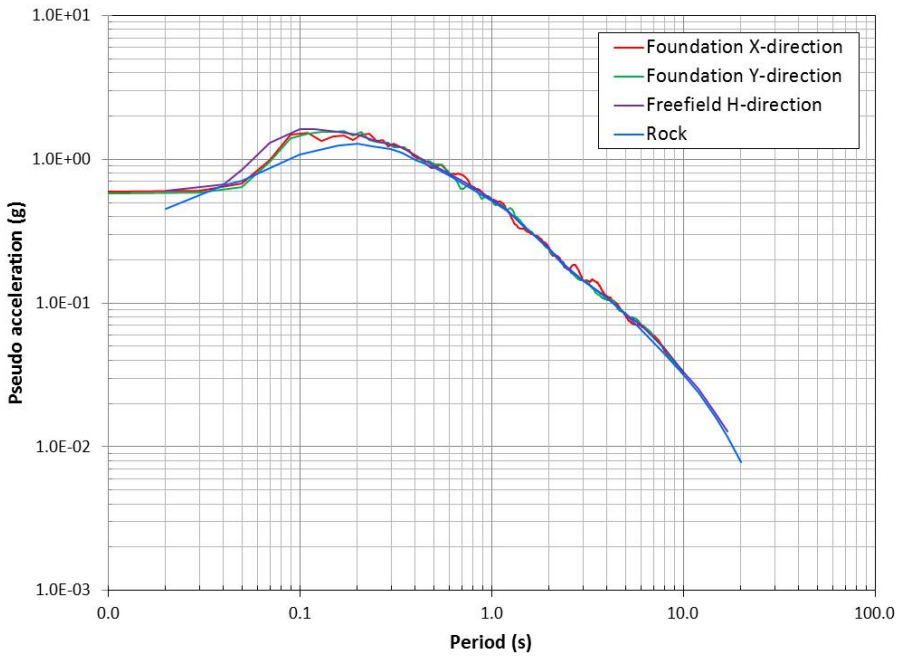

Fig. III–15. Comparison of response spectra for the foundation of the same structure located in a stiffer soil profile and with smaller piles diameters.

III–6. KINEMATIC FORCES – STEP (6)

Calculations are made for seven different time histories and Figures III–16 and III–17 show the maximum (regardless of the time at which they occur) bending moments and shear forces. The significant bending moment at 16m depth is caused by the strong stiffness contrast between the top soil layers and the weathered rock layer. The difference between the corner pile and the centre pile is rather limited because of the large number of piles. This difference would even be smaller if non-linearities were considered in the soil–pile interface, with redistribution from the corner pile, more loaded, to the centre piles

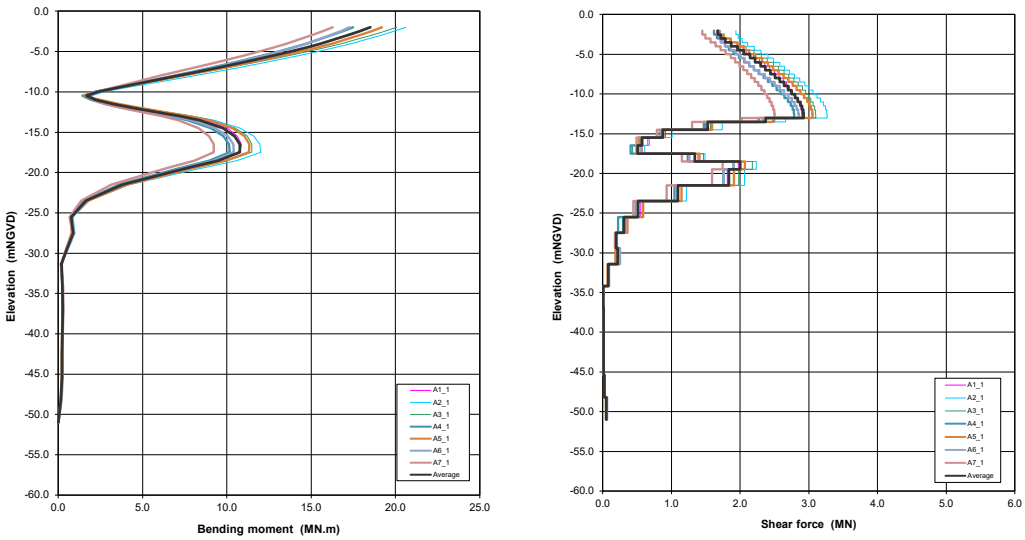

Fig. III–16. Maximum bending moments and shear forces for the centre pile.

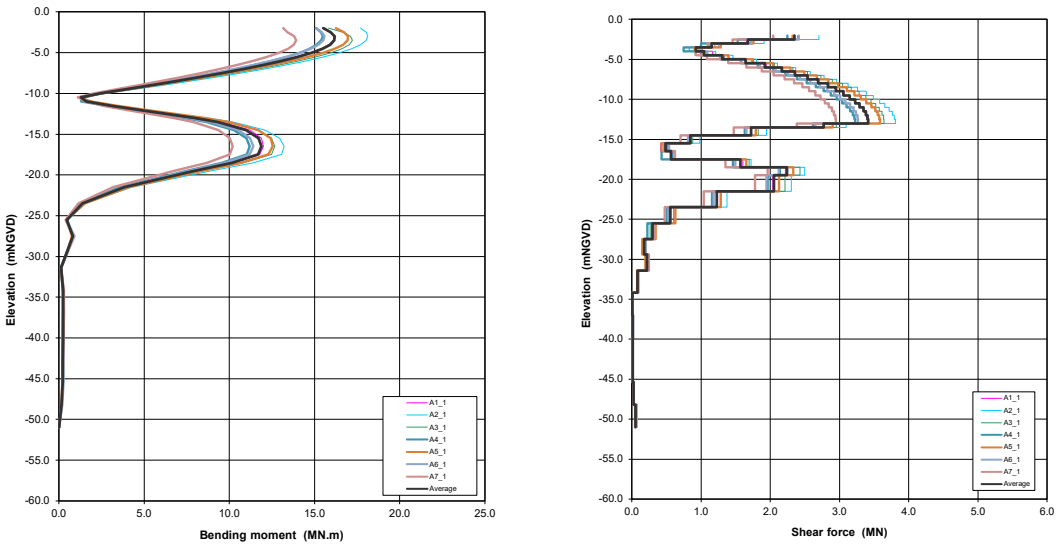

Fig. III–17. Maximum bending moments and shear forces for the corner pile.

III–6.1. Isolated pile

The kinematic forces have also been computed for an isolated fixed head pile. The internal forces, although similar in shape, are higher than for a pile in the group (note the different scales in Figure III–18) probably because the global rotation of the pile cap, although minimal, tends to release the pile head bending moment and shear force (see Figure III–18).

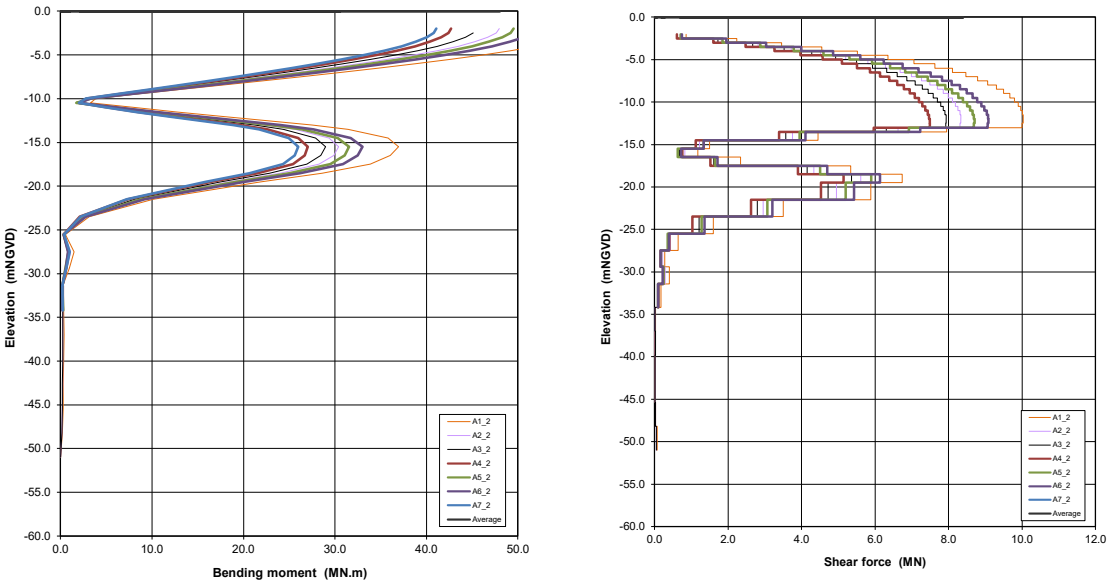

Fig. III–18. Maximum bending moments and shear forces for an isolated fixed head pile.

III–7. DETERMINATION OF INERTIAL FORCES IN PILES – STEP **(7)**

At the end of the SSI analysis, the global pile head forces are equal to the forces developed in the impedance functions and the pile cap displacements are known. Since the impedances represent the pile group impedance, the first step is to distribute the global forces (forces and moments) among the piles; this can be done for instance with the foundation model used for the calculation of impedances by applying the global forces, or displacements and rotations, at the node where the impedances are computed. Ideally, the forces (or displacements) are applied at a frequency corresponding to the fundamental frequency of the SSI mode. This procedure will not only yield the forces at each pile head but also the internal forces along each pile height.

However, this procedure assumes that the soil remains linear along the pile–soil interface with the strain compatible properties computed from the site response analysis. It therefore neglects additional, local, non-linearities that can take place along the pile shaft due to stress concentration. If these additional non-linearities are of minor importance on the global response, they may strongly affect the distribution of forces

in piles. It is therefore preferable to model each pile as a beam on a Winkler foundation, with the springs, dashpots and sliders modelling the pile–soil interaction calculated from available results (p–y curves from API–RP2A or Fascicule 62 –Titre V – CCTG,//www.geotech-fr.org › projets › pieuxbois). An example of such a model is shown in Figure III–19; it is submitted to the pile head forces calculated from the SSI analysis and distributed across the pile group.

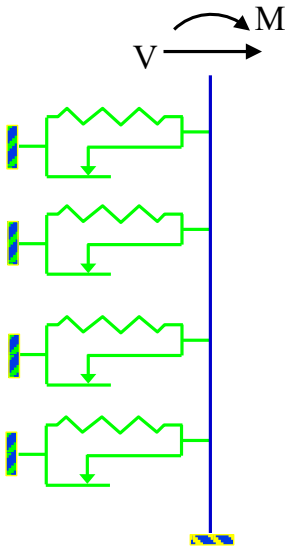

Fig. III–19. Pile model as a beam on a Winkler foundation, with the springs, dashpots and sliders.

III–8. COMBINATION OF INERTIAL AND KINEMATIC FORCES IN PILES – STEP (8)

If the piles kinematic forces F_K and the piles inertial forces F_I are obtained from time history analyses, there is no difficulty in combining at each time step their contributions. The total force at any given elevation and at any time is given by:

$$F_T(z,t) = \pm F_I(z,t) \pm F_K(z,t) \qquad \text{(III–1)}$$

However, in most cases if the kinematic forces are known as a function of time, only the maximum inertia forces are retrieved from the SSI analyses (for instance when a modal spectral analysis is used). To combine both components, each of them should be alternatively considered as the main action and weighted with a factor 1.0, while the other one is the accompanying action and weighted with a factor λ:

$$F_T(z) = \pm \max_t F_I(z,t) \pm \lambda \max_t F_K(z,t) \qquad \text{(III–2)}$$

or

$$F_T(z) = \pm \lambda \max_t F_I(z,t) \pm \max_t F_K(z,t) \qquad \text{(III–3)}$$

The coefficient λ depends on how close the main frequency leading to the maximum kinematic forces is to the main frequency leading to the maximum inertia forces. The first one is controlled by the soil response (fundamental frequency of the soil column) and the second one by the SSI mode. If these two frequencies are well separated, let's say by 20%, both maxima are uncorrelated in time and their maximum values can be added using the SRSS rule.

$$F_T(z) = \sqrt{\left|\max_t F_I(z,t)\right|^2 + \left|\max_t F_K(z,t)\right|^2} \qquad \text{(III–4)}$$

If both frequencies are within 20% of each other, it is reasonable to assume that both phenomena are correlated, and the kinematic and inertia forces should be added algebraically:

$$F_T(z) = \left|\max_t F_I(z,t)\right| + \left|\max_t F_K(z,t)\right| \qquad \text{(III–5)}$$

III−8.1. The influence of the contact condition between the pile cap and the soil

The previous calculations have been made assuming no contact between the pile cap and the soil. This assumption is very difficult to ascertain since the contact condition may evolve during the lifetime of the nuclear installation structure due to settlement of the soft layers caused by consolidation of clayey strata, or construction around the existing structure. It may also evolve during the earthquake due to soil compaction. Accurate modelling of this effect would require a full non-linear time domain analyses, which is still beyond the state of practice, especially with a large number of piles.

To estimate the impact of this modelling assumption, the impedance calculations have been redone with full contact between the pile cap and the soil.

The results are presented in Figure III–20 for one horizontal sway impedance, for the vertical one and for one rocking impedance as the ratio of the real part of the impedance term for the full contact condition to the same quantity for the no contact condition. The results show that the impact is negligible for vertical and rocking impedance, mainly because the piles tips are embedded in a competent layer and are only marginally important above 3Hz for the horizontal impedance, a frequency much likely to be higher than the SSI frequency of a heavy structure founded on piles. These conclusions apply to a pile group with a large number of piles and may be different when fewer piles are considered.

Given the insignificant difference between the two assumptions, for design purpose the no contact condition (which is the most likely situation) can be retained.

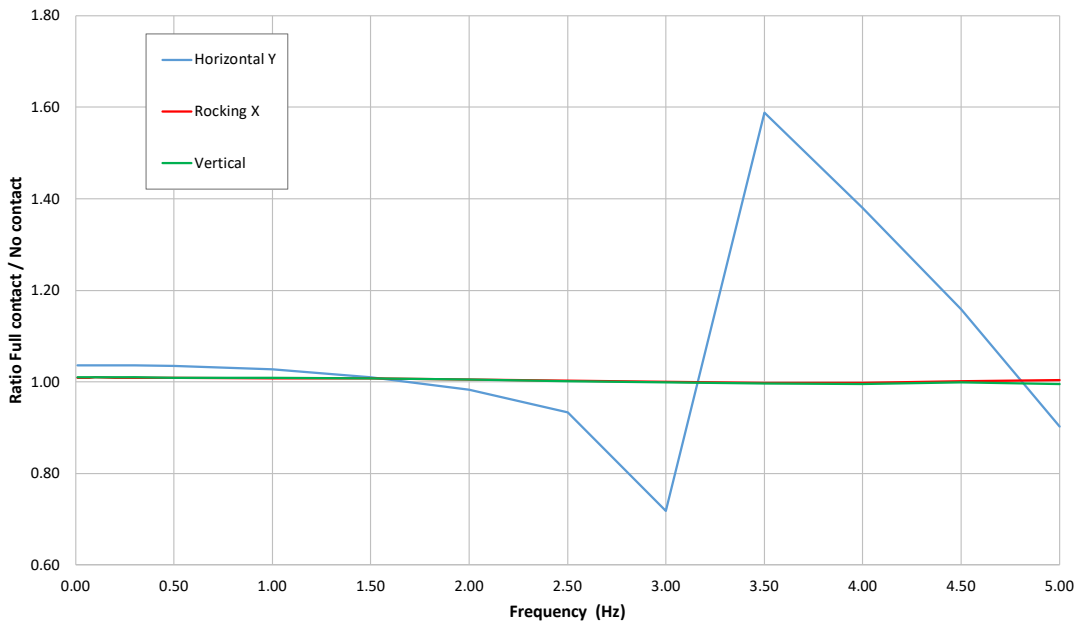

Fig. III–20. Influence of contact between the pile cap and the soil.

III–8.2. Influence of fixity condition at the pile cap

Previous calculations have been carried assuming a clamped connection of the piles to the pile cap. During seismic loading, the connection may deteriorate and evolve towards a reduction of the connection stiffness, eventually reaching the condition where a plastic hinge forms at the connection. Consideration of such phenomena requires a full non-linear dynamic analysis. To estimate the influence of such a degradation, the calculations have been redone with hinged conditions at the pile cap connection and no contact between the pile cap and the soil, which is an extreme condition. Figure III–21 presents the results which compare the dynamic impedances in both conditions: the fixity condition affects the horizontal stiffness but does not affect the vertical or rocking ones. However, the reduction in the horizontal stiffness, almost a factor of two, is certainly much larger than the reduction obtained under the formation of a plastic hinge which, in contrast to the hinged condition, exhibits a residual moment capacity.

Regarding the kinematic interaction forces (see Figure III–22 for the centre pile), if the maximum values are not significantly affected, the distribution of the forces along the pile is totally different: the maximum moment is now at -15m instead of being at the connection with the pile cap and the maximum shear force is deeper than before. One approach would be, for linear SSI analyses, either to run both types of analyses and to take the envelope of both conditions, or in a more conservative approach to take the maximum forces from the hinged analysis and to extend the maximum values upwards to the pile cap connection.

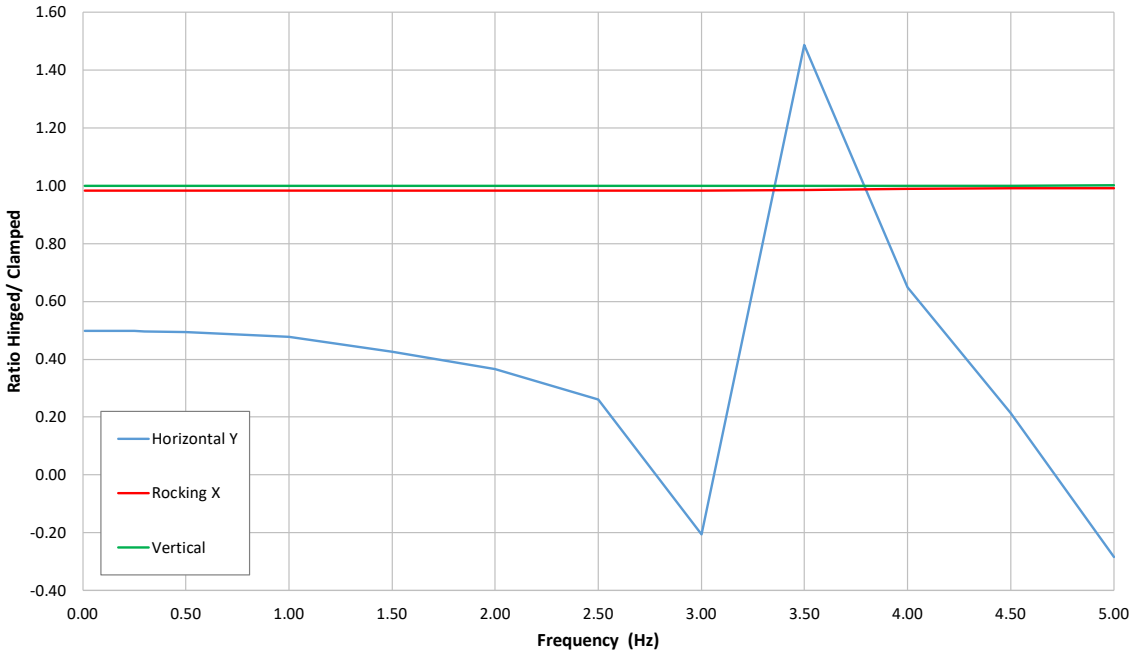

Fig. III–21. Influence of fixity condition at pile cap.

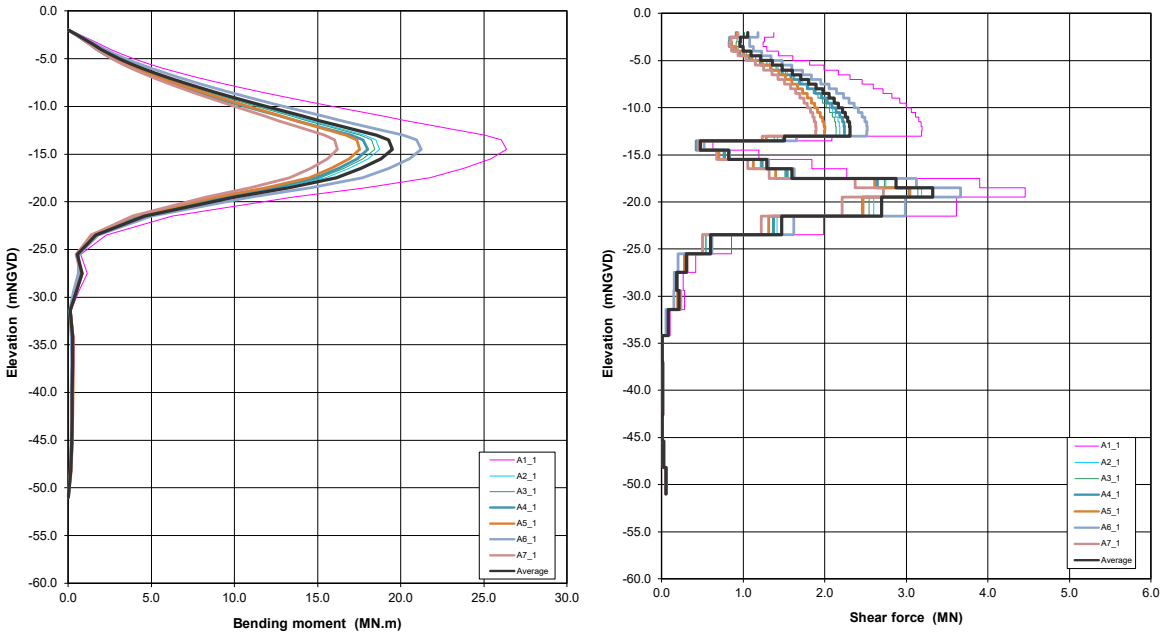

Fig. III–22. Bending moment and shear force for the centre pile.

Annex IV

EXAMPLES SEISMIC RESPONSE OF AN NPP ON NON-LINEAR SOIL AND CONTACT (SLIP AND UPLIFT)

This example presents the non-linear effects, namely response of soil and rock, and the contact zone (soil/rock-foundation) for non-linear response of an NPP.

IV–1. MODEL DEVELOPMENT AND SIMULATION DETAILS

The NPP model used here is a symmetrical structure with a shallow foundation slab (3.5m), and length of 100m. Figure IV–1 shows a slice view of the model in the normal y direction (perpendicular to plane of the paper). Solid brick elements are used for soil and foundation and shell elements for structure.

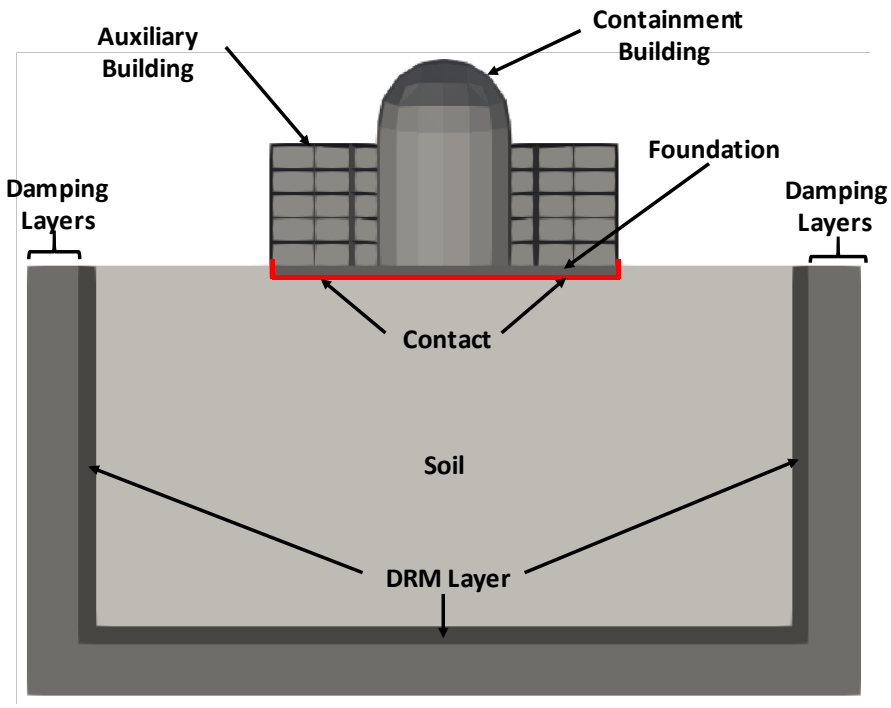

Fig. IV–1. Nuclear power plant model with shallow foundation.

IV–1.1. Soil Model

The depth of the model 120m below foundation (this is also the depth to the domain reduction method (DRM) layer). It is assumed that soils plastify within this range due to SSI effects. The soil is assumed to be dry, stiff with shear velocity of V_s = 500m/s, unit weight of γ = 21.4kN/m^3 and a Poison's ratio of ν = 0.25. To represent the travelling wave accurately for a given frequency, about 10 nodes per wavelength i.e. about 10 linear or 3 quadratic brick elements are needed [IV–1]. Here, the seismic waves are

analysed up to the frequency of f_{max} = 10Hz. The smallest wavelength λ_{min} to be captured thus, can be estimated as:

$$\lambda_{min} = V_s/f_{max} \qquad \text{(IV–1)}$$

Where, V_s is the smallest shear wave velocity of interest. For V_s = 500m/s and f_{max} = 10Hz the minimum wavelength λ_{min} becomes $(500m/s)/(10/s)$ = 50m. Choosing 10 nodes/elements per wavelength (linear displacement interpolation elements) the element size would be 5m [IV–2]. Reference [IV–1] states that even by choosing mesh size $\Delta h = \lambda_{min}/10$, the smallest wavelength that can be captured with confidence is $\lambda = 2\Delta h$, i.e. a frequency corresponding to $5f_{max}$. Based on the above analysis, soil was modelled as 8-node brick elements (with linear displacement interpolation, and non-linear/inelastic material) with a grid spacing of Δh = 5m.

A number of more or less sophisticated models for soils have been developed over years [IV–3–IV–6]. Here, only two scenarios of soil properties were considered in the analysis: one linear elastic and the other as von-Mises with non-linear kinematic hardening of the Armstrong-Frederick type with a yield strength achieved at a 1% shear strain and an initial kinematic hardening rate (h_a) of 3 x 10^5 kPa.

IV–1.2. Structural Model

The NPP structure consists of auxiliary building, containment building, and the foundation as shown in Figures IV–1 and IV–2 [IV–7]. The auxiliary building consists of 4 floors of 0.6m thickness, ceiling floor of 1m thickness, exterior wall of 1.6m thickness and interior walls of 0.4m thickness. The exterior and interior walls are embedded down to the depth of the foundation. The containment building is a cylinder of diameter 20m and height 40m with wall thickness of 1.6m. There is a gap of 0.2m between the containment and auxiliary building.

The top of the containment building is covered by semi-spherical dome of radius 20m. The foundation is square shallow footing of size 100m and thickness 3.5m. The containment building and the auxiliary building were modelled as shell elements and the foundation as 8 node-brick elements, both having the properties of concrete of elastic Young's modulus E = 20GPa, Poison's ratio ν = 0.21 and density ρ = 2400kg/m^3.

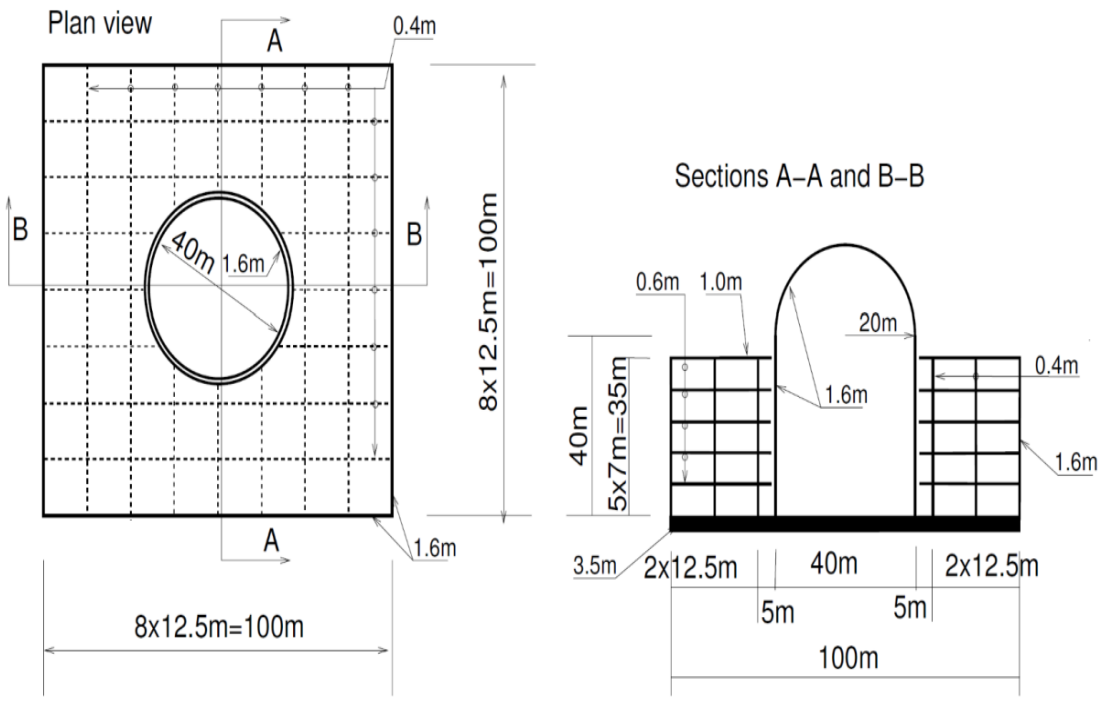

Fig. IV–2. Auxiliary and Containment Building.

IV–1.3. Interface Modelling

Node-to-node penalty-based contact element (gap open/close, frictional slip) K is used to model the interaction between foundation and soil as they are not one continuum material. Contact elements are applied all around the foundation connecting to the soil as shown in Figure IV–1 in red. The friction coefficient between the soil and the foundation is set to $\mu = 0.35$.

IV–1.4. Seismic Motions

Three-dimensional seismic motions were developed using the SW4 program [IV-8] for an earthquake of magnitude (M_w) of 5.5 for a point source on a fault of dimension 5.5x5.6 km with up-dip rupture slip model [IV-5]. The ESSI (Earth-quake Soil Structure Interaction) box to capture the free-field motion was located on the footwall of the reverse thrust fault as shown in Figure IV–3 in green. The generated motion had a directivity effect as the fault slips and propagates in the x-direction.

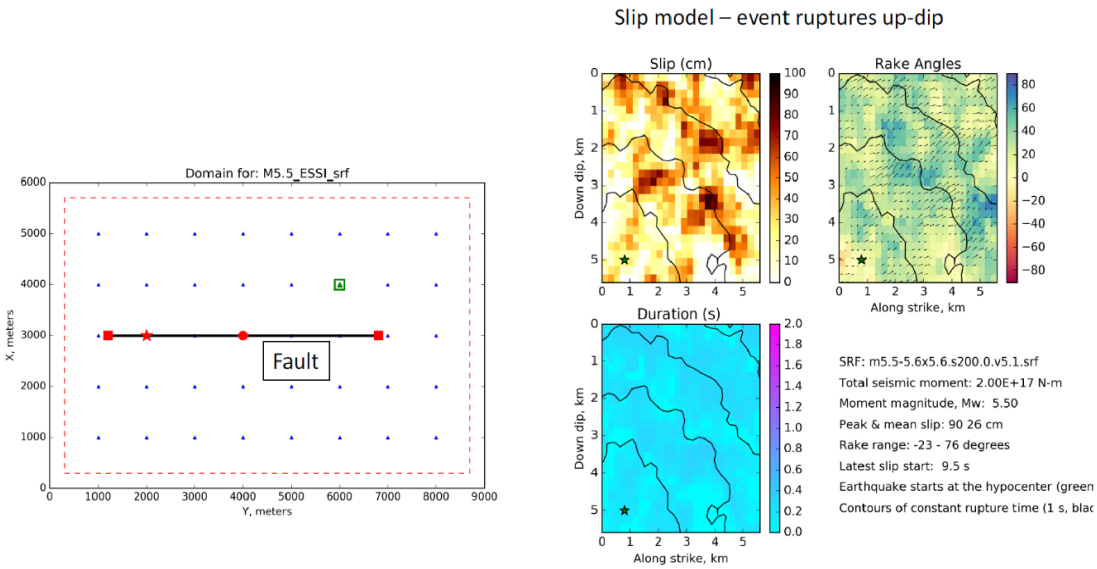

Fig. IV–3. Fault-Rupture earthquake modelling in SW4, (Rodgers, 2017).

The acceleration and displacement time series of the motion at the surface (centre) of a free field model are plotted in Figure IV–4. The PGA in the horizontal directions is about 1g. A significant amount of vertical acceleration is also observed, with a PGA in the vertical direction of 0.5g.

With the fault located at foot-wall side of reverse thrust fault, there is permanent subsidence of about 50mm in z-direction at the end of shaking event. The Fourier transform and response spectra of the motions are shown in Figure IV–5. The frequency range of the motion is within 20 Hz, however, due to finite element size restrictions, motions up to 10 Hz will be accurately modelled.

IV–1.5. Domain Reduction Method

The domain reduction method (DRM) [IV–9, IV–10] is used to apply 3-D seismic motions to the ESSI model.

The DRM layer (see Section 7.4.10) is modelled as single layer of elastic soil. The method takes into account 3-D free-field acceleration and displacement information and generates an equivalent force to drive the model with 3-D motions for each time step (t). The forces act only within a single layer of elements adjacent to the interface between the exterior region and the geological feature of interest. Three damping (absorbing) layers are applied away from the DRM layer to prevent incoming reflected waves. For this analysis, 25% Rayleigh damping was applied in each of the damping layers.

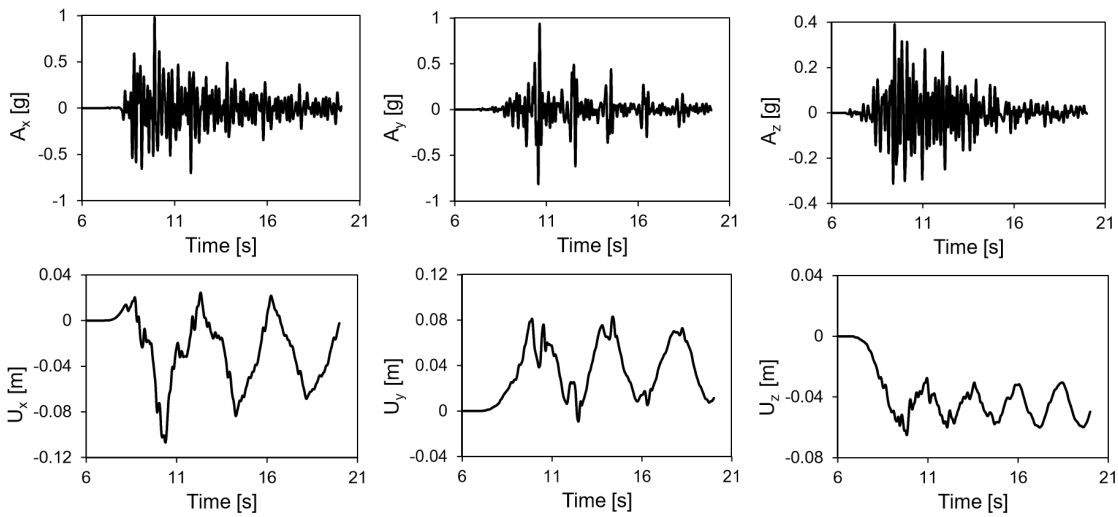

Fig. IV–4. Acceleration and Displacement Time Series of Motion.

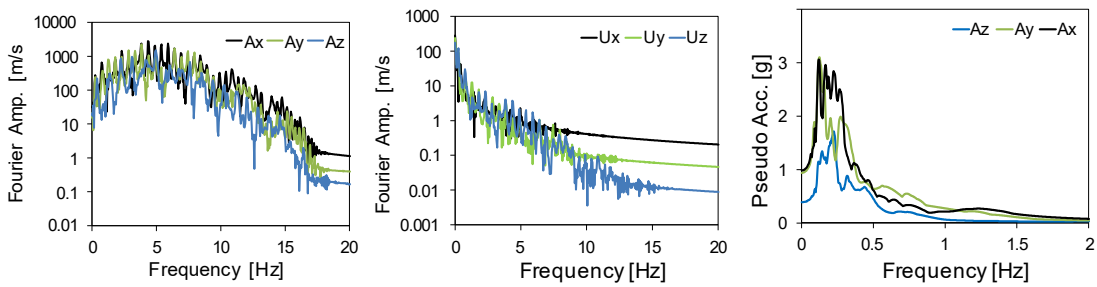

Fig. IV–5. Strong Motion Fourier Transform and Response Spectrum.

IV–1.6. Staged Simulation

The analysis was simulated with two loading stages. The first stage is the static self-weight to get the initial stress state of the soil and contact elements. In the second stage, seismic motion is applied using the DRM method. For each stage, equilibrium was achieved using the full Newton-Raphson method with a small tolerance of 1 x 10^{-4} N on the second norm of the unbalanced force. For dynamic analysis, the Newmark integration method with no-numerical damping was used. A small Rayleigh damping of 5% in soil and 2% in structure was externally applied. The time step considered here was 0.03 seconds with the simulation running in total for 20 seconds.

The analysis was run in parallel using the Real ESSI (Realistic Earthquake-Soil-Structure Interaction) Simulator [IV–17] on eight CPUs. The model consisted of about 300,000 degrees of freedom. Four scenarios (elastic no contact, elastic with contact, elastic-plastic no contact, and elastic-plastic with contact) were performed.

IV–1.7. Simulation Results

Due to space restriction, only a few locations were selected to study the non-linear effects on the NPP structure. The selected locations are shown in Figure IV–6. Since the containment building is more flexible than auxiliary building, point D located on the top of the containment building describes the maximum drift during shaking. Three locations A, B and C located along the foundation centreline were selected to study the slip at the interface during shaking.

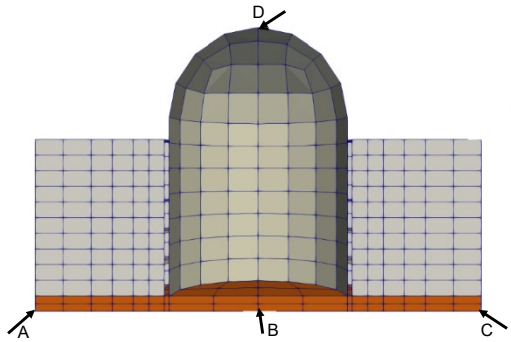

Fig. IV–6. Specific locations selected for study of non-linear effects on an NPP structure.

Since the site is located on the foot wall, during shaking permanent subsidence of the whole structure with soil to about 50 mm in elastic and 60 mm in elastic-plastic case was observed. In the self-weight stage, the soil settled by 150 mm in the elastic case and 230 mm in elastic-plastic case. Figure IV–7 shows the displacement and acceleration response of location D. Elastic-plastic soil shows natural damping to some high frequencies because of dissipating energy in the form of heat by hysteresis loop whereas, the elastic case with or without contact retains/increases the high frequency components of the wave. This can be observed from the Fourier amplitude of displacement.

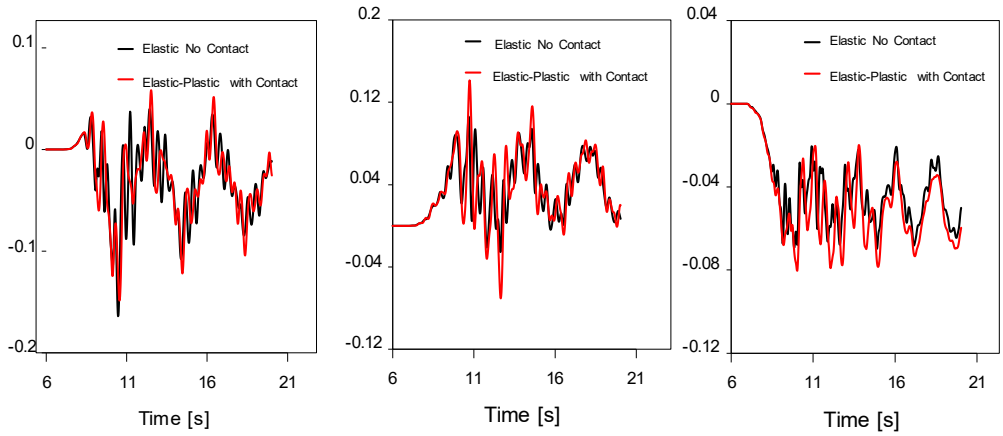

(a) Displacement (x, y and z)

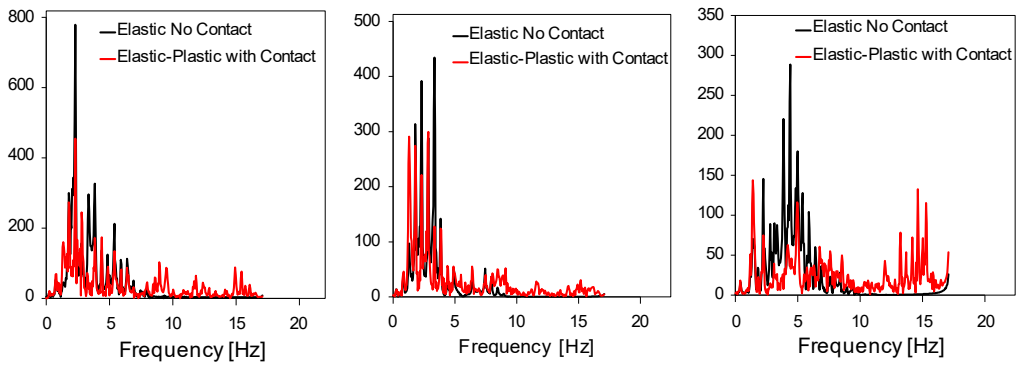

(b) Fourier Amplitude of Acceleration (x, y and z)

Fig. IV–7. Seismic Response at Top of Containment Building.

It is important to predict the development of high frequency excitation during shaking that could prove significant (when close to fundamental frequency) to equipment at a nuclear installation. Figure IV–7 plots the acceleration and its Fourier amplitude for location A. The elastic-plastic analysis leads to some high frequency excitations in the structure. Some of these high frequencies are a result of the introduction of contact at the soil–foundation interface. During shaking, the foundation slips and lifts creating some high frequency waves. The effects of contacts are even more dramatic when coupled with elastic material. The presence of high frequencies here, are more significant in the vertical direction. These high frequencies are thus, important, for design of nuclear building to ensure the safety of equipment. Figure IV–8 presents the deformation of the NPP structure at 11 seconds.

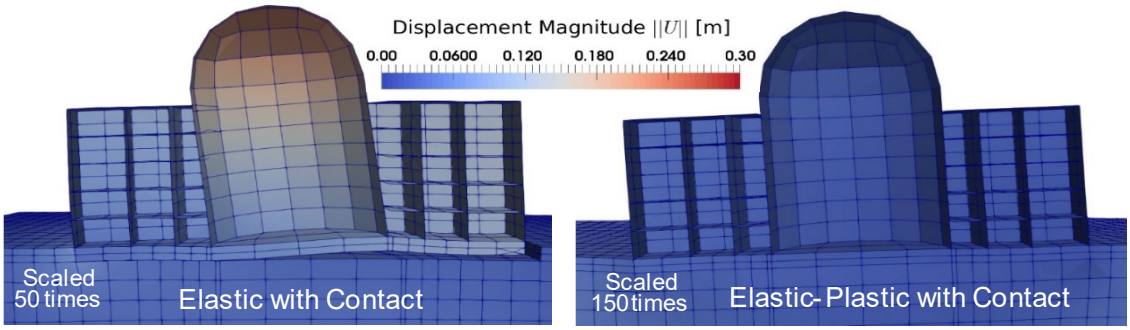

Fig. IV–8. Deformation of the NPP structure at 11 seconds.

REFERENCES TO ANNEX IV

[IV-1] WATANABE, K., PISANO, F., JEREMIC, B., A numerical investigation on discretization effects in seismic wave propagation analyses. Engineering with Computers (2016).

[IV-2] JEREMIC, B., JIE, G., PREISIG, M., TAFAZZOLI, N., Time domain simulation of soil-foundation-structure interaction in non-uniform soils. Earthquake Engineering & Structural Dynamics (2009).

[IV-3] YANG, Z., ELGAMAL, A., PARRA, E., Computational model for cyclic mobility and associated shear deformation. Journal of Geotechnical and Geoenvironmental Engineering (2003).

[IV-4] DAFALIAS, Y. F., MANZARI, M.T., Simple plasticity sand model accounting for fabric change effects. Journal of Engineering mechanics (2004).

[IV-5] PARK, S., BYRNE, P., Practical constitutive model for soil liquefaction. In Proc., 9th Int. Symp. on Numerical Models in Geomechanics (NUMOG IX), CRC Press, Boca Raton, FL, 2004. A. Rodgers. Private communications. SW4 – Real ESSI connection, (2017).

[IV-6] BOULANGER, R., ZIOTOPOULOU, K., Formulation of a sand plasticity plane-strain model for earthquake engineering applications. Soil Dynamics and Earthquake Engineering (2013).

[IV-7] JEREMIC, B., Development of analytical tools for soil-structure analysis. Technical Report R444.2, Canadian Nuclear Safety Commission – Comission canadiene de suˆret´e nucl´eaire, Ottawa, Canada, (2016).

[IV-8] SIOGREEN, B., PETERSSON, N. A., A Fourth Order Accurate Finite Difference Scheme for the Elastic Wave Equation in Second Order Formulation. J. Sci. Comput. (2011).

[IV-9] BIELEK, J., LOUKAKIS, K., HISADA, Y., YOSHIMURA, C., Domain reduction method for three-dimensional earthquake modelling in localized regions, part i: Theory. Bulletin of the Seismological Society of America, (2003).

[IV-10] YOSHIMURA, C., BIELAK, J., HISADA, Y., FERNANDEZ, A., Domain reduction method for three-dimensional earthquake modelling in localized regions, part ii: Verification and applications. Bulletin of the Seismological Society of America (2003).

Annex V

NON-LINEAR ANALYSIS OF A DEEPLY EMBEDEED SMALL MODULAR REACTOR (SMR)

In this analysis, 11 representative points are selected in the SMR to analyse the seismic response, as shown in Figure V–1. The location of the points and layer information are provided in Table V–1.

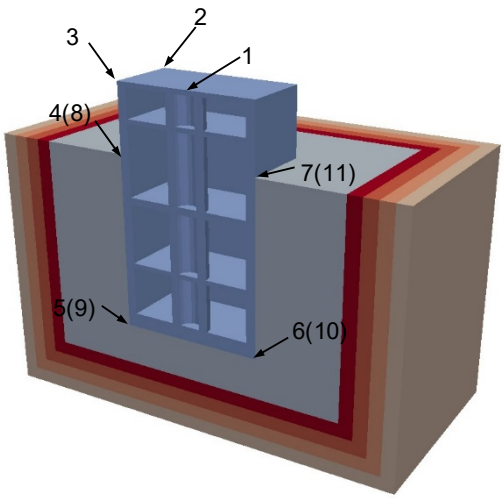

FIG. V–1. Representative points configuration.

Three representative points are chosen to display here: Point 3 locates at the top part of the structure, which is 14 meters above the ground surface. Point 4 is located on the ground surface. Point 5 is 36 meters embedded in the ground.

TABLE V–1. REPRESNETATIVE POINTS

Point ID	X (m)	Y (m)	Z (m)	layer
1	0	0	14	structure
2	15	15	14	structure
3	0	15	14	structure
4	0	15	0	structure
5	0	15	-36	structure
6	0	-15	-36	structure
7	0	-15	0	structure
8	0	15	0	surrounding soil
9	0	15	-36	surrounding soil
10	0	-15	-36	surrounding soil
11	0	-15	0	surrounding soil

The acceleration responses in the time and frequency domains for several points are presented in Figures V–2 to V–7.

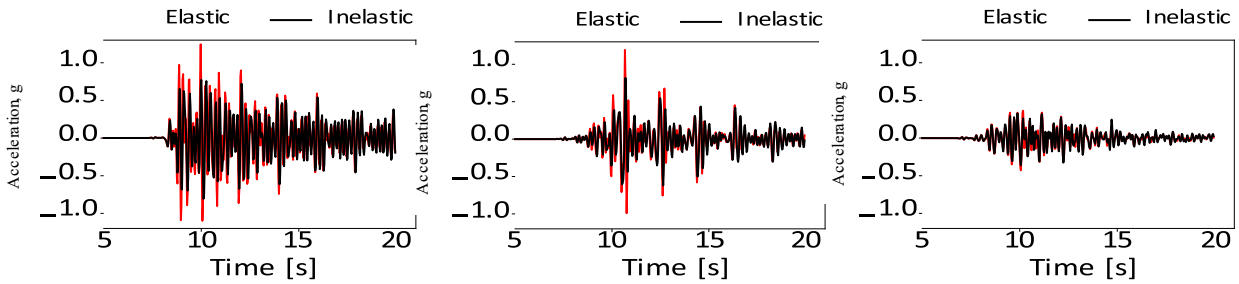

(a) A_x (b) A_y (c) A_z

FIG. V–2. Acceleration response of point 3 above ground surface.

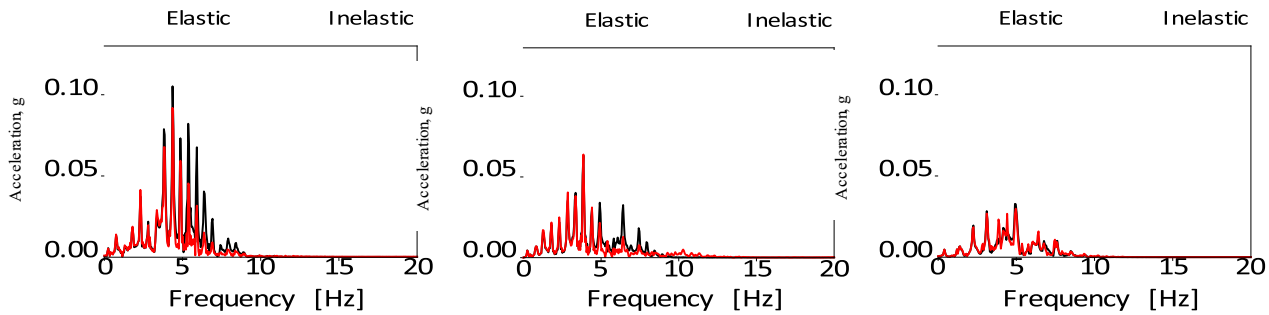

(a)FFT A_x (b) FFT A_y (c) FFT A_z

FIG. V–3. Acceleration response of point 3 in frequency domain.

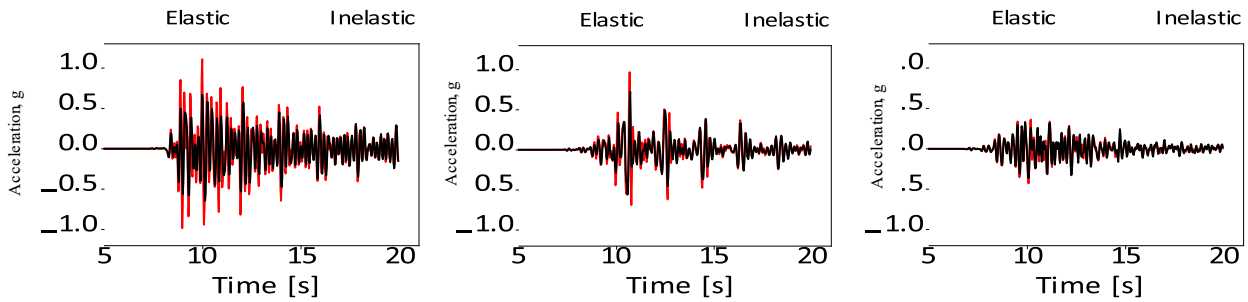

(a) A_x (b) A_y (c) A_z

FIG. V–.4. Acceleration response of point 4.

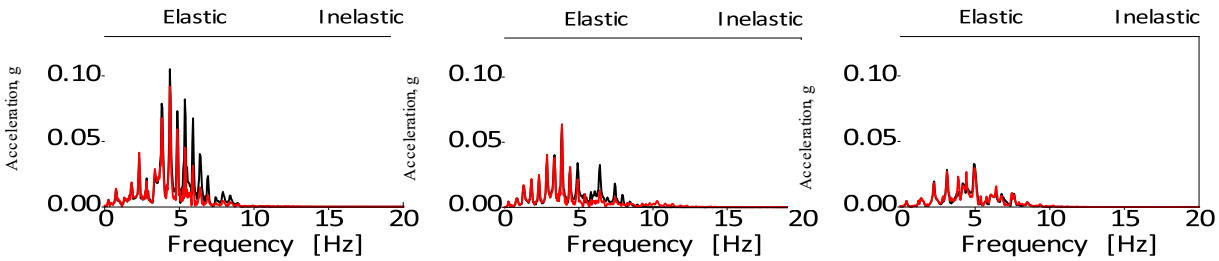

(a)FFT A_x (b)FFT A_y (c)FFT A_z

FIG. V–5. Acceleration response of point 4 in frequency domain.

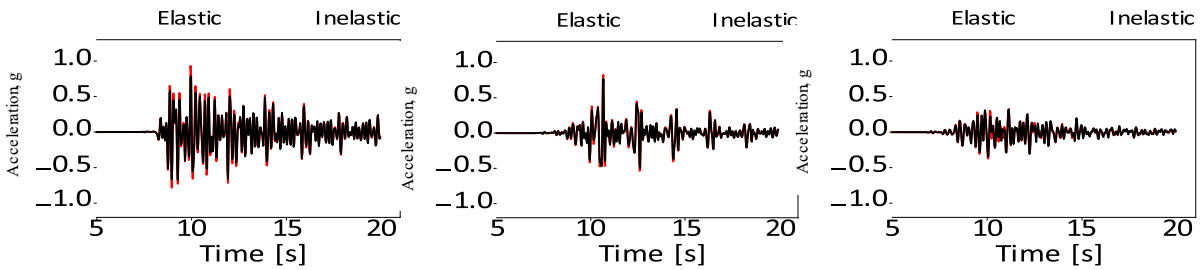

(a) A_x (b) A_y (c) A_z

FIG. V–6. Acceleration response of point 5.

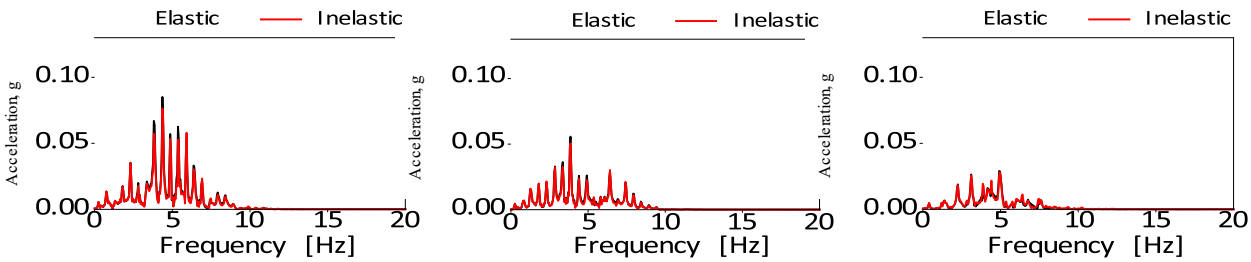

(a)FFT A_x (b)FFT A_y (c)FFT A_z

FIG. V–7. Acceleration response of point 5 in frequency domain.

Annex VI

NONLINEAR, TIME DOMAIN, 3D, EARTHQUAKE SOIL STRUCTURE INTERACTION (ESSI) ANALYSIS OF NPP, ANALYSIS PROCEDURES

All procedures are described in detail in [VI–1]

REFERENCES TO ANNEX VI

[VI-1] JEREMIC, B., YANG, Z., CHENG, Z., JIE, G., TAFAZZOLI, N., PREISIG, M., TASIOPOULOU, P., PISANO, F., ABELL, J., WATANABE, K., FENG, Y., KUMAR SINHA, S., BEHBEHANI, F., YANG., H., WANG, H., Nonlinear Finite Elements: Modelling and Simulation of Earthquakes, Soils, Structures and their Interaction, University of California, Davis, and Lawrence Berkeley National Laboratory, Berkeley, CA USA (1989-2021).

Annex VII

EQUIVALENT BULK MODULUS FOR UNSATURATED SOIL

For a porous medium in which the voids are filled with gas and water, the homogenized undrained bulk modulus is given by [VII–1]:

$$k_u^{\text{hom}} = \frac{(1-n)k_s + k_w \frac{nS}{1+\frac{\alpha_s}{k_s}(k_w-k_s)} + k_g \frac{(1-S)n}{1+\frac{\alpha_s}{k_s}(k_g-k_s)}}{1-n+\frac{nS}{1+\frac{\alpha_s}{k_s}(k_w-k_s)} + \frac{(1-S)n}{1+\frac{\alpha_s}{k_s}(k_g-k_s)}} \qquad \text{(VII–1)}$$

Where

n is the porosity

S is the degree of saturation

k_w is the bulk modulus of water (2 500MPa)

k_g is the bulk modulus of gas (0.1MPa)

k_s , μ_s are the bulk modulus and shear modulus of the solid matrix

$\alpha_s = \frac{3k_s}{3k_s+4\mu_s} = \frac{1+\nu}{3(1-\nu)}$

k_s is not easy to assess but it can be computed from the drained bulk modulus, $k_{\text{dr}}^{\text{hom}}$, obtained from Eq. (VII–1) with $S = k_w = k_g = 0$ and Poisson's ratio which can be assumed equal to 0:

$$k_{\text{dr}}^{\text{hom}} = \frac{(1-n)k_s}{1-n+\frac{n}{1-\alpha_s}} \qquad \text{(VII–-2)}$$

In order to model the unsaturated soil, a 3-phase medium, as a 2-phase medium, we look for the equivalent fluid bulk modulus, $k_{\text{eq,w}}$, of the saturated medium that will give the same undrained bulk modulus as the true 3-phase medium (Eq. (VII–1).

For the saturated 2-phase medium, the homogenized bulk modulus is given by Eq. (VII–1) in which $S = 1$:

$$k_{\text{eq}}^{\text{hom}} = \frac{(1-n)k_s + k_{\text{eq,w}} \frac{n}{1+\frac{\alpha_s}{k_s}(k_{\text{eq,w}}-k_s)}}{1-n+\frac{n}{1+\frac{\alpha_s}{k_s}(k_{\text{eq,w}}-k_s)}} \qquad \text{(VII–3)}$$

Combining Eqs (VII–1 to VII–3), the equivalent fluid modulus $k_{\text{eq,w}}$ is given by:

$$\frac{k_{\text{eq,w}}}{k_s} = \frac{k_g[(1-\alpha_s)k_s+\alpha_s k_w]-(1-\alpha_s)Sk_s(k_g-k_w)}{\alpha_s Sk_s(k_g-k_w)+k_s[(1-\alpha_s)k_s+\alpha_s k_w]} \qquad \text{(VII–4)}$$

It can easily be checked that for the two extreme cases of unsaturated or fully saturated soil, the bulk modulus of gas or of water are retrieved from Eq. (VII–4)

- $S = 0$, $k_{\text{eq,w}} = k_g$

- $S = 1$, $k_{\mathrm{eq,w}} = k_{\mathrm{w}}$

The ratio of the apparent bulk modulus of water to the true one is plotted versus the degree of saturation in Figure VII–1 for $k_{\mathrm{dr}}^{\mathrm{hom}} = 950\mathrm{MPa}$ and $\nu = 0$.

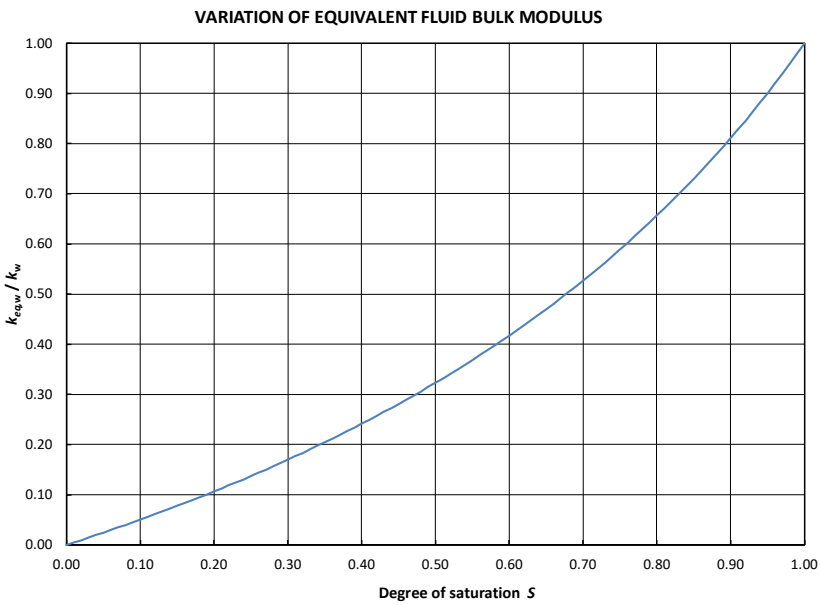

FIG. VII–.1. Variation of equivalent fluid bulk modulus.

REFERENCES TO ANNEX VII

[VII–1] DORMIEUX, L., KONDO, D., ULM, F.J., Microporomechanics, J. Wiley (2006).